UNIVERSITY OF CALIFORNIA SAN DIEGO

Distinctive Impacts of Extreme Warm Season Precipitation and Climate Change on the Vulnerable Water Resources of the Southwestern United States

A dissertation submitted in partial satisfaction
of the requirements for the degree
Doctor of Philosophy

in

Oceanography

by

Michael D. Sierks

Committee in charge:

Fred Martin Ralph, Chair
Jennifer Burney
Michael Dettinger
Jan Kleissl
Katherine Ricke
Shang-Ping Xie

2022

The Dissertation of Michael D. Sierks is approved, and it is acceptable in quality and form for publication on microfilm and electronically.

University of California San Diego

2022

DEDICATION

To Allie and Jack

TABLE OF CONTENTS

Dissertation Approval Page iii
Dedication iv
Table of Contents v
List of Figures viii
List of Tables xi
Acknowledgments xii
Curriculum Vitae xvi
Abstract of Dissertation xvii
Chapter 1 - Introduction 1
1.1 Motivation and Background 1
1.2 Dissertation Overview 5
Chapter 2 - Characteristics, Origins, and Impacts of Summertime Extreme Precipitation in the Lake Mead Watershed 7
2.1 Introduction 8
2.2 Data and Methods 10
2.2.1 Watershed Subdivisions 10
2.2.2 Precipitation 10
2.2.3 Meteorology 11
2.2.4 Tropical Cyclone Inventory 12
2.3 Results 13
2.3.1 Climatology of JAS Precipitation 13
2.3.2 Relationship Between Number of Wet Days and Total JAS Precipitation 14
2.3.3 Relationship Between Extreme Events and JAS Total Precipitation 15
2.3.4 Seasonality of Extreme Events and Tropical Cyclones 15
2.3.5 Dynamical Drivers of Extreme Events 15
2.4 Discussion 21
2.5 Concluding Remarks 26
2.6 Acknowledgements 27
2.7 Appendix A: Extreme Precipitation Events by Synoptic Categorization 42
2.8 Appendix B: Precipitation Distributions for Extreme Events in the Lake Mead Watershed 44
Chapter 3 – Seasonally Anchored Bias Correction of CMIP5 Hydrological Simulations 49
3.1 Introduction 50
3.1.1 Climate Change Impacts 50

3.1.2 Downscaling and Bias Correction 50
3.1.2.1 Windowing and Bias Correction Goals 51
3.1.3 Purpose of Paper 53
3.2 Study Domain 54
3.3 Data 54
3.4 Methodology 56
3.4.1 Climatological Hydrograph 56
3.4.2 Locating Milestones 57
3.4.2.1 Maximum and Minimum Streamflow 57
3.4.2.2 Start of Dry Season 57
3.4.2.3 Start of Wet Season 58
3.4.3 Calculating Mean Milestones Across Quantiles 59
3.4.4 Seasonally Anchored Windowing 60
3.4.5 Bias Correction Methods to be Compared 60
3.5 Results and Discussion 62
3.5.1 Validation Over the Historical Period 63
3.5.2 Water Year Mean Streamflow 63
3.5.3 Wet Season Streamflow by Decile 65
3.5.4 Temporal Shift in Peak Streamflow 67
3.6 Summary and Conclusion 68
3.7 Acknowledgments 73
3.8 Appendix A: Identification of Peak Streamflow Milestone for Bimodal Climatological Hydrographs 89
3.9 Appendix B: Original Model Change in Wet Season Streamflow by Decile 93
3.10 Appendix C: Error in Wet Season Streamflow by Decile 98
Chapter 4 – Climate Change Impacts on Lake Shasta: Assessing Adaptation Measures for California's Largest Reservoir 106
4.1 Introduction 107
4.2 Background 109
4.2.1 Lake Shasta Watershed 109
4.2.2 Reservoir Operations 110
4.3 Data 111
4.3.1 Historical Period 111
4.3.2 Future Climate Projections 112
4.4 Model Development and Validation 112
4.4.1 Wet-Season Operations 113
4.4.2 Dry-Season Operations 113
4.4.3 Model Calibration and Validation 114
4.5 Results and Discussion 115

4.5.1 Streamflow Changes 115
4.5.1.1 Seasonal Inflow Timing and Magnitude Changes 116
4.5.1.2 Inflow Parameter 116
4.5.2 Operations Under Existing Rules 117
4.5.3 Sensitivity to Changing the Refill Date 120
4.5.4 Sensitivity to Use of a Single Rule Curve 121
4.5.5 Sensitivity to Raising the Dam 122
4.5.5 Sensitivity to Perfect Forecast Operations 125
4.6 Summary and Conclusion 128
4.7 Acknowledgments 135
4.8 Supplementary Materials 154
4.8.1 Variable Rule Curve 154
4.8.2 Simulated Wet-Season Operations 155
4.8.2.1 Storage Exceeds the Rule Curve 155
4.8.2.2 Storage Below the Rule Curve 156
4.8.3 Simulated Dry-Season Operations 156
4.8.4 Estimation of Daily Evaporation 158
4.8.5 Downscaling GCM Data Using Station Data 159
4.8.5.1 Station-to-Gridded Data 159
4.8.5.2 Secondary Bias Correction 160
4.8.6 Station Data Information 160
4.8.6.1 CDEC Rainfall Stations 160
4.8.6.2 CDEC SWE Stations 162
4.8.6.3 CDEC Temperature Stations 163
4.8.6.4 CDEC Reservoir Inflow Stations 164
Chapter 5 - Conclusion 165
5.1 Summary of Major Contributions 165
5.2 Directions for Future and Related Research 167
Chapter 6 - References 169

LIST OF FIGURES

Figure 2.1. Topography of the Lake Mead watershed including major tributaries and their sub-basins […] 31

Figure 2.2. Average characteristics for sub-basins for (a) JAS precipitation, (b) fraction of water year precipitation during JAS, and (c) coefficient of variation of JAS precipitation […] 32

Figure 2.3. Relationship between total seasonal JAS precipitation and number of wet days per JAS for each basin […] 33

Figure 2.4. Seasonal distribution of extreme events color-coded by month for each sub-basin with 95th percentile precipitation values (mm) shown in parentheses […] 34

Figure 2.5. Example of a 'canonical' Rossby wave break extreme precipitation event. 200-hPa potential vorticity standardized anomaly […] 35

Figure 2.6. Composite fields for combined 'canonical' and 'TC tapping' RWB cases (n=16) in the combined Lake Mead watershed on day of extreme precipitation […] 37

Figure 2.7. Composite fields for IV cases (n=8) in the combined Lake Mead watershed on day of extreme precipitation for (a) 200-hPa potential vorticity standardized anomaly (shaded), 200-hPa potential vorticity […] 38

Figure 2.8. Hovmöller plots of standardized anomalies for (a) 200-hPa potential vorticity, (b) 700-hPa meridional wind, (c) integrated water vapor […] 39

Figure 2.9. Idealized synoptic set-ups for primary drivers of extreme precipitation in the Lake Mead watershed, (a) RWB (b) IV (adapted from Pytlak et al., 2005), and their corresponding characteristic meteorology […] 41

Figure 2.1B. 24-hour PRISM precipitation field for an extreme precipitation event occurring on 23 Sep 2007 […] 45

Figure 2.2B. 72-hour PRISM precipitation field for an extreme precipitation event occurring on 23 Sep 2007 […] 46

Figure 2.3B. 24-hour PRISM precipitation composite for 'canonical' and 'TC Tapping' RWB extreme precipitation events for the combined Lake Mead watershed […] 47

Figure 2.4B. 24-hour PRISM precipitation composite centered around the day of extreme precipitation for IV events for the combined Lake Mead watershed […] 48

Figure 3.1. Map of the study domain with watershed boundaries (black contour), gage locations (purple circle), and three-letter abbreviations for the 6 streams […] 79

Figure 3.2. Visual depiction of the algorithm used to identify climatological milestones for the seasonally anchored windowing method […] 80

Figure 3.3. Schematic highlighting the effect of windowing technique on which segments of the climatological hydrograph are used to bias correct a given model […] 81

Figure 3.4. Daily mean streamflow for the observed (black), and bias corrected data over the historical period for PresRat with seasonally anchored […] 82

Figure 3.5. Original model projected change in water year mean streamflow across the 6 streams (rows) and 10 GCMs (columns) with the 10-member ensemble […]..... 83

Figure 3.6. Original model projected change in Shasta streamflow by decile (rows) and GCM (columns) with the 10-member ensemble mean and standard […]..... 84

Figure 3.7. Error by decile for change in wet season streamflow for PresRat with seasonally anchored windowing […]..... 85

Figure 3.8. Flow weighted root-mean-square error (RMSE) in the representation of model-predicted future change in mean flow at each decile […]..... 86

Figure 3.9. Change in timing of peak climatological streamflow for the original model change (x-axis) and PresRat with seasonally anchored […] 87

Figure 3.10. Change in timing of peak climatological streamflow for the original model change (x-axis) and PresRat with seasonally anchored […]..... 88

Figure 3.1A. Visual depiction of the algorithm used to identify climatological milestones […] 90

Figure 3.2A. Climatological hydrographs (lines) for flows ranging from the 5th to 95th percentile […]..... 91

Figure 3.3A. Day of water year associated with the ‘start of wet season’ […]..... 92

Figure 3.1B. Original model projected change in Napa River streamflow by decile (rows) and GCM (columns) with the 10-member […]..... 93

Figure 3.2B. Original model projected change in Elder Creek streamflow by decile (rows) and GCM (columns) with the 10-member […]..... 94

Figure 3.3B. Original model projected change in Oroville Dam streamflow by decile (rows) and GCM (columns) with the 10-member […]..... 95

Figure 3.4B. Original model projected change in New Melones Reservoir streamflow by decile (rows) and GCM (columns) with the 10-member […]..... 96

Figure 3.5B. Original model projected change in Millerton/Friant Dam streamflow by decile (rows) and GCM (columns) with the 10-member […] 97

Figure 3.1C. Error by decile for change in wet season streamflow for PresRat with standard day-of-year windowing […]..... 99

Figure 3.2C. Error by decile for change in wet season streamflow for CDFt with seasonally anchored windowing […]..... 100

Figure 3.3C. Error by decile for change in wet season streamflow for CDFt with standard day-of-year windowing […]..... 101

Figure 3.4C. Error by decile for change in wet season streamflow for EDCDFm with seasonally anchored windowing […] 102

Figure 3.5C. Error by decile for change in wet season streamflow for EDCDFm with standard day-of-year windowing […]..... 103

Figure 3.6C. Error by decile for change in wet season streamflow for Qmap with seasonally anchored windowing […] 104

Figure 3.7C. Error by decile for change in wet season streamflow for Qmap with standard day-of-year windowing […] 105

Figure 4.1. Map of study area showing the Lake Shasta watershed (black contour), elevation (color shade) […] 138

Figure 4.2. a) The maximum allowable storage behind the dam is governed by Shasta's rule curve, which mandate 1 of 6 possible sub-curves […] 139

Figure 4.3. Model performance over the validation period (WYs 1996-2017); a) timeseries of observed (black) and simulated (red) daily reservoir storage […] 140

Figure 4.4. Lake Shasta inflow for the historical (grey, 1970-2020) and end of century (2050-2099) GCM periods for RCP4.5 (orange) and RCP8.5 (purple) […] 141

Figure 4.5. Centered 30-year averages of cumulative inflow over entire WY (top) and the percent of total WY inflow occurring before and after […] 142

Figure 4.6. Ensemble mean centered 30-year averages of the percentage of days between December 23rd and March 20th that each of the 6 possible sub-rule […] 143

Figure 4.7. Timeseries of daily storage (solid) and operative rule curve (dashed) values for 2 individual water years in CCSM4. The date and […] 144

Figure 4.8. Averaged over each climatological era, ensemble mean values of daily mean cumulative inflow (top, dot-dashed), storage (center, solid), and the operative […] 145

Figure 4.9. Ensemble mean water supply metrics of a) carryover and peak storage, and b) critically low storage levels, under adaptive operations in which the reservoir […] 146

Figure 4.10. Centered 30-year mean values of flood risk as measured by the average percentage of ensemble members requiring a spillway release […] 147

Figure 4.11. Water supply metrics of mean (a) and critically low (b) storage levels under adaptive operations in which the reservoir uses a fixed […] 148

Figure 4.12. Centered 30-year mean values of flood risk as measured by the average percentage of ensemble members requiring a spillway release […] 149

Figure 4.13. Averaged over each climatological era, ensemble mean values of daily mean cumulative inflow (top, dot-dashed), storage (center, solid) […] 150

Figure 4.14. Averaged over each climatological era, ensemble mean values of daily mean cumulative inflow (top, dot-dashed), storage (center, solid) […] 151

Figure 4.15. Centered 30-year mean values of flood risk as measured by the average percentage of ensemble members requiring a spillway release during a given water year […] 152

Figure 4.16. Scatterplot summarizing the risks to water supply and flood mitigation for historical (1970-2020, black marker), RCP4.5 (2050-2099, orange markers) […] 153

LIST OF TABLES

Table 2.1. USGS gage ID and geographical characteristics of the delineated sub-basins and the entire Lake Mead watershed. 29

Table 2.2. Precipitation characteristics of the delineated sub-basins and the entire Lake Mead watershed. 30

Table 2.1A. Independent extreme precipitation event dates for the combined Lake Mead watershed as categorized by synoptic processes defined in Section 2.3.5. 43

Table 3.1. Name, gage identification and summary characteristics of each watershed […] ... 74

Table 3.2. Selection of 10 GCMs from CMIP5 used in this work along with their originating institutions 75

Table 3.3. Summary statistics for each bias correction method (rows) and windowing technique […] 76

Table 3.4. Flow weighted root-mean-square error (RMSE) averaged over all deciles and across all streams […] 77

Table 3.5. Summary of the ability of each bias correction method and windowing technique to preserve the original model signal in the temporal shift in climatological peak streamflow […] 78

Table 4.1. The10 CMIP5 GCMs from which downscaled and bias-corrected projections were used in this study […] 136

Table 4.2. Summary of Nash-Sutcliffe efficiency (NSE) and additional relevant statistics detailing model performance over the validation period […] 137

Table 4.1S. Associated Inflow Parameter value for each of the 6 sub-rule curves governing Lake Shasta's operational rule curve […] 155

Table 4.2S. Station information for all CDEC rainfall data […] 161

Table 4.3S. Station information for all CDEC SWE data […] 162

Table 4.4S. Station information for all CDEC temperature data […] 163

Table 4.5S. Station information for all CDEC reservoir inflow data […] 164

ACKNOWLEDGEMENTS

Thank you to my advisor, Marty Ralph, for taking a chance on me and providing the opportunity to pursue a PhD. Thank you for allowing me the academic and intellectual freedom required to discover my own interests, to learn how to pose my own scientific questions, and to indulge in my curiosity. Your support unlocked opportunities for me to engage with my science in ways I never imagined, and more importantly, connect with people I'll never forget. Mike Dettinger, thank you for serving as my unofficial advisor, for spending countless hours helping me hash out half-baked ideas, correcting poor grammar, and encouraging me to think about the big picture. I feel incredibly lucky to have had the opportunity to work with you over the past few years and you've absolutely changed the way I think about science, its impacts, and how to it can be communicated. Thank you to the additional members of my committee, Jen Burney, Jan Kleissl, Katherine Ricke, and Shang-Ping Xie. To Dave Pierce, thank you for your patience and guidance during the many meetings when my sleep deprived brain was barely functioning.

Joining the Center for Western Weather and Water Extremes, I never imagined I would meet so many genuine, nurturing, and intelligent folks. Anna Wilson, thank you for the endless support of my work and my life outside of research. Your endless capacity to give and help those around is a truly great gift and I know I'm not the first, and won't be the last, person to wish I could find the words to express my gratitude for your friendship. Julie Kalansky, thank you for the years of support and generosity and for checking in when I felt lost. To Allison Michaelis, Leah Campbell, Meredith Fish, Carly Ellis, Forest Cannon, Kara Voss, and Chad Hecht, you made the Center a fantastic place to work. Whether it was dumping water out of toppled ISCOs, singing karaoke after a long day of conferencing, or just catching up after not

seeing one another for a while, there was never a dull moment with any of you, and I consider myself lucky to have friends like you.

My dearest Yaks. Jessica Ng, Jacob Morgan, Theresa Morrison, Ratnaksha Lele, Margaret Lindeman, Luke Kachelein, Mike Kovatch, Julia Dohner, Carrie McIntosh, and Chase James, you are of the highest caliber human beings I've ever met. Each of you is so curious, empathetic, silly, altruistic, passionate, and brilliant. You have all made this chapter of my life worthwhile. Thank you all for the endless support, love, and care you've given me, and to Allie and Jack over the past year. I can neither thank you enough nor express how much your friendship means to me. I am so proud of you all and can't wait to see what outstanding things you will bring to this world.

To my friends and family, thank you for encouraging me to pursue my passions and for being so patient, thoughtful, understanding, and forgiving when I became stressed and consumed by graduate school. I wish that everyone had the chance to feel the love and support you give to me. To my parents, thank you for nurturing my love of the water and supporting me along each chapter of my life. To Erik, Brenna, Ellis, Heidi, and Kevin, thank you for bringing such incredible joy into my life and sharing in my successes and comforting me in my tribulations. To Anthony Jakubisin and Grady Kestler, what a gift it has been sharing the last 12 years of my life with you both. Thank you for helping me grow into the person I am today, thank you for laughing with me and crying with me. I am beyond grateful for your thoughtfulness and generosity. To William Chapman, so much has changed in my life since we met all those years ago, and you've been there for me through it all. I couldn't imagine, hope for, or ask for a better friend. Your friendship is one of the greatest gifts I've known, and I don't tell you enough how much you mean to me and Allie and Jack. I can't wait to see what the

future holds for you and for Fiona. With your drive, passion, and emotional intelligence, you have the world at your fingertips. Selfishly, I hope the path you carve doesn't take you two too far from us, but no matter where it leads, we will be there cheering you on.

And finally, to Allie and Jack. I would not be here today without you; I would not be who I am today without you. Thank you for sharing your life with me. Thank you for supporting me. Thank you for bringing light into my world. Thank you for being selfless and generous; thank you for being gentle and kind; thank you for being silly and whimsical; thank you for being passionate and thoughtful. It has been the greatest gift in my life to have met you. It has been the greatest honor to watch you love Jack both so gently and fiercely. I know this past year has not been easy, and I can't thank you enough for helping me endure and for all the sacrifices you've made to bring me to this day. And to Jack, watching you grow and discover the world over the past 14 months has been unlike anything I could have imagined. I thought I knew love, but I was wrong. Thank you for teaching Allie and I so much about ourselves and each other. It is the honor of a lifetime to be your dad. This world is a wonderous place filled with incredible people. I hope more than anything that you will be as lucky as I've been and find friends like these to share in all the joys and challenges you'll find along the way.

Chapter 2, in full, is a reprint of the material as it appears in Sierks, M., Kalansky, J., Cannon, F., Ralph, F. M. (2020) Characteristics, Origins, and Impacts of Summertime Extreme Precipitation in the Lake Mead Watershed. Journal of Climate. © American Meteorological Society. Used with permission. The dissertation author was the primary investigator and author of this paper.

Chapter 3, in full, is the material submitted to the Journal of Hydrometeorology. Sierks, M., Pierce, D. W., Chapman, W. E., Ralph, F. M. (2022) Seasonally Anchored Bias Correction

of CMIP5 Hydrological Simulations. The dissertation author was the primary investigator and author of this paper.

Chapter 4, in part, is currently being prepared for submission for publication of the material. Sierks, M., Dettinger, M., Chapman, W. E., Ralph, F. M. The dissertation author was the primary investigator and author of this paper.

VITA

2013 Bachelor of Science in Engineering, University of California San Diego

2015 Master of Science in Engineering, University of North Carolina Chapel Hill

2022 Doctor of Philosophy in Oceanography, University of California San Diego

PUBLICATIONS

Sierks, M.D., Pierce, D.W., Chapman, W. E., Ralph, F.M., 2022. Seasonally anchored bias correction of CMIP5 hydrological simulations. *Journal of Hydrometeorology (in review)*

Chapman, W., Subramanian, A.C., Xie, S.-P., **Sierks**, **M.D.,** Ralph, F.M., and Kamae, Y., 2021. Monthly modulations of ENSO teleconnections: Implications for potential predictability in North America, *Journal of Climate*, *34*(14), 5899-5921.

Sierks, M.D., Kalansky, J., Cannon, F., Ralph, F. M., 2020. Characteristics, origins, and impacts of summertime extreme precipitation in the Lake Mead watershed. *Journal of Climate*, *33*(7), 2663-2680.

Hatchett, B. J. […], **Sierks, M.D.**, […], 2020. Observations of an extreme atmospheric river storm with a diverse sensor network. *Earth Space Science* 7, e2020EA001129.

ABSTRACT OF THE DISSERTATION

Distinctive Impacts of Extreme Warm Season Precipitation and Climate Change on the Vulnerable Water Resources of the Southwestern United States

by

Michael D. Sierks

Doctor of Philosophy in Oceanography

University of California San Diego, 2022

F. Martin Ralph, Chair

This dissertation explores the influence of extreme precipitation and the potential impacts of climate change on the vulnerable water resources of the southwestern United States. Specifically, it focuses on 1) the characteristics, origins, and impacts of historical extreme

warm-season precipitation in the Lake Mead watershed, 2) improving existing bias correction techniques for projected future streamflows, and 3) investigating the vulnerability of California's largest reservoir, Lake Shasta, to climate change under existing and adaptive operating protocols.

Although the North American Monsoon (NAM) is the main driver of summertime climate variability in the American southwest, considerable knowledge gaps exist regarding its impact at the northern extent of the core region (northwestern Mexico, southern Arizona, and New Mexico). The first part of this dissertation catalogues historical extreme precipitation events in the Lake Mead watershed (located at the NAM's northern boundary) and identifies unique synoptic drivers of extreme precipitation between the canonical NAM region and watersheds to the north.

From here, the dissertation shifts its focus from the historical period to future climate projections. Motivated by a desire to connect bias correction techniques to the underlying dynamics within earth systems models, a novel statistical method is developed for projected streamflow wherein data are windowed based on hydrograph-relative time, rather than Julian day. This method yields improved preservation of original climate model data for both extreme and non-extreme events.

Utilizing these bias corrected streamflow projections, and a simplified model of operations at California's largest reservoir, Lake Shasta, developed by the author, coming threats to water supply and flood risk under existing operations and several forms of adaptive responses to climate change are analyzed. Compared to the historical period, we simulate 27% declines in carryover storage (storage on September 30th) at the end of the 21st century under a severe warming scenario if operations are left unchanged. Despite many simulated interventions

favoring water supply over flood risk, historical levels of carryover storage were irretrievable at the end of the century under the warmer of the two warming scenarios examined in this study.

Chapter 1

Introduction

1.1 Motivation and Background

The southwestern United States is characterized by several distinct hydroclimates. Owing to its vast geographic extent and orographic features, the region is home to a diverse range of ecosystems transitioning from the lush Pacific coast, to the craggy snowcapped peaks of the Sierra Nevada and Rocky Mountain ranges, to the arid Mojave and Sonoran deserts. Despite stark differences in seasonal and average annual precipitation totals between these regions, all are characterized by water extremes (scarcity and flooding). The regions are also inextricably linked by their heavy reliance on water from the Colorado River, which flows southwest from the Rocky Mountains towards the Gulf of California.

Much of the desert and interior intermountain southwest experiences a bimodal distribution of seasonal precipitation with distinct peaks in the winter and summer (Adams & Comrie, 1997 and references therein). While winter precipitation is often fueled by the same storms that soak the coast, summertime precipitation events occur during the North American Monsoon (NAM) season and can have devastating impacts on the built environment in the form of flooding, wind damage, dust storms, power outages, and crop loss (Brazel & Nickling, 1986; Ray et al., 2007). Additionally, quantifying and ultimately predicting how monsoon rains translate into water resources and ecosystem benefits, especially when the monsoon is extreme, is a continuing problem for scientists and engineers.

Typical of a Mediterranean climate, the coastal regions have distinct rainy and dry seasons with considerable interannual variability of precipitation wherein a small number of large storms (between 5-7 on average) contribute most of the wet season precipitation in a given year (Dettinger & Cayan, 2014; Dettinger et al., 2011). As rainfall quenches soils and greens up lowland ecosystems during the winter, the snow that accumulates at high elevations persists long after the final drops of rain have fallen. Slowly melting throughout the spring and into the dry season, the snowpack provides a vital water resource across the West.

Reflecting a regional predisposition for drought and deluge conditions, carefully engineered to leverage the asynchronous arrivals of rain-driven and snowmelt-fed streamflows, many western reservoirs provide both water supply and flood-risk mitigation benefits. To reduce downstream flooding, empty space (storage volume) is mandated behind most dams during boreal winter as a trap for possible flood inflow (this empty space is called the flood pool). Such operation relies on springtime snowmelt to rebuild storage levels after major flood risks begin their climatological seasonal declines (US. Army Corps of Engineers, 1977).

However, the alpine snowpack, particularly in California's Sierra Nevada range, is as vulnerable as it is valuable. Warming temperatures have led to declining snowpacks during recent decades (Berg & Hall, 2017; Mote et al., 2018; Pierce et al., 2008), a trend that is projected to worsen with higher levels of atmospheric greenhouse gases (Barnett et al., 2008; Leung et al., 2004; Nijssen et al., 2001), compounding existing challenges to the region's water resources (Christensen et al., 2004; Knowles et al., 2018; Knowles et al., 2006; Lee et al., 2006). Additionally, rising freezing levels, resulting in a greater fraction of precipitation falling as rain versus snow (Barnett et al., 2008; Knowles et al., 2006; Leung et al., 2004; Nijssen et al., 2001), alongside projected increases in rain-on-snow events (McCabe et al., 2007;

Musselman et al., 2018), and more extreme winter precipitation (Gershunov et al., 2019) result in heightened simulated flood risk. Moreover, interannual variability of precipitation is projected to increase (Swain et al., 2018) as conditions favoring long-term droughts separating occasional large storms and streamflows become more likely (Mann & Gleick, 2015; Polade et al., 2014).

Such hydroclimatic changes are expected to have direct implications for water management. In addition to baseline increases in flood risk, as streamflow shifts to earlier in the year in response to rising snowlines, a larger fraction of total reservoir inflows may not be converted to storage gains (being sapped instead by flood-management releases). Thus, in the absence of springtime snowmelt inflows, reservoirs will not be able to refill as much as they are designed for (Cohen et al., 2020; Knowles et al., 2018; Sterle et al., 2020) leaving water managers in difficult positions, needing to adapt operations to an increasingly volatile and uncertain future.

Although many of the above global warming 'fingerprints' are robust and their impacts will be widespread, individual river basins, watersheds, and reservoir drainage areas will not be impacted uniformly (Das et al., 2011; Kalra et al., 2008; Mote et al., 2005, 2018). Both physical (e.g., elevation, topographic aspects, vegetation) and meteorological (e.g., moistening of the atmosphere, large-scale weather pattern changes and increased amplitudes of seasonal temperature cycles) factors will control the response of water supply-relevant variables, such as annual streamflow, total precipitation, or snowpack volume (Gonzalez et al., 2018; M. He et al., 2019; Huning & AghaKouchak, 2018; Pierce & Cayan, 2013). As a result, the potential impacts of climate change on water management and the health of riparian and riverine

ecosystems need to be examined on local scales and on a case-by-case basis, along with associated mitigation or adaptation strategies.

Investigating the impacts of climate change, or assessing the efficacy of adaptation and mitigation strategies, at the local level requires high resolution simulations of projected future climate. Though a key part of the process, global climate models (GCMs) are necessary but insufficient tools due to the mismatch between their resolution (~100 km) and that required to study change at the local scale (~10 km or less) as well as inherent GCM biases. Prior to being used for local applications, future climate projections typically undergo a process called downscaling and bias correction in which GCM output is combined with higher-resolution historical observations, topography, and/or dynamics to resolve smaller-spatial scale features while removing systematic errors in the GCM. While valuable and widely applied, the resulting future climate data is sensitive to the downscaling methodology used and many bias correction schemes alter the GCM-predicted change for unphysical reasons (Hagemann et al., 2011; Maraun, 2013; Maurer & Pierce, 2014; Pierce et al., 2013). While downscaled and bias corrected GCM output (e.g., temperature, precipitation) is satisfactory for some planning studies, many require the use of a land-surface model to produce variables such as streamflow. In this case, due to biases introduced by the land-surface model, streamflow projections may undergo 'secondary' bias correction before they are used for planning even if downscaled and bias corrected GCM output is used to drive the land surface model.

This dissertation is motivated by the impacts of extreme weather on the people and ecosystems of the southwestern United States, the reliance (and risk exposure) of local-, regional-, and national economies on the water resources of the west, and the threat that climate change poses to each of these topics.

1.2 Dissertation Overview

Through the combination of observational-, reanalyzed-, and GCM data, in addition to the development of novel statistical methods and modeling, the objective of this body of work is to evaluate both existing warm season precipitation extremes and projected impacts of climate change on the vulnerable water resources of the southwestern United States. The dissertation is organized in the following manner.

In Chapter 2, the synoptic drivers of extreme summertime (defined here as July-September) precipitation over the Lake Mead watershed are examined through composite and individual event analysis. Lake Mead is the nation's 2nd largest reservoir and is located on the Colorado River, spanning segments of the borders of Utah, Nevada, and Arizona. This location is particularly interesting as it exists in the transition zone between the core of the North American Monsoon (NAM) region and the area to the north, which is very much on the periphery of the NAM's influence. A greater understanding of the atmospheric conditions most conducive to extreme precipitation may help improve emergency preparedness and even water management. Following this evaluation of summer precipitation in the observed record and at synoptic timescales, the focus of this dissertation shifts to future climate projections and decadal timescales.

Chapter 3 evaluates whether the current standard streamflow bias-correction technique of applying a calendar-based time window, often 1-month long, to adjust a given global climate model (GCM) datapoint is suitable for systems characterized by changes in both magnitude and seasonality. Motivated by a desire to connect bias correction techniques to the underlying dynamics within hydrologic models, a novel statistical method is developed for correcting

projected streamflows wherein biases are determined and windowed based on hydrograph-relative time, rather than by rigid day-of-year considerations.

Building from the dataset produced in Chapter 3, Chapter 4 investigates projected climate change impacts on California's Lake Shasta and identifies specific variables that govern its vulnerability. Through the development of a highly flexible reservoir-operations model, climate-change challenges to water supply and flood risk under existing operations and with several different adaption responses are simulated and evaluated.

Chapter 2

Characteristics, Origins, and Impacts of Summertime Extreme Precipitation in the Lake Mead Watershed

Abstract

The North American Monsoon (NAM) is the main driver of summertime climate variability in the American southwest. Previous studies of the NAM have primarily focused on the Tier I region of the North American Monsoon Experiment (NAME), spanning central-western Mexico, southern Arizona and New Mexico. This manuscript, however, presents a climatological characterization of summertime precipitation, defined as July, August, and September (JAS), in the Lake Mead watershed, located in the NAME Tier II region. Spatiotemporal variability of JAS rainfall is examined from 1981-2016 using gridded precipitation data and the meteorological mechanisms that account for this variability are investigated using reanalyses. The importance of the number of wet days (24-hr rainfall ≥1 mm) and extreme rainfall events (95^{th} percentile of wet days) to the total JAS precipitation are examined and show extreme events playing a larger role in the west and central basin. An investigation into the dynamical drivers of extreme rainfall events indicates that anticyclonic Rossby wave breaking (RWB) in the midlatitude westerlies over the US west coast is associated with 89% of precipitation events >10 mm (98^{th} percentile of wet days) over the Lake Mead basin. This is in contrast to the NAME Tier I region where easterly upper-level disturbances such as inverted troughs are the dominant driver of extreme precipitation. Due to the synoptic

nature of RWB events, corresponding impacts and hazards extend beyond the Lake Mead watershed and are relevant for the greater U.S. southwest.

2.1 Introduction

Enhanced knowledge of Colorado River basin hydrometeorology is necessary for effective water resource management throughout the arid Southwest US. This need is increasing in urgency given future projections of prolonged regional drought and growing water demand (*Colorado River Basin Water Supply and Demand Study: Executive Summary*, 2012). Accordingly, this manuscript presents a characterization of summertime meteorology over the Lake Mead watershed in the Lower Colorado River basin.

Lake Mead supplies water to over 25 million people for household use, agriculture and power generation across the American southwest (Rosen et al., 2012). While roughly 90% of annual inflow is generated via upstream releases from Lake Powell on the Colorado River (primarily fed by snowmelt in the Upper Colorado River basin), 10% of inflow is generated locally (Bunk, 2018), 25% of which occurs during the months of July, August, and September (JAS) (streamflow data available at https://waterdata.usgs.gov/usa/nwis/). Although the average annual inflow contributed by summertime precipitation within the Lake Mead watershed represents only a fraction of overall storage, multidecadal drought and historical over-allocation of existing water resources have placed the reservoir on the precipice of a litigated shortage threshold that, when crossed, will trigger delivery cut backs. As a result, interannual variability in this comparatively small inflow contribution by local summertime precipitation is highly relevant to overall water resource management and can be the difference between normal or historically unprecedented reservoir operations.

The precipitation events that generate summertime inflow to Lake Mead occur during the North American Monsoon (NAM) season. The NAM is the main driver of summertime climate variability in the region and is associated with a marked increase in precipitation during the months of July, August, and September (Adams & Comrie, 1997). Weather associated with the NAM can have devastating impacts on the built environment such as flooding, wind damage, dust storms, power outages, and crop loss (Brazel & Nickling, 1986; Ray et al., 2007). Apart from hazards, precipitation falling during the monsoon season is vital for ecosystem processes (Notaro et al., 2010) which can affect the surface energy balance (Vivoni, 2012; Watts et al., 2007) and feedback on summer precipitation (Dominguez et al., 2008; Small, 2001).

Meteorologically, the NAM is characterized by the development of a surface heat low and 500-hPa 'monsoon ridge' over the southwest U.S. (Adams & Comrie, 1997; Douglas, 1995; Douglas et al., 1993; Tang & Reiter, 2002). The subsequent seasonal reversal of winds and enhanced moisture transport into northwest Mexico and the southwestern US at this time are essential to the development of precipitation, though it has been demonstrated for the North American Monsoon Experiment (NAME) Tier I region that synoptic scale variability in the strength and position of the NAM ridge influence the organization and growth of convective systems and drive precipitation variability across a range of spatial and temporal scales (Bieda et al., 2009; Carleton, 1986, 1987; Fuller & Stensrud, 2000; R. W. Higgins et al., 2004; Johnson et al., 2007; Pascale & Bordoni, 2016; Pytlak & Goering, 2005; Stensrud et al., 1997). For example, the interactions between the monsoon ridge and easterly disturbances, such as inverted troughs, are often associated with moisture surges and extreme precipitation in southern Arizona and northern Mexico (Brenner, 1974; Hales, 1974; Lahmers et al., 2016; Pytlak &

Goering, 2005; Stensrud et al., 1997). Midlatitude westerly disturbances (e.g. cutoff lows, open wave troughs, shortwaves) have also been shown to produce synoptic forcing for ascent and low level moisture transport into the NAM region leading to extreme precipitation (Carleton, 1986; Corbosiero et al., 2009; Favors & Abatzoglou, 2013; Johnson et al., 2007).

Here, we investigate the role of synoptic disturbances on NAM precipitation in the Lake Mead watershed in the NAME Tier II region, where considerably less is known about the impact of the individual mechanisms discussed above (Higgins & Gochis, 2007). Motivated by the gap in understanding of hydrometeorology in the northern extent of the NAM, the ecological and societal impacts of monsoon rainfall, and declining Lake Mead reservoir elevations, the purpose of this manuscript is to examine the impact of summertime (JAS) precipitation on the Lake Mead watershed from a climatological perspective and to understand the synoptic drivers of regional extreme precipitation events.

2.2 Data and Methods

2.2.1 Watershed Subdivisions

To examine spatial variability across the Lake Mead watershed, USGS stream gages on major Lake Mead tributaries were used to define 7 sub-basins (Table 2.1, Fig. 2.1). For each tributary, the furthest downstream gage with the longest record of daily discharge was used to delineate the sub-basin boundary (except for the Colorado River, which was split into 2 watersheds using a single USGS gage).

2.2.2 Precipitation

Daily precipitation totals, defined as 12-12 UTC, were obtained from the PRISM 4-km gridded AN81d dataset for the period 1981-2016 (Daly et al., 1994). The individual sub-basins

are reasonably sampled by PRISM precipitation stations, although fewer exist in the proximity of the Grand Canyon. Although the onset and retreat of the NAM varies inter-annually, this work uses the months of July, August, and September (JAS) as a proxy for "monsoon season/summertime" which generally agrees with Bieda et al. (2009) for the NAME Tier II region. The spatial variability of seasonal (JAS) precipitation within the Lake Mead basin was examined in addition to the temporal variability of precipitation on sub-seasonal, seasonal, and interannual timescales. One such metric used to infer relative interannual variability is the coefficient of variation (c_v) hereby defined as c_v = standard deviation/mean. Note that this metric is always positive and normalizes the variability by the mean of a given distribution.

To understand the drivers of interannual variability in total JAS precipitation, the relationship between the number of wet days as well as accumulation from extreme and non-extreme precipitation to the total JAS precipitation were independently examined using Spearman's rank correlation. Extreme (non-extreme) events were categorized as the 95^{th} ($<95^{th}$) percentile of wet days, defined here as 24-hr mean basin precipitation ≥ 1 mm (Cavazos et al., 2008). Extreme events must be separated by more than one day to be considered independent and consecutive days $>95^{th}$ percentile were counted as a single event on the first extreme precipitation date. The contribution of the top 5% of wet days to the JAS precipitation total was assessed for each sub-basin and the entire Lake Mead watershed using the methodology of Dettinger and Cayan (2014).

2.2.3 Meteorology

Atmospheric reanalysis variables from NASA's Modern-Era Retrospective and Applications, Version 2 (Gelaro et al., 2017) were taken at 23 vertical levels from 1000-200 hPa at 0.5º x 0.625º horizontal resolution. Daily mean (12PM-12PM UTC) values were

computed by averaging across 3-hourly model output. Synoptic conditions for extreme events were examined via lagged composite analysis and on a case-by-case basis. Atmospheric conditions were examined 10 days prior through 1 day after each extreme precipitation event. Attention was focused on evaluating synoptic features identified in previous studies as important for southwest extreme precipitation, including: tropical easterly waves (Fuller & Stensrud, 2000; Stensrud et al., 1997), inverted troughs (Bieda et al., 2009; Pytlak & Goering, 2005), upper-level potential vorticity anomalies (Carleton, 1986; Pytlak & Goering, 2005), and 500-hPa ridge position (Carleton, 1986, 1987; Maddox et al., 1995; Watson et al., 1994), in addition to integrated water vapor (IWV), and integrated vapor transport (IVT) (Schmitz & Mullen, 1996).

Field significance for synoptic patterns was computed via bootstrapping with resampling in which the distribution of 5,000 randomly selected representative data is compared to an individual event or composite signal. If the individual event or composite signal falls beyond the top or bottom 2.5% of the randomly selected distribution, the signal is deemed statistically significant. Standard anomalies for the above variables were computed using the following formula, Standard Anomaly = (Data – Climatology)/Standard Deviation, where the climatology and standard deviation were computed using a centered 28-day window across the 36-year record at each grid point for each variable.

2.2.4 Tropical Cyclone Inventory

To quantify the importance of tropical cyclones to JAS precipitation in the Lake Mead watershed, intensity and position were taken from the International Best Track Archive for Climate Stewardship (IBTrACS) dataset (Knapp et al., 2010) to identify tropical cyclone (TC) tracks that passed through 28.5°N ± 2°N, 113.5°W ± 3°W. This region was chosen primarily to

identify and flag TCs which track northeast enough to directly influence precipitation over the study area and encapsulates the core region of TC tracks impacting the southwest in Corbosiero et al. (2009). Similar to Seastrand et al. (2015), precipitation falling within 7 days from the flagged date was assumed to be associated with the concurrent TC. Flagged dates were excluded from the extreme event synoptic composite and case-by-case study to investigate drivers of extreme precipitation apart from tropical storms, which can produce extreme precipitation events in the study region but are infrequent enough to necessitate separate consideration in the climatology.

2.3 Data and Methods

2.3.1 Climatology of JAS Precipitation

The average JAS total precipitation in the entire Lake Mead watershed is 103.0 mm ± 32.6 mm. Summertime rainfall maxima occur over high terrain features such as the Mogollon Rim, Kaibab Plateau, and other isolated peaks (Fig. 2.2). The highest average values are located in the southeastern basin, on the northern side of the Mogollon Rim, which bifurcates the low deserts of southwestern Arizona from higher terrain to the north. On the sub-basin scale, a strong increasing west-to-east gradient in average JAS precipitation exists with 57.2 mm ± 46.9 mm falling in the westernmost Las Vegas Wash sub-basin and 128.2 mm ± 33.0 mm in the easternmost Little Colorado sub-basin. In contrast, a strong decreasing west-to-east gradient exists in the coefficient of variation of average JAS precipitation. In general, the western sub-basins are drier on average with larger inter-annual variability while the eastern basins are wetter with smaller interannual variability (Table 2.2). Further, the fraction of annual water year (WY, October 1 – September 30) precipitation occurring during JAS over the entire Lake Mead

watershed is 36% ± 13%. A similar increasing west-to-east gradient is found with 29% of annual WY precipitation occurring in the Las Vegas Wash sub-basin compared to 44% over the Little Colorado (Table 2.2).

2.3.2 Relationship Between Number of Wet Days and Total JAS Precipitation

The total number of wet days during JAS explains 75% of the year-to-year variability in total summertime precipitation for the Lake Mead watershed. In contrast to the coefficient of variation and contribution to annual precipitation results shown above, a west-to-east trend is not apparent, with rank correlated r-squared values falling between 0.65 and 0.77.

The relationship between the mean total number of wet days during JAS and mean total JAS precipitation for each sub-basin is shown in Fig. 2.3 and demonstrates a distinct difference between the western and easternmost sub-basins' precipitation distributions (For an individual basin, mean values of each variable mark the center of an ellipse, and the distance from the center to the ellipse's edge in either direction represents ± 1 standard deviation of that variable. Data from individual years are shown in translucent dots). In the Las Vegas Wash basin, the narrow vertical ellipse indicates comparative greater variability in total JAS precipitation than in the number of wet days during JAS. By comparison, the basins in the center of the greater Lake Mead watershed have more proportional variability in each variable. The easternmost Little Colorado basin, as well as the entire Lake Mead watershed, is characterized by more consistent total JAS precipitation despite larger variability in the number of wet days. In general, basins increase in both total JAS precipitation and number of wet days moving from west-to-east.

2.3.3 Relationship Between Extreme Events and JAS Total Precipitation

For the entire Lake Mead watershed, the variance in total JAS precipitation explained by the top 5% (bottom 95%) of wet days is 46% (80%). Total variance explained exceeds 100% due to the correlation between precipitation regimes, i.e., years with extreme precipitation often have larger non-extreme totals. The average percentage of JAS precipitation falling as extremes ranges from 12-17%, with slightly higher values in the eastern sub-basins. When the percentage of total JAS precipitation from 1981-2016 falling as extremes is examined, western and central basins are more strongly influenced, with 24.6% of all precipitation due to extremes in the Las Vegas Wash and the combined watershed receiving 17.6% (Table 2.2).

2.3.4 Seasonality of Extreme Events and Tropical Cyclones

The monthly distribution of independent extreme precipitation events in the Lake Mead basin exhibits a skewness towards the end of the monsoon season (Fig. 2.4). In fact, the Little Colorado is the only sub-basin for which July is not the month with the lowest frequency of extreme events, irrespective of TC inclusion. Concerning TCs, which occur preferentially towards the end of the JAS period, extreme (non-extreme) precipitation events are associated with 29% (67%) of systems that tracked into the region of influence (described in Section 2.2.4). While it is noteworthy that TCs are associated with a greater fraction of both extreme and non-extreme events in the eastern Lake Mead basin than the west, a thorough analysis of their meteorology and hydrologic impacts on the Tier II region is beyond the scope of this paper.

2.3.5 Dynamical Drivers of Extreme Events

The meteorological conditions leading to extreme precipitation events, excluding TC

events, for each sub-basin as well as the combined Lake Mead basin were investigated using lagged composite and individual event analyses. Lagged composites show a weak westerly disturbance signal (not shown), though considerable variance necessitated a review of each individual event's meteorology. Further qualitative inspection of daily mean fields for each case revealed 4 distinct synoptic regimes: inverted trough, Rossby wave breaking in the midlatitude westerlies, tropical storm influence for non-TC flagged date, and uncharacterized.

Criteria for the above categories are as follows: *Inverted Trough (IV)*: westward moving 200-hPa positive potential vorticity (PV) standard anomaly > 0.25 on the southern side of the NAM ridge (Lahmers et al., 2016) poleward of 15 ^{o}N. *Rossby Wave Breaking (RWB)*: eastward moving 200-hPa positive PV standard anomaly > 0.25 in midlatitudes with mandatory overturning of 2 PV Unit (PVU) contour (Abatzoglou & Magnusdottir, 2006; Postel & Hitchman, 1999; Thorncroft et al., 1993). *Tropical Storm (TS)*: moisture surge coinciding with northward moving cyclonic feature off Baja coast, likely a tropical disturbance no longer tracked by iBTrACS and not associated with RWB or IV synoptics. *Uncharacterized*: no clear synoptic upper level forcing mechanism, excessive moisture and low-mid level disturbances are possible.

RWB events were split into three groups: 'canonical', 'TC tapping', and 'irregular' events. Canonical and TC tapping events feature clean Rossby wave breaking (e.g. Abatzoglou and Magnusdottir, 2006 (note their Fig. 3); Barnes and Hartmann, 2012 (note their Fig. 2)), with the latter potentially advecting moisture from a distinct cyclonic feature outside of the control box described in Section 2.2.4. Irregular RWB events feature an overturning of the 2 PVU contour, but with a less organized large-scale background flow. It is important to note that events were categorized using daily mean fields and analysis performed on higher temporal

resolution data, ex. 3-hourly fields, may yield slightly different results. For example, an 'irregular' RWB here may look 'canonical' at higher resolution. However, changes to the large-scale synoptic categorization of events are unlikely.

Out of 40 independent extreme events for the combined Lake Mead watershed, 70% are classified as RWB events (canonical-22.5%, TC tapping-17.5%, irregular-30%). Conversely, IVs are associated with 20% of all extreme events while TS and Uncharacterized events each comprise 5% of cases. Results for sub-basins elucidate a similar trend with RWB playing a more dominant role than IVs in extreme events. The subjective analysis here suggests a preference for IV extreme events to occur early in the summer, peaking in July, waning in August, and absent for September. In contrast, RWB events play an increasing role as the summer progresses, associated with ~40-50% of July events compared to ~90% of events in September. Independent extreme precipitation event dates for the combined Lake Mead watershed are listed by synoptic category in Table 2.1A in Appendix A. On occasions where both a RWB and IV were identified (n=2), preference was given to the most salient feature; one case was a RWB, the other an IV.

The extreme event on September 23, 2007 is an example of a canonical Rossby wave break event (Fig. 2.5). Here, the anticyclonic wave break 3 days prior to the event (Fig. 2.5 a) produced a quasi-stationary cutoff low centered over the California Bight while simultaneously transporting significant amounts of water vapor poleward on the western flank. Although not all RWB events produce a cutoff low, the feature is common and the location of the positive (negative) 200-hPa PV (500-hPa height) anomaly is located to the west of the Lake Mead watershed. As the westerly trough dropped into the coastal region, the 500-hPa NAM ridge receded to the east. The resulting south/southwesterly synoptic-scale flow advected warm,

moist air into the Lake Mead watershed providing necessary moisture for extreme precipitation. The progression of the northern edge of the 33-mm integrated water vapor (IWV) contour demonstrates the surge of moist air into the region (Fig. 2.5 b,c) as a direct result of the anomalous cyclonic circulation. Lastly, quasigeostrophic dynamics associated with the cutoff low and leading edge of the positive PV anomaly can act as a trigger for intense convective storms (Hoskins et al., 1985; Martius & Rivière, 2016). The 24 and 72-hour precipitation fields from this event can be viewed in the supplemental as in Appendix B as Figures 2.1B and 2.2B respectively. This example serves to illustrate the general mechanisms by which an anticyclonic RWB generates extreme precipitation in the summertime southwestern US, though the specific meteorology of any given RWB event is variable.

Lead-lag composite analysis was performed on the combined 'canonical' and 'TC tapping' RWB subset of extreme events for the combined Lake Mead watershed (Fig. 2.6). The composited atmospheric features are not sensitive to the choice of sub-basin as the large-scale patterns for extreme precipitation are similar across the watershed. The composites do not depict a robust overturning of PV contours seen in Figure 2.5 on account of variability in the location, timing, and axis of the wave break between events. Despite the weakened composite signal at long lead times, the synoptic features of a RWB are apparent with decreasing lead time and at the time of the precipitation event: co-located 200-hPa PV and 500-hPa geopotential anomalies over the Southern California Bight, moist SSW flow into the American southwest, and a distinct Rossby wave pattern spanning the eastern Pacific and US. It is worth noting that although the moist SSW flow is driven by the cyclonic circulation associated with the RWB, anticyclonic circulation (SSE flow) around an eastward displaced NAM ridge amplifies it. Further, the west-east dipole of cyclonic and anticyclonic circulation favors upper level

divergence that is conducive for ascent over the Lake Mead watershed (Holton, 2004). The composited days comprise 40% of JAS extreme events over the combined Lake Mead watershed, demonstrating the importance of midlatitude westerly disturbances to extreme precipitation in the NAME Tier II region.

To contrast RWB precipitation generation to inverted trough (IV) events, which are known to impact southern Arizona (Douglas & Englehart, 2007; Finch & Johnson, 2010; Pytlak & Goering, 2005), lead-lag composite analysis was applied to the IV subset of events for the combined Lake Mead watershed (Fig. 2.7). As in the RWB analysis, the composited large-scale atmospheric features are not sensitive to the choice of sub-basin as the general synoptic patterns for extreme precipitation are similar across the watershed. However, the composited IV signal is less robust than the RWB as there is greater variability in the strength and location of the upper-level disturbance across the 8 individual IV events. At 2-3 days lead, the composites depict an easterly PV anomaly at 200-hPa with a weak 500-hPa geopotential height trough moving across northern Mexico on the equatorward side of a strengthened northward-displaced NAM ridge (not shown). From here, the monsoon ridge retreats eastward as the upper-level disturbance turns northward near the Baja Peninsula. The day of event composite features significant moisture transport into the Lake Mead watershed from the south-southeast as the co-located 200-hPa PV and 500-hPa anomalies move northward across the US-Mexico border. In addition to the northward moving upper-level disturbance, the day of event composite depicts a second 200-hPa positive PV anomaly off of the California coast whose ensuing circulation can help steer the primary disturbance towards the Lake Mead watershed (seen in several individual events). The composite 24-hour precipitation field for RWB and IV cases can be seen in the supplemental as Figures 2.3B and 2.4B respectively.

To contrast the temporal evolution of RWB and IV events, composite Hovmöller plots of 200-hPa PV, 700-hPa meridional wind (V700hPa), and IWV are shown for each event type (Fig. 2.8). The composites include 16 RWB and 8 IV events that produced extreme precipitation in the combined Lake Mead watershed. Because driving RWB and IV dynamics tend to occur in distinct latitudinal bands, each regime's PV field is averaged over its characteristic domain (detailed in Fig. 2.8). The latitudinal averaging band for the RWB composite (32°N-45°N) is consistent with the region of >0.5 standard anomaly in Figure 2.6 and that of the IVs (25°N - 35°N) is consistent with previous IV tracking work and highlights the northern portion of the domain used in Lahmers et al. (2016).

The RWB PV composite Hovmöller shows a distinct westerly wave with a couplet of maximum amplitude centered over the watershed on the day of extreme precipitation with an eastward propagation speed of roughly 350 km day^{-1} (Fig. 2.8a). Dynamical forcing associated with the advection of positive PV at the feature's leading edge is conducive to ascent and likely plays a role in driving these extreme precipitation events (Hoskins et al., 1985; Martin, 2006; Martius & Rivière, 2016). The evolution of V700hPa depicts significant circulation anomalies corresponding to the breakdown and eastward retreat of the NAM ridge due to an approaching midlatitude westerly disturbance (Fig. 2.8b). The evolution of IWV features a plume of moisture developing over the watershed several days prior to the event before reaching a maximum on the day of the event and then moving eastward (Fig. 2.8c).

In contrast, the PV composite for IV events features an easterly trough whose signal is evident several days prior to the extreme event. Both the primary easterly disturbance and the emergence of a secondary offshore PV anomaly can be seen (Fig. 2.8a). Anomalous southerly winds approaching the basin from the east are representative of an easterly disturbance in

synchrony with an eastward or northward displaced NAM ridge (Fig. 2.8b). The IWV signal for the IVs emerges from the east ~3 days prior near 110°W and continues westward through the day of extreme precipitation (Fig. 2.8c).

2.4 Discussion

Deconstructing the Lake Mead watershed into sub-basins reveals dramatic gradients in summertime (July, August, and September (JAS)) precipitation characteristics. Not only are the southeastern sub-basins wetter than the northwestern, on average, they experience a greater fraction of water year precipitation during the summer months and less interannual variability of summer precipitation. Using a threshold of 1 mm, the influence of the number of wet days on JAS accumulated precipitation exhibits no spatial trend with rank correlated r-squared values falling between 0.65 and 0.77.

However, the role of extreme precipitation events in driving JAS total accumulation varies geographically in the Lake Mead basin with heightened importance in the central and western sub-basins with 17.6% of 1981-2016 JAS precipitation falling during extreme events for the combined Lake Mead watershed. Concerning the seasonality of extreme events, a skewness exists with distributions peaking in August or September across all sub-basins. While this timing corresponds to increased tropical storm activity in the late summer, we find the relationship to hold when excluding tropical storms tracking within 28.5°N ± 2°N, 113.5°W ± 3°W from our analyses, suggesting landfalling tropical storms and their remnants are not the most frequent drivers of extreme precipitation in the late summer.

Case-by-case analyses of synoptic fields for each extreme event reveal anticyclonic Rossby wave breaking (RWB) in the midlatitude westerlies to be the dominant source of JAS

extreme precipitation events in the entire Lake Mead watershed (70% of events from 1981-2016). Interestingly, when the precipitation threshold for an extreme event is raised from the 95th percentile (7.4 mm) to 10 mm (98th percentile), the fraction of RWB events increases from 70% to 89% indicating that RWB are associated with the most extreme summertime precipitation in the Lake Mead basin. The RWB results in a trough over the US west coast whose equatorward extent can reach as far south as 30^{o}N (e.g., Fig. 2.5). The ensuing circulation is able to advect moisture into the southwest, priming the region for instability and precipitation. Further, eastward displacement of the 500-hPa NAM ridge results in a circulation dipole centered over the southwest, enhancing moisture transport from the south and favoring upper level divergence. Finally, strong quasi-geostrophic dynamics on the leading flank of the positive potential vorticity (PV) anomaly can force ascent and trigger convection (Hoskins et al., 1985; Martin, 2006; Martius & Rivière, 2016).

Previous work has noted the role of midlatitude westerly disturbances in both aiding (Carleton, 1986; Corbosiero et al., 2009; Favors & Abatzoglou, 2013; Johnson et al., 2007) and suppressing (Douglas & Englehart, 2007; Fuller & Stensrud, 2000) moisture influx and precipitation in the NAM region. This manuscript builds upon the former body of work arguing that an upstream midlatitude trough is not only able to facilitate the advection of moist air into the NAM region, but also contribute favorable dynamics for extreme precipitation. New to the understanding of extreme events in the NAM region is the importance of anticyclonic Rossby wave breaking on the genesis of cutoff and closed lows. While earlier work has demonstrated the link between RWB and cutoff lows (Baray et al., 2003; Ndarana & Waugh, 2010; Nieto et al., 2008; Scott et al., 2001) and the ability of RWB (Hoskins et al., 1985; Martius & Rivière, 2016) and cutoff lows (Abatzoglou, 2016; R. Nieto et al., 2008; Oakley & Redmond, 2014) to

affect extreme precipitation, these works have not demonstrated the importance of these mechanisms during the NAM season, especially as they relate to Tier II.

In southern Arizona and the NAME Tier I region, tropical easterly waves (TEWs) and inverted troughs (IVs) are important to extreme precipitation and convective outbreaks (Mazon et al., 2016; Pytlak & Goering, 2005). Although these transient disturbances are associated with extreme precipitation north of the Mogollon Rim, this flow regime is only associated with 20% of extreme events for the combined Lake Mead watershed. As seen in Bieda et al. (2009) and Pytlak & Goering (2005), Lake Mead was impacted by IVs both originating south of 30^{o}N in the Gulf of Mexico region as well as those generated in the midlatitude westerlies which became entrained in the tropical easterlies upon RWB on the east side of the NAM ridge.

When placing the Lake Mead watershed in the geographical context of previous literature highlighting extreme summertime precipitation, it appears to be located at a hinge point of synoptic forcing. IV track density peaks over central Mexico and the southern tip of Baja California which results in greater impacts (cloud-to-ground lightning, precipitation) south of the Mogollon Rim in northern Mexico and southern Arizona (Bieda et al., 2009; Lahmers et al., 2016). In contrast, the seasonal fraction of summertime precipitation from closed and cutoff lows in the interior western US increases from south to north, with distinctly higher values seen north of the Arizona-Utah border (Abatzoglou, 2016; Oakley & Redmond, 2014). The Lake Mead watershed, and the broader region straddling the northern NAME Tier I-II boundary, is uniquely positioned to experience the dominant synoptic drivers of extreme summertime precipitation of both the intermountain west and the core of the NAM region.

Idealized schematics of both RWB and IV events driving extreme precipitation in the Lake Mead basin are depicted in Figure 2.9, though the specific meteorology of any given event

is variable. In accordance with a strengthening of the monsoon ridge, due to thermal expansion of the lower atmosphere with increasing global temperatures (Christidis & Stott, 2015; Pascale et al., 2016), it is worth investigating whether there will be a future change in the prevalence of IVs impacting the Lake Mead region as these features may be displaced southward and westward away from the locus of high pressure (Lahmers et al. 2016; their Fig. 18). The subjective analysis here suggests a preference for IV extreme events to occur early in the summer, peaking in July, waning in August, and absent for September for the combined Lake Mead watershed, which resembles the seasonality of IV days presented in Lahmers et al. (2016) and Bieda et al. (2009). In contrast, RWB events make up roughly 90% of September events but play a lesser role in July (~40-50%). The transition from boreal summer to fall is associated with a strengthening of the Pacific westerly jet and the propensity for later season RWBs coincides with an easterly shift in the jet exit region and corresponding eastward shift in the location of RWB (Abatzoglou & Magnusdottir, 2006). Noting that RWB events tend to occur later in the summer season, it may be useful to look beyond JAS into the fall and early winter to better understand the impact of RWB on precipitation throughout the southwest. In addition to facilitating extreme weather on the eastern flank, dynamics on the western side of anticyclonic RWB events can result in significant poleward transport of water vapor, as seen in Fig. 2.5a, with potential impacts on precipitation and radiative forcing in the Arctic (Liu & Barnes, 2015; Stramler et al., 2011).

Further, the timing of peak RWB frequency (Abatzoglou & Magnusdottir, 2006) coincides with increased tropical storm activity in the tropical eastern Pacific (Corbosiero et al., 2009). Although extreme events corresponding to TCs tracking close to the head of the Gulf of California were removed, cyclonic circulation associated with RWB can tap into tropical

moisture from already-decayed systems or those whose tracks are south or southwest of our control box. A sensitivity test indicated a southwestward expansion of our control box has little impact on the number of extreme events removed or their seasonality. However, as noted in previous work (Corbosiero et al., 2009; Garza, 1999; K. M. Wood & Ritchie, 2014), tropical systems that do impact western Mexico and the southwestern US typically gain their northward motion from a deep equatorward penetration of a midlatitude trough, making the study of RWB tropical-extratropical interactions in the region relevant to the broader scientific community.

The results from this study are applicable beyond the Lake Mead watershed. Depending on the orientation of the RWB axis and whether the resulting PV anomaly is advected to the northeast by the steering flow, intense precipitation can reach into the interior west. In fact, several events in the Virgin sub-basin corresponded to heavy precipitation in the Salt Lake City, UT area and one canonical RWB that tapped into a weakening tropical depression resulted in near-record floods on the Rillito River outside of Tucson, AZ (Saarinen et al., 1984). The RWB event from Figure 2.5 produced widespread heavy precipitation (over 50 mm falling in California, Nevada, Arizona, and Utah) resulting in 43% of the JAS mean in the Virgin sub-basin and 19% for the entire Lake Mead watershed. Along with hail, flash flooding, and even a tornado report in Orange County, CA., (National Oceanic and Atmospheric Administration Storm Events Database; see online at https://www.ncdc.noaa.gov/stormevents) the intense precipitation associated with this system also drove a post-fire debris flow in Los Angeles, CA (Cannon et al., 2011). This example clearly shows the ability of RWB to drive extreme precipitation, meaningful streamflow generation, and high impact weather in the Lake Mead basin and beyond.

2.5 Concluding Remarks

This work presents a climatological characterization of summertime precipitation in the Lake Mead watershed, located in the NAME Tier II region, spanning from 1981-2016. The importance of the number of wet days (24-hr rainfall ≥1 mm) and extreme rainfall events (95th percentile of wet days) to the total JAS precipitation is examined and shows a strong west-to-east gradient of JAS precipitation with extreme events playing a larger role in the central and west basin. Anticyclonic Rossby wave breaking (RWB) over the US west coast is found to be the dominant synoptic driver of extreme summertime precipitation in the Lake Mead watershed. As the Lake Mead basin sits on the northern periphery of the more-studied North American Monsoon Experiment (NAME) Tier I region, this result highlights the different mechanisms associated with extreme precipitation to the north and south of the Mogollon Rim and may prove relevant for the greater NAME Tier II region.

Although some impacts of RWB on extreme precipitation in the Colorado River basin from a hydroclimate and flood risk standpoint are demonstrated here, there remains much to be learned. Earlier work has demonstrated that the lack of snowmelt and flashy nature of lower Colorado basin tributaries makes streamflow forecasting difficult (Shafer & Huddleston, 1984), however improving hydrologic model forcing (i.e. precipitation forecasting) may yield more accurate streamflow predictions (Franz et al., 2003). Noting the frequent collocation with cutoff lows, which have been associated with substantial forecast difficulty (Nieto et al., 2005; Smith et al., 2002), understanding the atmospheric regimes conducive to RWB over the US west coast may help improve accompanying precipitation and streamflow forecasts in the greater NAM region. Moving forward, it will be important employ a climatological framework to understand

the necessary conditions (location/strength of upper level low, land surface moisture, local sea surface temperatures, etc.) for a RWB event to facilitate extreme precipitation in the southwestern United States.

Looking towards the future, Oakley & Redmond (2014) note that since short to medium-range numerical weather prediction models have difficulty regarding closed lows associated with RWB, long-term climate models likely face serious issues in representing these features as well. Further, uncertainties in the latitudinal position of the eddy driven jet and subsequent impacts on anticyclonic RWB (Barnes & Hartmann, 2012) make the study of future RWB impacts on summertime precipitation in the NAM region challenging. Despite this, it is important to determine if and how RWB frequency over this region will be affected by a changing climate. Shifts in the longitudinal location, equatorward extent, and intensity of RWB will impact their ability to act as moisture conduits from the tropics to the NAM region and drive extreme precipitation, with potential implications for the future state of regional water resources.

2.6 Acknowledgements

This research was supported by the US Army Corps of Engineers, grant number USACE W912HZ-15-2-0019, and the CA Department of Water Resources, grant number 4600010378 TO#15 Am 22. The authors thank William Chapman for providing statistical guidance and Chad Hecht for illuminating synoptic discussions.

Chapter 2, in full, is a reprint of the material as it appears in Sierks, M. D., Kalansky, J., Cannon, F., & Ralph, F. M. (2020). Characteristics, Origins, and Impacts of Summertime Extreme Precipitation in the Lake Mead Watershed. Journal of Climate. © American

Meteorological Society. Used with permission. The dissertation author was the primary investigator and author of this paper.

Table 2.1. USGS gage ID and geographical characteristics of the delineated sub-basins and the entire Lake Mead watershed

Watershed	Abbreviated Name	USGS Gage ID	Area (km^2)	Mean/Maximum Elevation (m)
1) Las Vegas Wash	LVW	09419700	4,900	1,222/3,601
2) Muddy River	MUD	09419000	18,200	1,624/3,479
3) Lower Lake Mead	LLM	09404200	19,500	1,047/2,463
4) Virgin River	VIR	09415000	12,700	1,575/3,225
5) Paria River	PAR	09382000	3,700	1,874/3,135
6) Grand Canyon	GCN	09404200	25,300	1,761/3,156
7) Little Colorado River	LCO	09402000	68,000	1,922/3,836
Combined Watershed	--	--	152,300	1,676/3,836

Table 2.2: Precipitation characteristics of the delineated sub-basins and the entire Lake Mead watershed.

Watershed	Average JAS Precipitation (mm)	WY Fraction during JAS	Coefficient of Variation	1981-2016 JAS Minimum (Year)	1981-2016 JAS Maximum (Year)	Average Percent of JAS Precipitation Falling as Extremes	Percentage of Total JAS Precipitation Falling as Extremes (1981-2016)
8) LVW	57 ± 47	0.29	0.82	9.7 (2010)	230.7 (1984)	12 ± 22	24.6
9) MUD	68 ± 38	0.25	0.56	17.1 (1995)	167.2 (1984)	14 ± 18	20.4
10) LLM	69 ± 22	0.30	0.48	21.8 (1993)	142.4 (1984)	14 ± 19	19.6
11) VIR	99 ± 43	0.30	0.44	36.1 (2009)	187.1 (2004)	16 ± 18	20.9
12) PAR	101 ± 40	0.34	0.40	41.0 (2009)	190.6 (2003)	17 ± 17	21.0
13) GCN	126 ± 43	0.35	0.34	51.5 (2009)	215.2 (2013)	17 ± 14	19.9
14) LCO	128 ± 33	0.44	0.26	54.1 (2009)	203.0 (1999)	17 ± 13	17.8
Combined Watershed	103 ± 33	0.36	0.32	42.5 (2009)	181.2 (1984)	15 ± 12	17.6

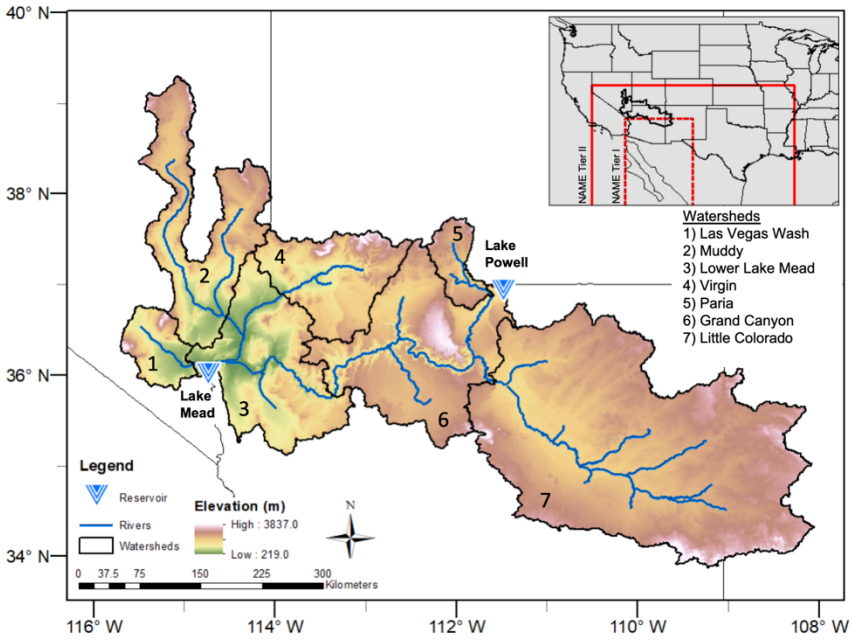

Figure 2.1. Topography of the Lake Mead watershed including major tributaries and their sub-basins. Northern extent of NAME Tier I and II regions and extent of entire Lake Mead watershed below Lake Powell shown in inlay for reference.

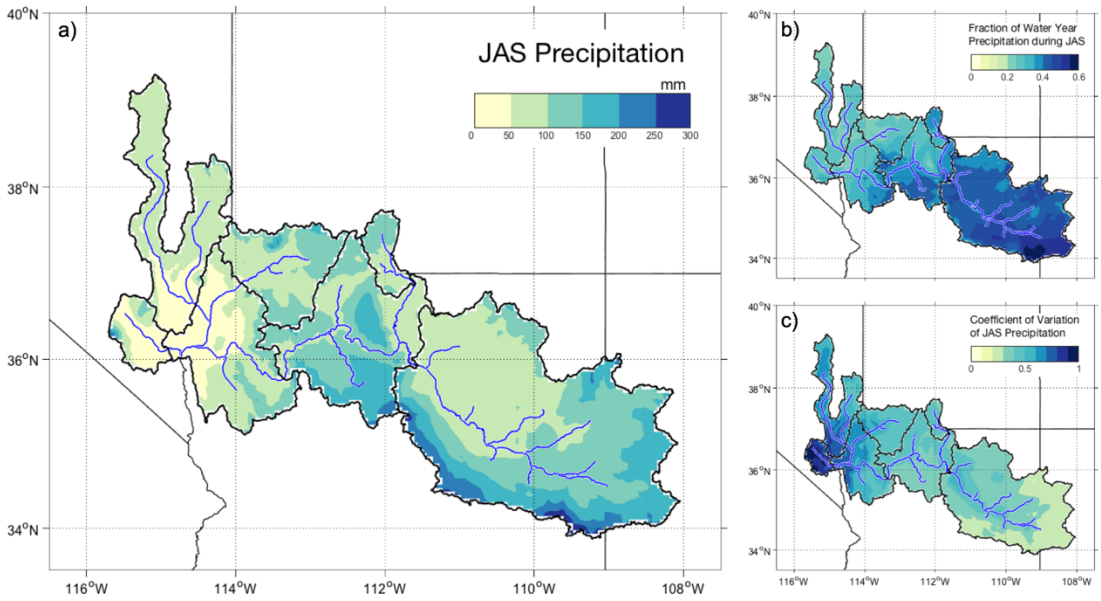

Figure 2.2. Average characteristics for sub-basins for (a) JAS precipitation, (b) fraction of water year precipitation during JAS, and (c) coefficient of variation of JAS precipitation derived from daily PRISM precipitation from 1981-2016.

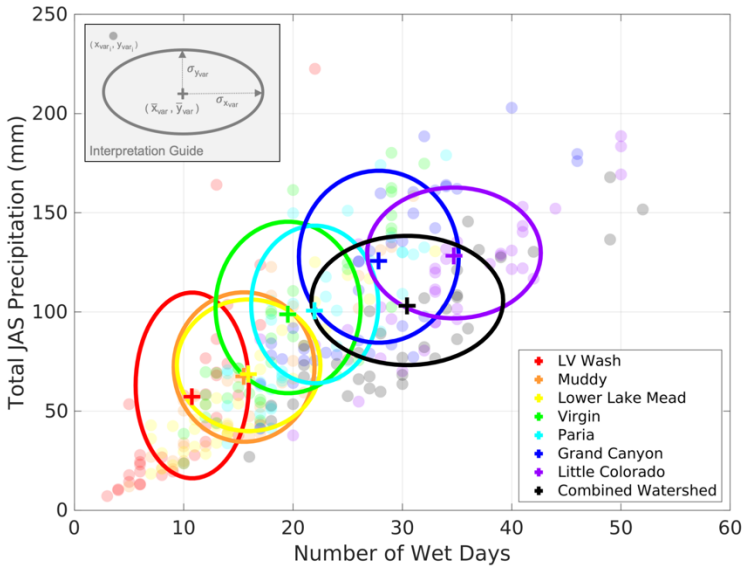

Figure 2.3. Relationship between total seasonal JAS precipitation and number of wet days per JAS for each basin. 36-year mean values are denoted by "+" and individual years by translucent markers. The distance from the center of an ellipse to its edge in either axis dimension represents one standard deviation of that variable. Basins are ordered west-to-east corresponding to warm-to-cool colors.

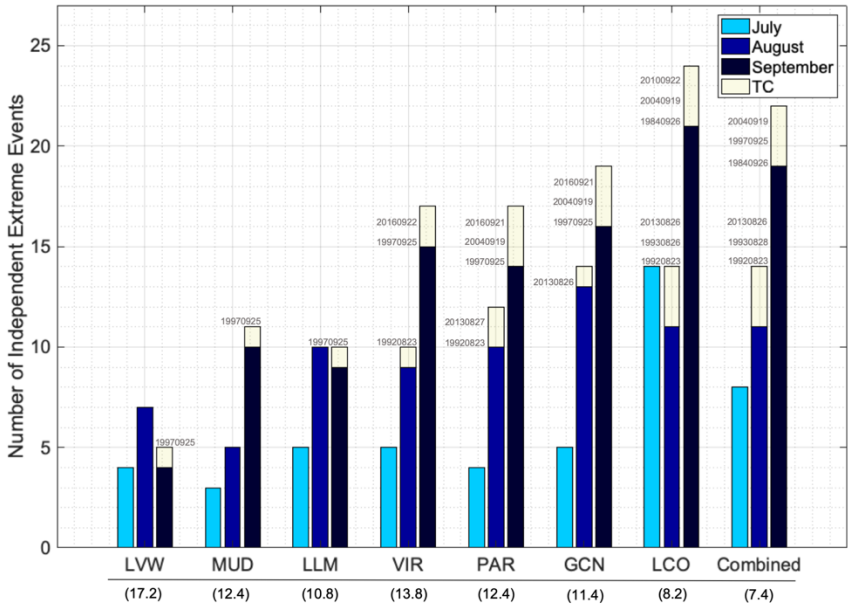

Figure 2.4. Seasonal distribution of extreme events color-coded by month for each sub-basin with 95th percentile precipitation values (mm) shown in parentheses. Extreme events within 7 days of tropical systems tracking within 28.5^{o}N ± 2^{o}N and -113^{o}E ± 3^{o}E are denoted with corresponding event date in grey. Extreme precipitation events affecting multiple sub-basins are counted once for each sub-basin.

Figure 2.5. Example of a ‘canonical’ Rossby wave break extreme precipitation event. 200-hPa potential vorticity standardized anomaly (shaded), 200-hPa potential vorticity (black contours, shaded every 2 PVU starting at 2 PVU), and IWV (blue contour denoting 33-mm isoline) for (a) 20 Sep 2007, (b) 21 Sep 2007, (c) 22 Sep 2007, and (d) 23 Sep 2007. The extreme precipitation event occurred on 23 Sep 2007. IVT vectors significant at the 95th percentile are shown. Stippling indicates statistical significance of 200-hPa PV standard anomaly at the 95th percentile. The Lake Mead watershed is outlined in a thin black line.

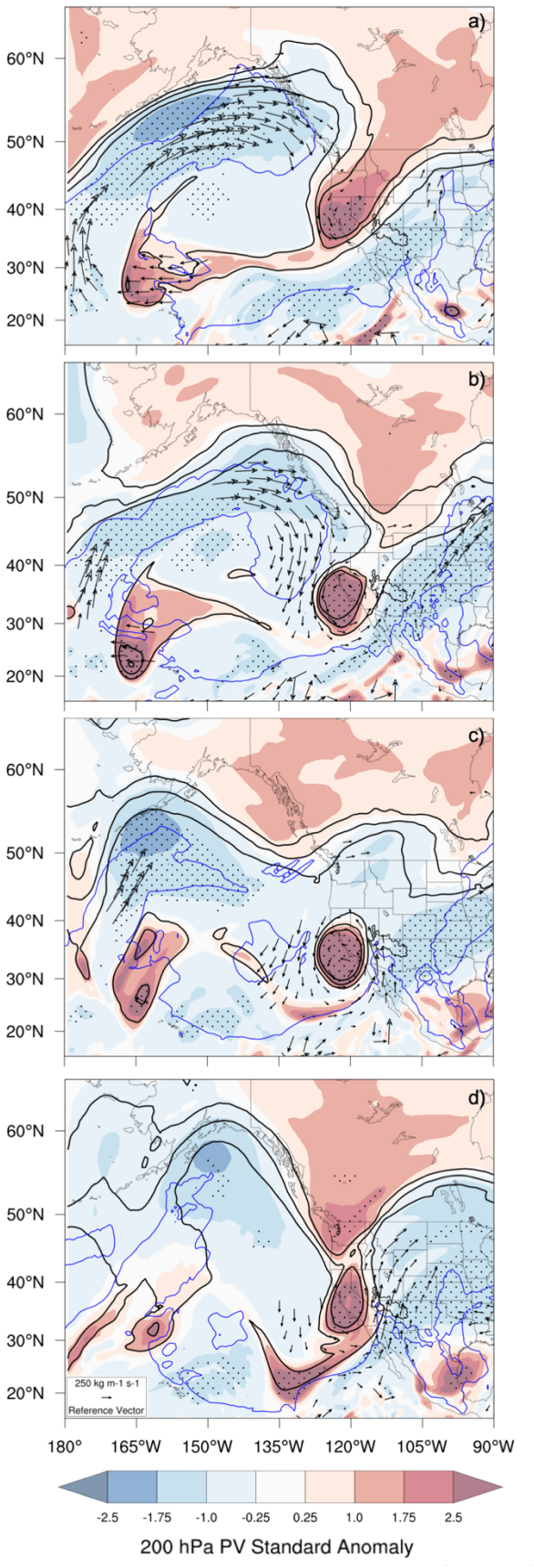
a)
b)
c)
d)
60°N
50°N
40°N
30°N
20°N
180°
165°W
150°W
135°W
120°W
105°W
90°W
250 kg m-1 s-1
Reference Vector
-2.5
-1.75
-1.0
-0.25
0.25
1.0
1.75
2.5
200 hPa PV Standard Anomaly

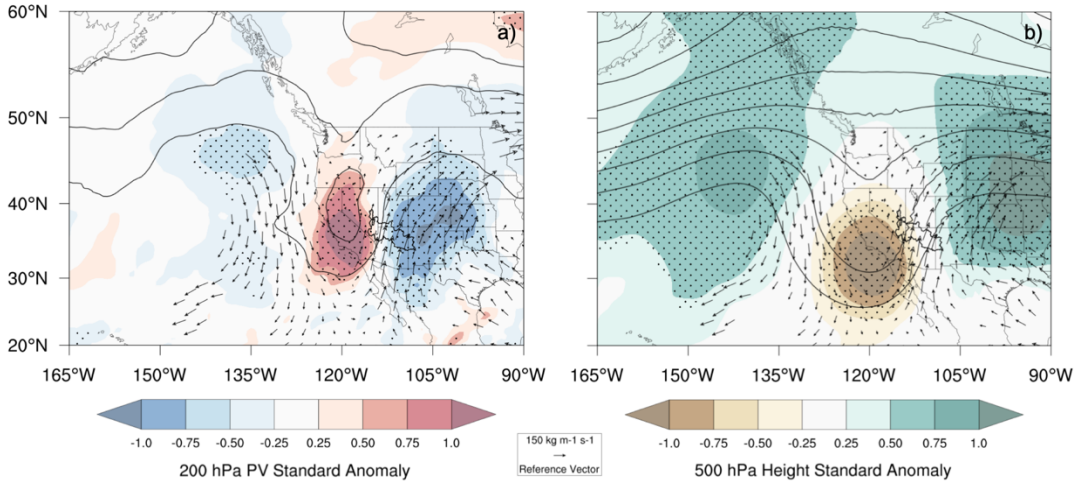

Figure 2.6. Composite fields for combined 'canonical' and 'TC tapping' RWB cases (n=16) in the combined Lake Mead watershed on day of extreme precipitation for (a) 200-hPa potential vorticity standardized anomaly (shaded), 200-hPa potential vorticity (black contours, shaded every 2 PVU starting at 2 PVU), and (b) 500-hPa geopotential height standardized anomaly (shaded), 500-hPa geopotential height (black contours, shaded every 50 m starting at 5850 m). IVT vectors significant at the 95th percentile are shown. Stippling indicates statistical significance of standard anomaly field at the 95th percentile. The Lake Mead watershed is outlined in a thin black line.

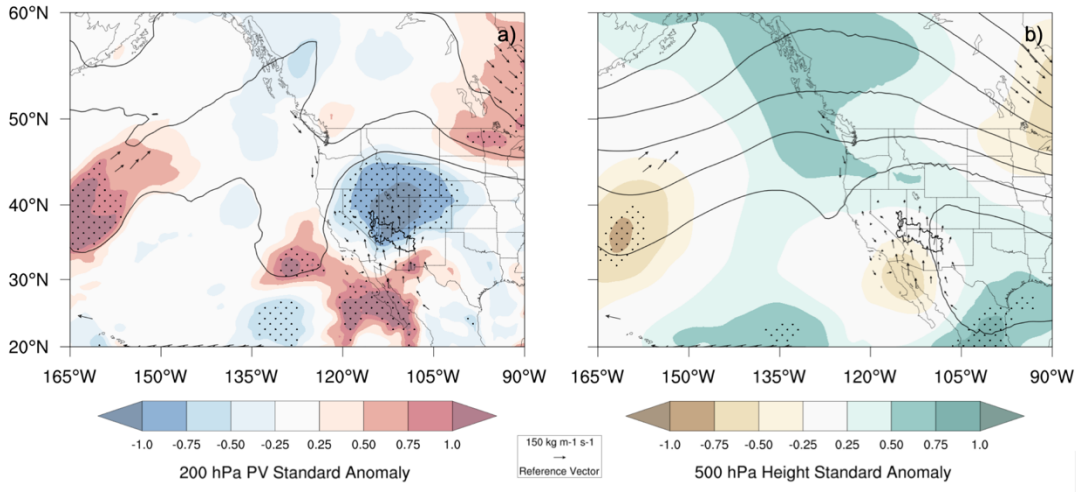

Figure 2.7. Composite fields for IV cases (n=8) in the combined Lake Mead watershed on day of extreme precipitation for (a) 200-hPa potential vorticity standardized anomaly (shaded), 200-hPa potential vorticity (black contours, shaded every 2 PVU starting at 2 PVU), and (b) 500-hPa geopotential height standardized anomaly (shaded), 500-hPa geopotential height (black contours, shaded every 50 m starting at 5850 m). IVT vectors significant at the 95th percentile are shown. Stippling indicates statistical significance of standard anomaly field at 95th percentile. The Lake Mead watershed is outlined in a thin black line.

Figure 2.8. Hovmöller plots of standardized anomalies for (a) 200-hPa potential vorticity, (b) 700-hPa meridional wind, (c) integrated water vapor. RWB events (n=16) are composited in the left column and IV events (n=8) on the right for extreme precipitation events for the combined Lake Mead watershed. Stippling indicates statistical significance of the standardized anomaly field at the 95th percentile.

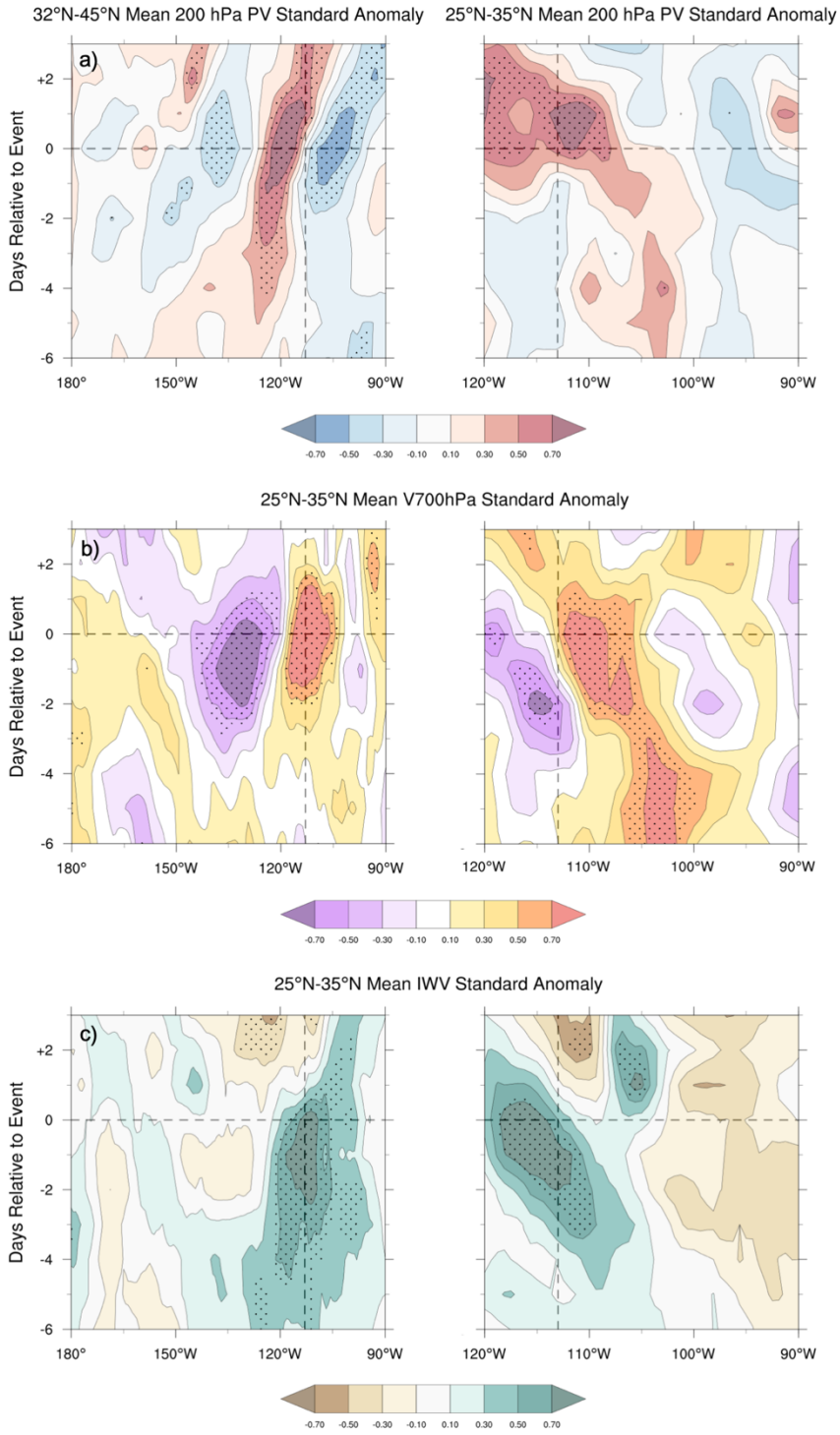
32°N-45°N Mean 200 hPa PV Standard Anomaly
25°N-35°N Mean 200 hPa PV Standard Anomaly
a)
Days Relative to Event
+2
0
-2
-4
-6
180°
150°W
120°W
90°W
120°W
110°W
100°W
90°W
-0.70 -0.50 -0.30 -0.10 0.10 0.30 0.50 0.70
25°N-35°N Mean V700hPa Standard Anomaly
b)
25°N-35°N Mean IWV Standard Anomaly
c)

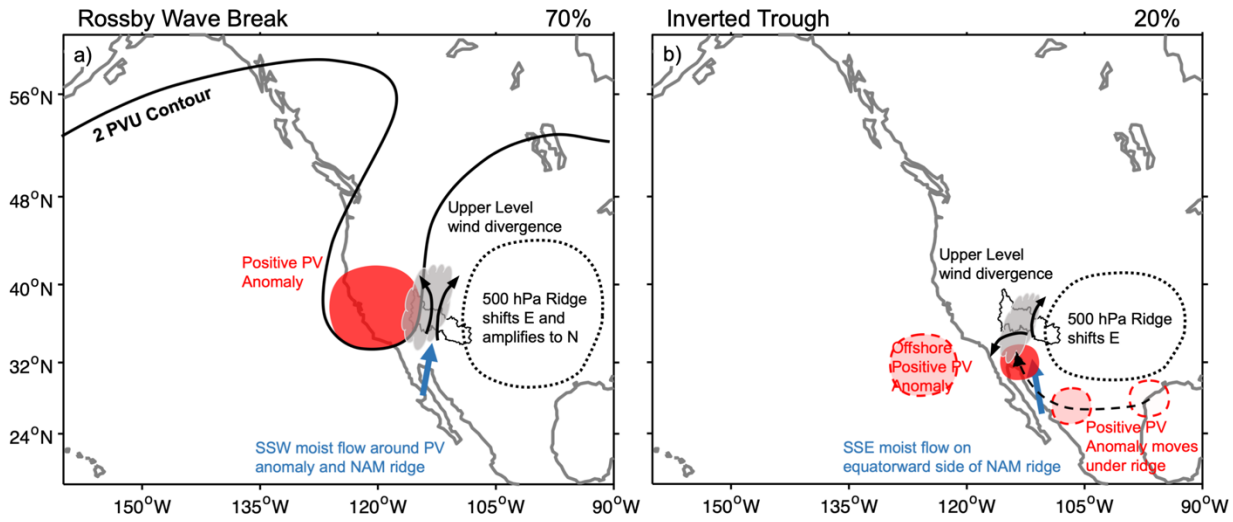

Figure 2.9. Idealized synoptic set-ups for primary drivers of extreme precipitation in the Lake Mead watershed, (a) RWB (b) IV (adapted from Pytlak et al., 2005), and their corresponding characteristic meteorology. The fraction of extreme events for the entire Lake Mead watershed associated with each regime is denoted above each panel. The Lake Mead watershed is outlined in a thin black line.

2.7 Appendix A: Extreme Precipitation Events by Synoptic Categorization

Following the criteria described in Section 2.3.5, the date and synoptic categorization of individual extreme precipitation events impacting the entire Lake Mead watershed are given below. Note that tropical cyclones have been removed prior to analysis as noted in Section 2.2.4.

Table 2.1A: Independent extreme precipitation event dates for the combined Lake Mead watershed as categorized by synoptic processes defined in Section 2.3.5.

RWB 'canonical'	RWB 'TC Tapping'	RWB 'irregular'	Inverted Trough	Tropical Storm	Uncharacterized
19810810	19830817	19810906	19820824	19900816	19820813
19840723	19830930	19820911	19830725	19980905	20160804
19850919	19860924	19830924	19860722		
19900923	20020908	19870717	19980723		
19970811	20020911	19870721	19990709		
19980912	20070923	19870818	20000830		
20120822	20140909	19910906	20130727		
20130910		19940903	20140804		
20140928		19970904			
		20120912			
		20140820			
		20150808			

2.8 Appendix B: Precipitation Distributions for Extreme Events in the Lake Mead Watershed

The 24-hour precipitation distribution (Fig. 2.1B) for the event in Figure 2.5 depicts a south-north swath of rainfall in accordance with the longitudinal circulation dipole seen in Fig. 2.5d. However, as the cutoff low moved from west to east during the 72hrs centered about the extreme event day, the corresponding 72-hour precipitation field appears as a zonal band of heavy precipitation (Fig. 2.2B).

The composited 24-hour precipitation distribution for the 'canonical' and 'TC tapping' RWB events from Figure 2.6 depicts a meridional swath of rainfall spanning southern Arizona to Utah (Fig. 2.3B). Although individual events differ in orientation, location, and precipitation amount, the composited distribution indicates the ability of RWB events to impact the greater NAM region.

Compared to Fig. 2.3B, the composite precipitation values for IV events are noticeably smaller supporting the argument that RWB events are the main drivers of the most extreme precipitation events in the Lake Mead watershed (Fig. 2.4B).

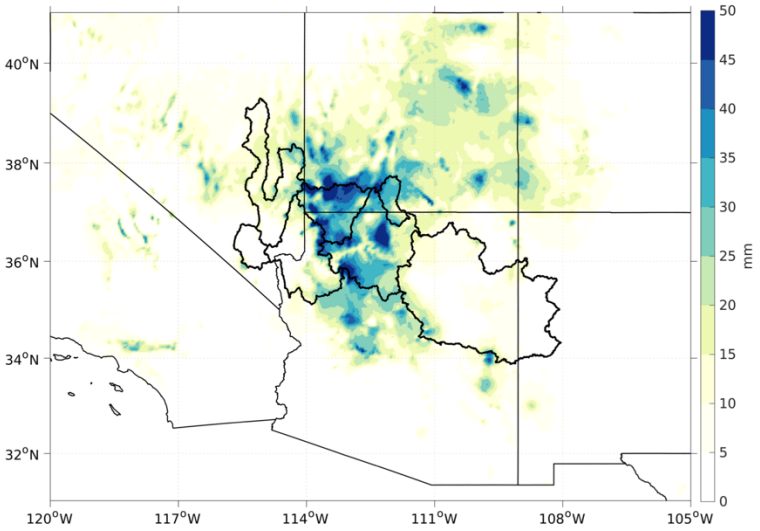

Figure 2.1B. 24-hour PRISM precipitation field for an extreme precipitation event occurring on 23 Sep 2007, shown in Figure 2.5 of the main text.

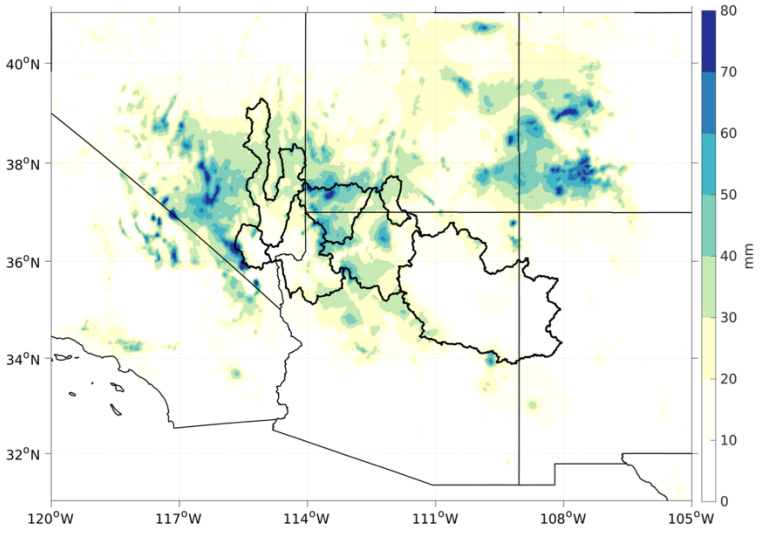

Figure 2.2B. 72-hour PRISM precipitation field for an extreme precipitation event occurring on 23 Sep 2007, shown in Figure 2.5 of the main text. Precipitation data covers 22 Sep 2007, 23 Sep 2007, and 24 Sep 2007.

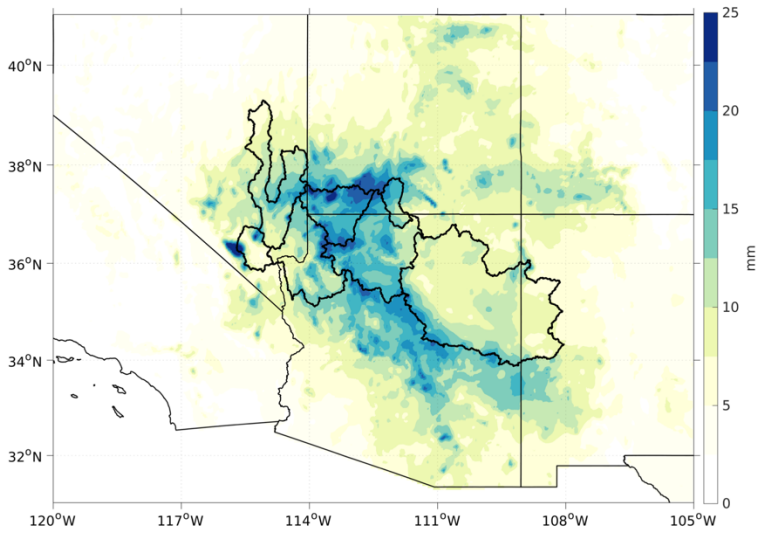

Figure 2.3B. 24-hour PRISM precipitation composite for 'canonical' and 'TC Tapping' RWB extreme precipitation events for the combined Lake Mead watershed (n=16) used to create Figure 2.6 of the main text.

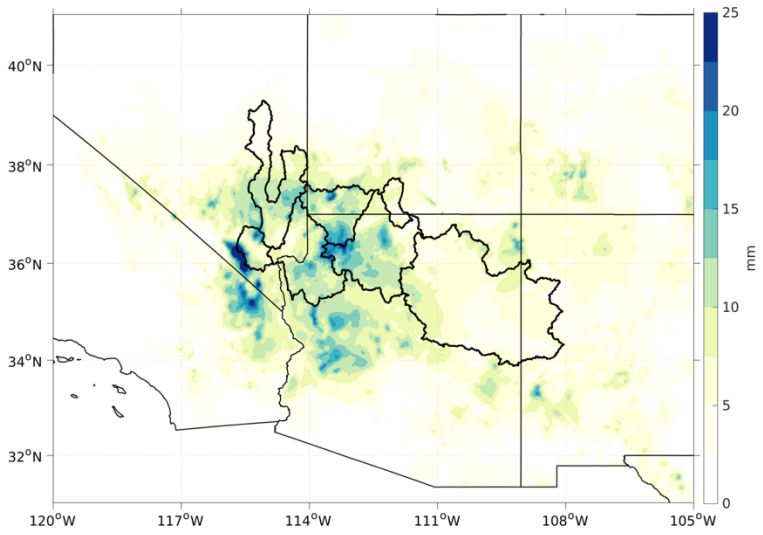

Figure 2.4B. 24-hour PRISM precipitation composite centered around the day of extreme precipitation for IV events for the combined Lake Mead watershed (n=8) used to create Figure 2.7 of the main text.

Chapter 3

Seasonally Anchored Bias Correction of CMIP5 Hydrological Simulations

Abstract

Robust and reliable projections of future streamflow are essential if we are to create more resilient water resources, and such projections must first be bias corrected. Standard bias correction techniques are applied over calendar-based time windows, often 1-month long, and leverage statistical relations between observed and simulated data to adjust a given simulated datapoint. Motivated by a desire to connect the statistical process of bias correction to the underlying dynamics in hydrologic models, we introduce a novel windowing technique for projected streamflow wherein data are windowed based on hydrograph-relative time, rather than Julian day. We refer to this method as 'seasonally anchored'. Four existing bias correction methods, each using both the standard day-of-year and the novel windowing technique, are applied to daily streamflow simulations driven by climates from 10 global climate models across a diverse subset of six watersheds in California to investigate how these methods alter the model climate change signals. Among the methods, only PresRat (short for 'preserves ratio') preserves projected annual streamflow changes, and does so for both windowing techniques. The seasonally anchored window PresRat reduces the ensemble bias by a factor of two compared to quantile mapping (Qmap), cumulative distribution function transform (CDFt), and equidistant quantile matching (EDCDFm) methods. For wet season flows, PresRat with seasonally anchored windowing best preserves the original model change over the entire distribution, particularly at the most extreme quantiles, and the other three methods show improved performance using the novel windowing method as well.

Lastly, when examining temporal shifts in seasonality, PresRat and CDFt preserve the original model signals with both the novel and standard windowing methods.

3.1 Introduction

3.1.1 Climate Change Impacts

Fueled by climate change, rising temperatures and declining snowpacks have revealed that the ways in which the American West has managed water for the past 75 years is insufficient to sustainably meet projected demands (Barnett & Pierce, 2009; Rajagopalan et al., 2009; Udall & Overpeck, 2017). It is equally apparent that river basins, watersheds, and reservoir drainage areas will not be impacted uniformly (Das et al., 2011; Kalra et al., 2008; Mote et al., 2005, 2018). The response of water supply-relevant variables to climate change, such as annual streamflow, total precipitation, or the extent of April 1st snowpack, will be functions of factors like shifting large-scale weather patterns, elevation, topographic aspects, vegetation, and the amplitude of season temperature cycles (Gonzalez et al., 2018; M. He et al., 2019; Huning & AghaKouchak, 2018; Pierce & Cayan, 2013). As a result, the potential impacts of climate change on water management, riparian health, and associated mitigation or adaptation strategies need to be examined on local scales and on a case-by-case basis.

3.1.2 Downscaling and Bias Correction

Future climate projections from global climate models (GCMs) are a key tool for estimating likely impacts of climate change on future water availability, but due to limited spatial resolution (typically no finer than 100 km) are insufficient for studying changes at the local-scale of river basins and heterogeneous hydrologic processes (Fowler et al., 2007; Hewitson et al., 2014; Salathé, 2003). Further, biases in the GCMs, arising from model limitations like subgrid

parameterizations of cloud microphysics and poorly resolved topography at the native GCM grid scale, can result in distorted projected climate impacts (see discussion in Maraun et al., 2017). Prior to being used in most applications, therefore, climate projections must be downscaled and bias corrected. Implemented through either a 'statistical' or 'dynamical' approach, downscaling techniques interpolate smaller-spatial scale features by combining coarser GCM output with higher-resolution observations, topography, and dynamics to produce projections with resolutions on the order of 10s km. Either as part of the downscaling process or done subsequently, bias correction removes systematic errors in the GCM with the goal of retaining the raw GCM climate change signal.

While some climate change planning projects may be satisfied simply by downscaled and bias corrected GCM output (e.g., temperature, precipitation), many require the use of a land-surface model to produce quantities such as streamflow or soil moisture. Even if downscaled and bias corrected GCM output is used to drive the land surface model, streamflow projections often need 'secondary' bias corrections before they are used for planning due to biases introduced within the land-surface model. Though useful, it should be understood that bias correction is a statistical technique and thus is not able to discern between physical processes responsible for a given data-point or a broader climate change-imposed trend (Maraun et al., 2017).

3.1.2.1 Windowing and Bias Correction Goals

Although the goal of the windowing and bias correction process is to remove systematic biases while retaining the signal of change from the driving climate model, many bias correction methods alter the model-predicted change for unphysical reasons (Hagemann et al., 2011; Maraun, 2013; Maurer & Pierce, 2014; Pierce et al., 2013). As a result, the application of different bias correction methods to identical datasets will yield varied future projections (Maurer & Pierce,

2014; Teutschbein & Seibert, 2012). Simplified, many bias correction methods establish a correction function that maps a model variable's empirical distribution over a historical period to that of an observed variable's distribution over a historical period. Upon applying this correction function to the model historical data, the bias corrected data is mapped onto the observed variable's distribution thus removing any systematic biases over the historical period. Though the definition of the transfer function varies among methods (Pierce et al. 2015), nearly all methods make assumptions of stationarity, i.e., that model biases occurring in the model's historical period also apply to future model periods. Though commonly adopted, stationarity is not guaranteed, and it is therefore crucial to understand under what conditions it breaks down (e.g., with changes in large-scale circulation).

Because model biases typically vary by season, correction functions are usually developed for specific calendar-based "seasons" (e.g., Thrasher et al. 2012). Specifically, distributions of the observed, historical- and future- model datasets are developed by subsetting in time, either by individual months or by taking some rolling window of fixed width (see Pierce et al., 2015 for a deeper discussion). Although cumulative distribution functions (CDFs) can be generated either empirically (as in the methods examined here) or parametrically, nonparametric methods have yielded higher skill in reducing systemic errors for precipitation (Gudmundsson et al., 2012).

In the context of climate change, for variables whose seasonal cycles are predominately affected by changing amplitudes rather than shifts in seasonality (such as temperature or even precipitation) it may be fair to assume that historical biases for January data can be removed directly from future January data. Consider, though, a variable whose climate change signal is characterized in large part by a temporal shift in its climatology, such as snowfed streamflow. Historically in the western U.S., mountainous rivers experience peak streamflow during the spring

(later for higher elevation sites) as the snowpack begins to melt (Serreze et al., 1999). Towards the end of the 21st century, reduced in volume and melting earlier, projected snowpack declines result in peak streamflow shifting significantly earlier into the season (Noah Knowles & Cronkite-Ratcliff, 2018; Udall & Overpeck, 2017). If we were to apply a calendar-fixed window to bias correct streamflow (e.g., comparing data from the month of April, historical to future), it is possible that historical bias corrections of peak or rising-limb streamflow data will be applied to future streamflow data occurring well into the receding limb, thus applying corrections to and from different streamflow regimes and controlled by different physical processes.

3.1.3 Purpose of Paper

Motivated by the desire to move towards a 'process-aware' method of statistical bias correction and the inability of fixed calendar- windowing to account for processes that shift seasonality under future climate scenarios, this paper introduces a new 'seasonally anchored' windowing approach that, when applied to existing statistical methods, improves the preservation of original model – used henceforth to refer to hydrologic model output driven by downscaled and bias corrected GCM data – climate change signals in projections of streamflow. We evaluate the performance of several published bias correction methods, using the standard Julian day anchored framework and our seasonally anchored windowing techniques, with respect to their ability to reduce bias while preserving key metrics of climate change from the original model. Specifically, we investigate the preservation of: 1) original model projected changes in water year mean streamflow, 2) original model projected change across all deciles of wet season streamflow, and 3) original model change in seasonality as measured by change in date of peak streamflow.

The paper is structured in the following manner. In Sections 3.2 and 3.3, we describe the study domain and the rivers included in this work, and detail the observed and model data sources

used to evaluate the various bias correction methods. In Section 3.4, we detail the seasonally anchored windowing technique and describe the four bias correction methods compared. Section 3.5 describes the performance of the various methods over both the historical and future climate periods. Lastly, Section 3.6 summarizes and discusses these results.

3.2 Study Domain

The hydroclimate of California is characterized by distinct wet and dry seasons and is punctuated by high interannual variability (Dettinger et al., 2011). In fact, the presence or absence of just a few storms each year can determine the difference between drought conditions and sufficient water supply (Dettinger & Cayan, 2014). Moreover, interannual variability and dependence on just a few storms per year is expected to increase in the future, with model projections showing fewer wet days but more precipitation on the wet days that occur (Pierce et al., 2013). Because 1) there is a strong latitudinal gradient in the frequency of landfalling winter storms (Payne & Magnusdottir, 2014), and 2) interactions between low-level moisture flux and local orographic forcing is driving mechanism of California precipitation (Neiman et al., 2002), the complex terrain of coastal and inland ranges results in marked spatial heterogeneity in the hydroclimate. California's rivers and streams are as diverse as the landscapes that feed them, with flashy, ephemeral streams in low deserts and snow-fed perennial rivers in the high mountains, the latter of which are responsible for filling some of the nation's largest reservoirs. As projected climate change impacts for riparian environments differ dramatically across watersheds and stream types (Perry et al., 2015 and references therein), the diversity of California's waterways and robustness of its observational network make it an excellent testbed for our bias correction methods.

3.3 Data

Bias correction requires both historical (observed or reanalysis) and model data. Thus, the number of rivers eligible for examination are limited to those with both of the above datasets. Streams were selected based on the following criteria: 1) availability of routed streamflow projections from land-surface models driven by downscaled and bias corrected GCM data, 2) availability of at least 20 years of observational data, and 3) their inclusion enhance the representation of selected streams from along the continuum of rain- versus snow- dominated basins. Upon applying the above criteria, we choose 6 rivers for our case study (Figure 3.1, Table 3.1). The selected rivers span hydrologic characteristics of rain-, snow-, and mixed rain-and- snow dominated watersheds, allowing us to test the performance of our seasonally anchored windowing technique for bias correction on streams with and without large projected flow-seasonality changes. We emphasize here that our goal is not to produce an expansive dataset of bias-corrected streamflow, which requires a larger network of streams, though such an exercise will undoubtedly be useful.

Streamflow projections used in this study were obtained from Knowles & Cronkite-Ratcliff, 2018 (see Section 2.2 of Knowles and Cronkite-Ratcliff, 2018 for details). They use Localized Constructed Analogs (LOCA, Pierce et al., 2014) statistically downscaled GCM data to force the Variable Infiltration Capacity (VIC) hydrological model (Liang et al., 1994). Rather than use each of the 31 members in the Coupled Model Intercomparison Project (CMIP5; Taylor et al., 2012) ensemble, we focus our analysis on a subset of 10 GCMs chosen by the California DWR Climate Change Technical Advisory Group as providing passable simulations of the historical California hydroclimate (California Department of Water Resources Climate Change Technical Advisory Group, 2015, models listed in Table 3.2). Here, we restrict our analysis to the future climate relative concentration pathway (RCP) 8.5 since the climate change signal of shifting

seasonality is more easily discerned in higher warming scenarios. However the results found here will apply to other emissions scenarios. Observational data for the six streams span water years (WYs) 1997-2019 and were obtained from the United States Geological Survey (USGS) and California Department of Water Resources (DWR) Data Exchange Center.

3.4 Methodology

While the following subsections describe the methodology in complete detail, we preface by briefly summarizing the algorithmic approach. First, for a given value that is to be bias corrected, we convert from Julian day to a hydrograph-relative time unit. This is done by locating its position (in time) relative to important climatological features (e.g., day of peak streamflow). Then, we map this point in 'hydrograph-relative' time onto all datasets (observed, historical GCM, future GCM) to identify hydrologically similar periods.

3.4.1 Climatological Hydrograph

The first step in the new seasonally-anchored approach is to calculate climatological mean hydrographs for the (1) observed, (2) simulated-historical and (3) simulated-future flows. In the present study, the length of climatological periods varies from the observed (n=23 years, 1997-2019), simulated-historical (n=36 years, 1970-2005), and simulated-future flow series (n=31 years, e.g., 2069-2099). The observed period is limited by the period of available record of gaged streamflow. Climatological-average hydrographs are computed at several quantiles (discussed below), but to ease explanation of the process, we explain it for the 70th percentile (P70) first.

For a given Julian day, the 70th percentile streamflow value is estimated from a distribution containing all data from the climatological period within a 31-day centered window (e.g. at Julian day 185, use data from Julian days 170-200) similar to Thrasher et al., 2012. Once done for all days of the year, this array of length 365 is then smoothed by taking the mean of all points within

the centered 31-day windows. The resulting smoothed array is the climatological hydrograph at the 70th percentile (Figure 3.2, top).

3.4.2 Locating Milestones

Once the climatological hydrograph is calculated for a given percentile, milestones along the curve that correspond to key characteristic features of the stream are identified. Similar to previous work by Yarnell et al. (2015) we define our milestones as the Julian days when four climatological-hydrograph transitions occur (detailed below, and shown in Fig. 3.2): (1) minimum flow, (2) transition from a low-flow period to the rising limb, (3) maximum flow, and (4) transition from the receding limb to a low-flow period.

3.4.2.1 Maximum and Minimum Streamflow

The milestone of peak flow occurs on the Julian day with the largest climatological streamflow and delineates the change from the rising to the falling limbs of the hydrograph (Fig. 3.2, triangle). Similarly, the milestone marking the minimum streamflow occurs on the Julian day with the lowest value of climatological streamflow (Fig. 3.2, circle). This is done for each of the three flow series. Although the vast majority of climatological hydrographs in this study are described by having a single peak, Appendix A describes how the identification of the peak streamflow milestone is handled for 'bimodal' hydrographs.

3.4.2.2 Start of Dry Season

Qualitatively, transitions between distinct streamflow regimes occur when the shape of the hydrograph changes rapidly. We can quantify the shape of the hydrograph by its 1st and 2nd derivatives with respect to time. The first derivative of streamflow ($\frac{dQ}{dt}$, Figure 3.2 middle) indicates where the stream is rising and falling. If we wish to pinpoint the end of the falling limb, we must

only examine days when $\frac{dQ}{dt} < 0$. The second derivative with respect to time ($\frac{d^2Q}{dt^2}$, Figure 3.2 bottom) is used to identify when the hydrograph has maximum points of curvature, or in the language used above, when the shape of the hydrograph indicates an inflection point. To identify the milestone associated with the end of the falling limb (start of the dry season), we find the Julian day coinciding with the local maximum of $\frac{d^2Q}{dt^2}$ given that $\frac{dQ}{dt} < 0$. This is shown schematically in bottom subplot of Figure 3.2 by the 'x'. This is done for the observed and simulated-historical datasets. The process for the simulated-future dataset is describes in the following section.

3.4.2.3 Start of Wet Season

For mixed rain- and snow dominated rivers, there is larger variability in the onset of the wet season than the onset of the dry season (Patterson et al., 2020) as the former is governed by precipitation, which has a high degree of interannual variability (Dettinger et al., 2011), whereas the latter is corresponds to the end of the snowmelt pulse (Stewart et al., 2005), which is driven by lower variability fields such as synoptic temperature advection and solar insolation (Cayan et al., 2001; Mioduszewski et al., 2015; Pederson et al., 2011). Therefore, we don't apply the same method as in the previous section. Rather, we assume the streamflow value associated with the 'start of the dry season' milestone delineates between baseflow and non-baseflow periods. Since the 'start of the wet season' marks the stream's departure from baseflow, the corresponding milestone is set at the Julian day when the climatological hydrograph increases above the streamflow value associated with the 'start of the dry season' milestone. This is shown schematically in top panel of Figure 3.2 by the diamond marker and is calculated for the observed and simulated-historical datasets.

Motivated by the importance of the low-flow period to ecosystem health (Hill et al., 1991; Petts, 1996; Poff et al., 1997; Richter et al., 1996), we deem this 'threshold value' (evaluated as

flow above baseflow) to be characteristic of the stream and assume that the streamflow above baseflow value associated with the low-flow period does not change with time. That is, while baseflow levels may change from historical to future periods, if the historical low-flow period was delineated at 500 cfs above baseflow, then the future climate milestone for the 'start ('end') of the west season' will be located when the stream rises (falls) to 500 cfs above the future climate baseflow. This will yield a consistent comparison of how both the duration of the low-flow period and corresponding streamflow magnitudes change in future climate projections.

3.4.3 Calculating Mean Milestones Across Quantiles

The milestone identification process is performed with hydrographs computed at every 5 percentage points between the 40th and 80th percentiles (P40-80). The final milestone locations for the climatological period are computed by taking the mean value of the milestone dates across all individual quantiles. The rationale for choosing to evaluate data between the 40th and 80th percentiles is two-fold. First, the final milestones should represent a broad range of climatological stream conditions, but extreme values—while only a small fraction of total data--can yield outlier milestones that are not representative of the entire distribution. Because of this, quantiles near the distribution tails are excluded from this final step of the milestone process – though they are accounted for during the windowing procedure described in Section 3.4.4. Second, the asymmetry, relative to the median, of the P40-80 range reflects the differing dynamics of high and low flow climatologies. High quantile flows in the early water year only occur when the synoptic environment is favorable for large precipitation events (typically October at the earliest). As a result, for higher quantile climatological hydrographs, the timing of the start of the wet season is more-or-less constrained to a narrow window of 1-3 months at the beginning of the water year. However, low quantile flows correspond to the absence of large storms and are not constrained in

time. For drier years with few storms during the early WY, the start of the wet season can be pushed far into the water year and, if included, skew the mean value taken over all quantiles in P40-80 (see Fig. 3.2A and 3.3A).

3.4.4 Seasonally Anchored Windowing

Using the milestones as reference points, we are able to bias correct a day's simulated flow in a way that acknowledges its position in the hydrograph, which ensures that the hydrologic processes at work on that day are accommodated. For example, a flow that occurs on the descending limb of the hydrograph will be bias corrected using the same parameters no matter whether that flow is in, e.g., June in the historical period or in, e.g., April in a future projection (Fig. 3.3, bottom). This differs from traditional bias correction techniques that are anchored by day-of-year, which means (in cases where the peak flow shifts earlier in the year) the bias correction parameters from the rising limb of the hydrograph in the historical period might be applied to values from the descending limb of the hydrograph in the future period (Fig. 3.3, top). Because window widths are based on the length of streamflow regime segments (e.g., rising limb), and those segments vary across the observed, historical-, and future GCM climatologies, we do not require the different datasets to have the same window widths. Before the actual bias correction step is done, the empirical distributions of daily streamflow data are cubic hermite spline interpolated to obtain the same length, following Pierce et al., 2015.

3.4.5 Bias Correction Methods to be Compared

To illustrate the effect of the windowing technique on bias corrected streamflow data, we examine the performance of 4 different bias correction methods using first the standard DOY windowing, and then seasonally anchored windowing. Similar to (Pierce et al., 2015), we apply the following techniques: PresRat (Pierce et al., 2015), CDF-transform (CDFt, Michelangeli et al.,

2009), equidistant CDF matching (EDCDFm, Li et al., 2010), and quantile mapping (Qmap, Panofsky & Brier, 1968; Wood et al., 2002). For the sake of brevity, we do not discuss the details of each bias correction method and instead refer the reader to Section 3 of Pierce et al., 2015.

For the CDFt, EDCDFm, and Qmap methods, we adopt the standard practice of bias correcting data using a 30-day window centered around a given datapoint. The 30-day window enables the methods to represent the seasonal cycle, but such a narrow window is not suitable to correct extreme events. Because extreme values of precipitation can occur at any time during the wet season, the PresRat method from Pierce et al., 2015 does not use a fixed 30-day window like the other 3 methods and instead iteratively bias corrects data using windows of increasing width, providing better correction of extreme values. Rather than applying iterative bias correction in the version of PresRat used in this study, we develop an alternative method to balance the correction of extreme values (requiring a wide window) and the seasonal cycle (requiring a narrow window). Here, we vary the window width based on the 'extremity' of a value. Beginning with a 30-day window, we find the quantile location of the data point being corrected in its climatological distribution. If it falls between the 20^{th} and 80^{th} percentile, a 30-day window is used. Otherwise the window is expanded by 15-days on either side and the quantile location of the data is found again. If the data falls between the 10^{th} and 90^{th} percentile, the 60-day window is applied. If not, a 120-day window is used to bias correct the most extreme values. This reflects the fact that extreme events are by nature rare.

Because some methods of bias correction operate on fractional changes between a future and historical model period, they can be sensitive to small errors occurring at low values (Pierce et al., 2015). For this reason, prior to bias correction, we correct for any biases in the model baseflow by adding the difference between the observed and simulated baseflow values to all

model data. This greatly improves the efficacy of the bias correction methods at lower flows while having very little impact at higher flows.

3.5 Results and Discussion

The efficacy of a bias correction method can be evaluated by its ability to remove systematic model biases while preserving desired climate change signals from the original model. In this case we choose to consider: 1) mean changes in streamflow magnitude over the entire water year, 2) changes in magnitude evaluated at high, medium, and low quantiles of the distribution, and 3) temporal shifts of seasonality (which may be small in some streams). The combination of bias correction method (QM, CDFt, EDCDFm, PresRat) and windowing technique (standard day-of-year or seasonally anchored) is evaluated by its ability to preserve the 3 quantities listed above. As the magnitude of streamflow varies substantially between California watersheds, working with normalized data allows for a more straightforward comparison of climate change signals. For this reason, we normalize any change between a simulation's future and historical values by a historical baseline (Equation 3.1) to give a percent change relative to the pre-climate change period.

$$\Delta = \mathbf{100} * \frac{\boldsymbol{Future - Historical}}{\boldsymbol{Historical}} \tag{3.1}$$

Using a standardized metric (Δ) helps us compare both the magnitude of change across a diverse subset of streams and the performance of bias correction methods in preserving this metric. In the following sections, we evaluate change between the future (also referred to as 'end-of-century') and historical periods defined as water years 2069-2099 and 1970-2005 respectively. Subsequent sections evaluate this change over both the entire water year and over the 'wet season', which we define as the timeframe spanning 1-month prior to the start of the wet milestone to 1-

month after the end of the wet season milestone. This covers the period roughly from November to June (although it is subject to both watershed elevation and climatological era).

3.5.1 Validation Over the Historical Period

Applied over the historical period, the PresRat, CDFt, and EDCDFm methods simplify to the quantile mapping method, with the exception of data off the endpoints of the historical distribution (see Section 3 of Pierce et al., 2015 for discussion). Therefore, when using a relatively narrow 30-day window, all methods are effective in correcting the historical GCM data so that it recreates the observed data's seasonal cycle. This is true for both the standard day-of-year windowing technique and the seasonally anchored windowing technique (not shown). Concerning the historical period, the only meaningful difference between the four bias correction methods results from the variable window width used in our PresRat method (Figure 3.4). Because the window width expands when correcting high-quantile data, large streamflow events occurring early in the wet season can be mapped onto observed streamflow values occurring up to 60 days later (as opposed to 15 days later in the standard method). This can result in slightly elevated mean flows during the transition from dry-to-wet season, driven by streamflow at high quantiles. However, as extreme precipitation and streamflow events can occur at any point between October-April, a variable window based on the quantile of the datum being corrected is more easily justifiable than the common fixed narrow (31-day) window when correcting hydrometeorological variables in the western US.

3.5.2 Water Year Mean Streamflow

Before evaluating the ability of each bias correction method to preserve the projected future change in mean water year streamflow, we first examine the original model signal (Figure 3.5). Across the simulations of 6 streams that were driven by projections from 10 GCMs, the changes

in water year mean streamflow differ considerably. Evaluating change in units of percent of historical mean, which removes the influence of differing streamflow magnitudes, we see that CESM1-BGC, CNRM-CM5, and CanESM2 have the largest projected increases in water year mean streamflow with values upwards of 40% for some streams. Although the largest percent increases occur for the streams with the lowest flows, these models suggest higher-flow streams will still see increases beyond 30%. Among the projections based on the 10 GCMs, there is little agreement on the sign or magnitude of the projected change and the projections with very large increases heavily influence the multi-model ensemble mean change.

We use the term 'error' here to refer to the difference between original model projected change and post-bias correction projected change. This quantity is an error in the sense that we expect our bias correction approach to preserve certain key aspects of the model-predicted climate change signal (as listed explicitly above), and is defined in Equation 3.2 below,

$$Error = \Delta_{Bias\ Corrected} - \Delta_{Raw\ GCM} \tag{3.2}$$

wherein Δ is defined by Equation 3.1. Using the above definition, we now compare the ability of the 4 bias correction methods and 2 windowing techniques in preserving the signal of water year mean change averaged across the 10 GCMs and 6 streams.

The CDFt, EDCDFm, and Qmap bias correction techniques do not intrinsically preserve the water year mean flow change signal from the un-bias corrected projections (Table 3.3). The PresRat method is the one method that preserves the water year mean flow change, for both windowing methods, with mean and root-mean-square (RMS) errors <1%, and does so by design (see Pierce et al., 2015). The other three methods alter the original model signal to varying degrees. In all cases, applying a seasonally anchored window improves the preservation of the water year mean flow change signal by nearly a factor of 2 compared to the standard day-of-year windowing

technique. In addition to improving the mean flow change, the new windowing technique also results in a narrower spread of errors among the models in the PresRat, CDFt, and Qmap methods.

3.5.3 Wet Season Streamflow by Decile

The hydroclimate of the western US is dominated by the occurrence (and absence of) extreme precipitation and streamflow events. Therefore, statistical bias correction techniques need to preserve the original-model projected changes at high-flow quantiles, rather than altering the projected change for no physical reason. When viewed at the granularity of a single percentile of flow, the signal of projected changes can be noisy. Therefore, we evaluate here changes at decile levels over the wet season. Again, before evaluating the ability of each bias correction method to preserve this quantity, we first examine the un-bias corrected model signals. Change is calculated with Equation 3.1 using the mean of all streamflow values within a given decile range for each of the historical and future climate periods. Figure 3.6 gives a visual depiction of the original model climate change signal at the Shasta gage and the remaining 5 streams can be seen in Appendix B. Although some minor differences exist among the 6 streams and 10 GCM-based histories, there is a near unanimous agreement that the top 10-20% of streamflow values will increase while the middle ~30% of the distribution will decrease. This follows the projected climate change signal in precipitation wherein high-tail events occur with greater frequency (Gershunov et al., 2019). Notably, in the historically most snow dominated watershed, Millerton, larger differences exist between the 10-member ensemble, with 4 models projecting large increases at the high end and 2 projecting decreases. Again, this work does not focus on the impacts or certainty of projected streamflow changes, but rather on the extent to which they are altered by bias correction techniques.

Using Equation 3.2, we evaluate how well each correction method and windowing technique preserves the original projected change at each decile over the wet season. Figure 3.7 provides a visual representation of these errors for the PresRat method using seasonally anchored windowing. Equivalent plots for the remaining combination of bias correction and windowing methods can be found in Appendix C. Each subplot contains a box-and-whisker plot for a given stream wherein errors for individual GCM projections are shown by grey circles and the mean error across the 10-member ensemble is depicted by an orange line. In Figure 3.7, with few exceptions, errors in the depiction of future changes in wet season streamflow, by quantile, falls within ± 10% of the original model signal for all the combinations of GCMs and streams. As mentioned earlier, a large fraction of the total streamflow is contained in the top 10-20% of the distribution. To highlight where, in terms of decile, large errors in the bias correction method begets large errors in streamflow, the fraction of total wet season streamflow represented by each decile is plotted on the right y-axis. Though not explicitly shown here, the PresRat method with seasonally anchored windowing has notably smaller biases than other techniques at the top decile of flows.

To quantitatively assess how well the original signal is preserved, we calculate the root-mean-square error (RMSE) at each decile for each of the 4 correction methods and 2 windowing techniques, using the following equation,

$$RMSE = \sqrt{\frac{\sum_{i=1}^{N}(\Delta_{Bias\ Corrected_i} - \Delta_{Raw\ GCM_i})^2}{N}} \tag{3.3}$$

where i represents a given driving-GCM. Then, motivated by the importance of large streamflow events to the hydroclimate of the western US, we weight the RMSE at each decile by the percentage of total historical wet season streamflow in the decile, thus emphasizing errors at higher deciles. We refer to this quantity as the flow-weighted RMSE. To equally weight the performance

of the bias correction technique on each river, and thus equally sampling the range of snow vs. rain dominated regimes, the flow weighted RMSE at each decile is averaged across the 6 streams.

Figure 3.8 and Table 3.4 summarize the above process and depicts the flow weighted RMSE averaged across the 6 streams for all combinations of correction method and windowing technique. At lower deciles, the flow weighted RMSE values are similar across the 4 correction methods. The lines begin to diverge near the 50th percentile with the seasonally anchored PresRat and CDFt methods achieving the best performance between the 50th-90th percentiles. For the top 10% of streamflow, where the most impactful of streamflow events exist, PresRat with seasonally anchored windowing best preserves the original model signal of change. If we take the average across all deciles for each line individually, we see that the PresRat method using seasonally anchored windowing not only yields the lowest flow weighted RMSE, but that for each correction method, the seasonally anchored windowing method outperforms the standard day-of-year method (triangle markers).

3.5.4 Temporal Shift in Peak Streamflow

The previous sections focus on the ability of bias correction techniques to preserve original model projected changes in the magnitude of annual and wet season flow. Because the fingerprint of climate change for mountain rivers is characterized by changes in both magnitude and timing of peak streamflow, we will now evaluate the ability of each correction method and windowing technique to preserve projected shifts in seasonality. Using the climatological milestone associated with the peak streamflow (defined in Section 3.4), we compare the original model change (measured in days) in peak streamflow timing with the bias corrected changes.

Evaluating the difference in Julian day of peak streamflow between the end-of-century and historical periods, Figure 3.9 shows the original model change in days on the x-axis and the change

from the PresRat with seasonally anchored windowing method on the y-axis for each of the 10 GCM-projected climates and 6 rivers. If the bias correction methods preserve the original model signal exactly, all markers would fall on the dotted black 1-to-1 line. For the overwhelming majority of stream and GCM combinations, we see that the temporal shift is well-preserved. Though the amount of change varies with GCM, it is most strongly related to the how snow-dominated a watershed is over the historical period. The largest signal of change is seen at New Melones (red markers), which loses its historical snowmelt peak entirely. The snowiest basin, Millerton (green markers), doesn't exhibit as large a signal because unlike New Melones, it retains a snowmelt peak in some projections.

Table 3.5 summarizes the preservation of the projected temporal shifts for the various bias correction methods and windowing techniques. For the PresRat and CDFt methods, which best preserve changes in streamflow magnitude, the seasonally anchored windowing method yields similar error metrics as the standard day-of-year technique. By virtue of locking windows to Julian days, the day-of-year method does a good job at preserving the raw model signal of temporal change. Notably, the seasonally anchored method achieves the same efficacy (for PresRat and CDFt) as the day-of-year method without requiring identical windows for the historical and future datasets.

3.6 Summary and Conclusion

Robust and reliable projections of changes in future streamflow are essential if we are to improve (or maintain) resilient water resources and mitigate damage to riparian ecosystems in the face of climate change. But raw simulations of streamflow are used in applications or impact models only at one's peril, unless first bias corrected. Traditional methods for bias correction operate by comparing future and historical model data from shared ranges of Julian days. However,

the physical and environmental process that govern streamflow (or any hydrometeorological variable) are not necessarily fixed to calendar periods, especially in the context of climate change, which will advance melting season earlier in the year and can alter the seasonality of precipitation. In order to better connect the statistical process of bias correction to the underlying processes in hydrologic models, we introduce a novel windowing technique for bias correction of projected streamflows. Data are windowed based on hydrograph-relative time, not calendar day. By locating the temporal position of a given data point undergoing correction in relation to characteristic features of its average hydrograph (e.g., start of rising limb, peak flow, end of falling limb, minimum flow) we window data based on hydrographically-equivalent days across the observed, simulated-historical, and simulated-future periods.

We evaluate the efficacy of several bias correction methods, using both the standard day-of-year and our new seasonally anchored windowing technique, applied to streamflow projections for six California streams that range from rain- to snow dominated watersheds and that are responses to climate projections from a suite of 10 CMIP5 global climate models (GCMs) selected by the California Department of Water Resources as having good representation of the historical California hydroclimate. Based on the importance of individual high-magnitude streamflow events, total water year streamflow, and timing of peak flow on the natural and built environment, we argue that successful bias correction should accomplish three tasks: 1) preserve the water year mean climate change signal of the un-bias corrected flow projections, 2) preserve un-bias corrected changes at all quantiles, and 3) preserve any temporal signal of shifting seasonality in the un-bias corrected flow projections, all while correcting the simulated historical statistics to that of the observed dataset. Evaluated as the percent difference relative to the historical period, we

investigate the degree to which the four bias methods and two windowing techniques preserve the un-bias corrected signal of climate change across the study domain.

PresRat is the only bias correction method examined in this work that preserves the original model, shorthand for hydrologic model output driven by downscaled and bias corrected GCM data, signal of water year mean change and does so for both seasonally anchored and standard day-of-year windowing techniques. Although the other 3 methods, CDF transform (CDFt; Michelangeli et al., 2009), Equidistant CDF matching (EDCDFm; Li et al., 2010), and Quantile Mapping (Qmap; Panofsky & Brier, 1968; Wood et al., 2002) do not preserve the original model water year mean changes, even for these methods, seasonally anchored windowing reduces the ensemble mean error by roughly a factor of two while reducing the spread when compared to standard day-of-year windowing.

For an extreme and highly variable hydroclimate, like California, where a large fraction of total water (both streamflow and precipitation) is contained in the top decile of the distribution, it is vital that bias correction does not skew the original model projection signals of change at the highest quantiles. Using the root-mean-square error evaluated at each decile of wet season streamflow to gauge success, we find that 1) PresRat with seasonally anchored windowing best preserves the raw signal at the top decile of flows, 2) PresRat with seasonally anchored windowing best preserves the raw signal averaged over all deciles, and 3) using seasonally anchored windowing improved the performance of each of the four bias correction methods. These findings are true not only for the 10-member ensemble averaged over the six streams, but true for all streams individually. With respect to streamflow magnitude, regardless of their hydrological characteristics (e.g., rain- vs. snow dominated), the seasonally anchored windowing technique was more effective in preserving the original model signals of climate change.

Finally, because any shift in seasonality of snow-fed rivers will have strong impacts on both the natural and built environments, we examine the extent to which bias correction methods alter the original model signals of shifting seasons. We measure the change in seasonality by finding the difference between the Julian dates coinciding with peak streamflow in the simulated-future and simulated-historical periods. While the seasonally anchored windowing technique improved the preservation of original model signals in magnitude, we find that both windowing methods preserve the shift in seasonality equally well (for PresRat and CDFt) with mean bias values < 1 day and root-mean-square error of ~7 days.

In summary, seasonally anchored windowing, as opposed to the standard day-of-year technique, yields better bias corrected projections of future streamflow across a subset of six streams ranging from rain- to snow- dominated ecosystems in California. Without sacrificing any capacity to preserve projected changes in timing of peak streamflow, the seasonally anchored method improves the preservation of magnitude changes in the un-bias corrected flow projections. This is true not only for the water year mean signal, which is important as it relates to the total volume of water flowing through the river over the course of the year, but is also true for both low and high streamflow events which have an outsized imprint on California's hydroclimate, water resources, and ecosystems.

While this work focused largely on wet season streamflow, Figure 3.10 highlights an important vulnerability of the standard day-of-year windowing concerning late season flows. Since biases from the early receding limb of the historical period hydrograph are applied to near-baseflow streamflow during the end-of-century period (because both occur over the same calendar-based period), the resulting bias corrected projections can represent something very unphysical: streamflow decreases past baseflow during the receding limb before rebounding and then receding

once more until it reaches baseflow (dashed lines). In contrast, the future period hydrographs for seasonally anchored methods (solid lines) do not exhibit this unphysical behavior because they apply biases from equivalent stretches of the climatologies. Because this seasonal shift is driven by warming temperatures resulting in diminished snowpack whose peak volume is pushed earlier into the water year, this non-physical feature is most prevalent for historically snow-dominated watersheds.

This work 1) demonstrates the inability of bias correction with day-of-year windowing to provide reliable projections of variables whose climate change signal is characterized by changes in both magnitude and seasonality, and 2) introduces a novel windowing method which moves towards 'process informed' bias correction wherein environmental and physical processes, rather than calendar dates, are shared by windowed data. Given the importance of streamflow projections in creating more resilient water resources, it may be pertinent to evaluate the difference in future streamflow projections across a wider range of California rivers using both seasonally anchored and day-of-year windowing methods. Although we conceptualized and applied the method for the purpose of bias correcting streamflow in California, the fundamental technique of windowing based on the position (in time) of a given data point in reference to some climatological milestones could be applied to variables other than streamflow (e.g., snow water equivalent, which is also expected to have a significant seasonal shift in the future). For variables that will have seasonal shifts in the future, it is important to move towards 'process informed' bias correction and away from calendar-based methods that are completely detached from the physical processes governing the systems. Although the method introduced here does not directly tether the statistical process of bias correction to the underlying physics of GCMs or land surface models, it is a step in the appropriate direction.

3.7 Acknowledgments

All authors were supported by the CA Department of Water Resources grant number 4600013361. MDS received support from the US Army Corps of Engineers, grant number USACE W912HZ-19-SOI-002. DWP received support from the California Energy Commission grants EPC-16-063, PIR-19-007, and EPC-20-006 and NOAA's RISA California-Nevada Climate Applications Program Award NA17OAR4310284.

Chapter 3, in full, is the material submitted to the Journal of Hydrometeorology. Sierks, M., Pierce, D. W., Chapman, W. E., Ralph, F. M. (2022) Seasonally Anchored Bias Correction of CMIP5 Hydrological Simulations. The dissertation author was the primary investigator and author of this paper.

Table 3.1. Name, gage identification and summary characteristics of each watershed. Streams are listed by their fraction of total water year streamflow occurring before April 1 (proxy used to indicate importance of snowmelt) in descending order with the snowiest watersheds listed in the final rows.

Stream	Gage ID	Drainage Area (km2)	Min, Max Elevation (m)	Mean Elevation (m)	% Streamflow Before April 1 (Observed)
Napa River	USGS, 1145800	550	7, 1161	247	87.7
Elder Creek	USGS, 11379500	250	255, 1959	978	73.2
Shasta Dam	CDEC, SHA	18350	306, 4113	1435	62.0
Oroville Dam	CDEC, ORO	9350	240, 2635	1545	58.0
New Melones Reservoir	CDEC, NML	2550	160, 3381	1632	43.6
Friant Dam (Millerton)	CDEC, MIL	4250	157, 3954	2161	30.6

Table. 3.2. Selection of 10 GCMs from CMIP5 used in this work along with their originating institutions.

Model Acronym	Model Source/Institution
ACCESS1.0	Commonwealth Scientific and Industrial Research Organisation (CSIRO) and Bureau of Meteorology, Australia
CCSM4	National Center for Atmospheric Research (NCAR), United States NCAR, United States
CESM1-BGC	National Center for Atmospheric Research (NCAR), United States NCAR, United States
CMCC-CMS	Centro Euro-Mediterraneo per I Cambiamenti Climatici
CNRM-CM5	Centre National de Recherches Météorologiques, France
CanESM2	Canadian Centre for Climate Modelling and Analysis, Canada
GFDL-CM3	Geophysical Fluid Dynamics Laboratory (GFDL), Princeton, New Jersey, United States
HadGEM2-CC	Met Office Hadley Center, UK
HadGEM2-ES	Met Office Hadley Center, UK
MIROC5	Atmosphere and Ocean Research Institute and NIES, Japan

Table 3.3. Summary statistics for each bias correction method (rows) and windowing technique (Standard day-of-year show in parentheses, seasonally anchored shown without) on their success in preserving the projected mean change in water year mean streamflow across the 6 streams and 10 GCMs.

BC Method	Ens. Mean Error [%]	RMS Error [%]
PresRat	0.20 (0.37)	0.86 (0.91)
CDFt	1.72 (6.18)	5.57 (8.64)
EDCDFm	4.49 (7.69)	13.04 (12.96)
Qmap	3.33 (6.14)	7.64 (10.59)

Table 3.4. Flow weighted root-mean-square error (RMSE) averaged over all deciles and across all streams. Methods using standard day-of-year windowing are shown in parentheses, and those using seasonally anchored are shown without parentheses.

BC Method	Ensemble Mean RMSE Across Deciles [Flow Weighted %]
PresRat	0.51 (0.81)
CDFt	0.75 (1.37)
EDCDFm	1.81 (3.47)
Qmap	1.21 (1.93)

Table 3.5. Summary of the ability of each bias correction method and windowing technique to preserve the original model signal in the temporal shift in climatological peak streamflow. Methods using standard day-of-year windowing are shown in parentheses, and those using seasonally anchored are shown without parentheses.

BC Method	R2	Ens. Mean Error [days]	RMSE [days]
PresRat	0.9 (0.9)	0.4 (0.1)	6.8 (6.9)
CDFt	0.9 (0.9)	0.1 (0.1)	7.1 (7.0)
EDCDFm	0.6 (0.9)	3.1 (-0.5)	15.3 (6.7)
Qmap	0.8 (0.9)	0.1 (0.4)	11.1 (7.6)

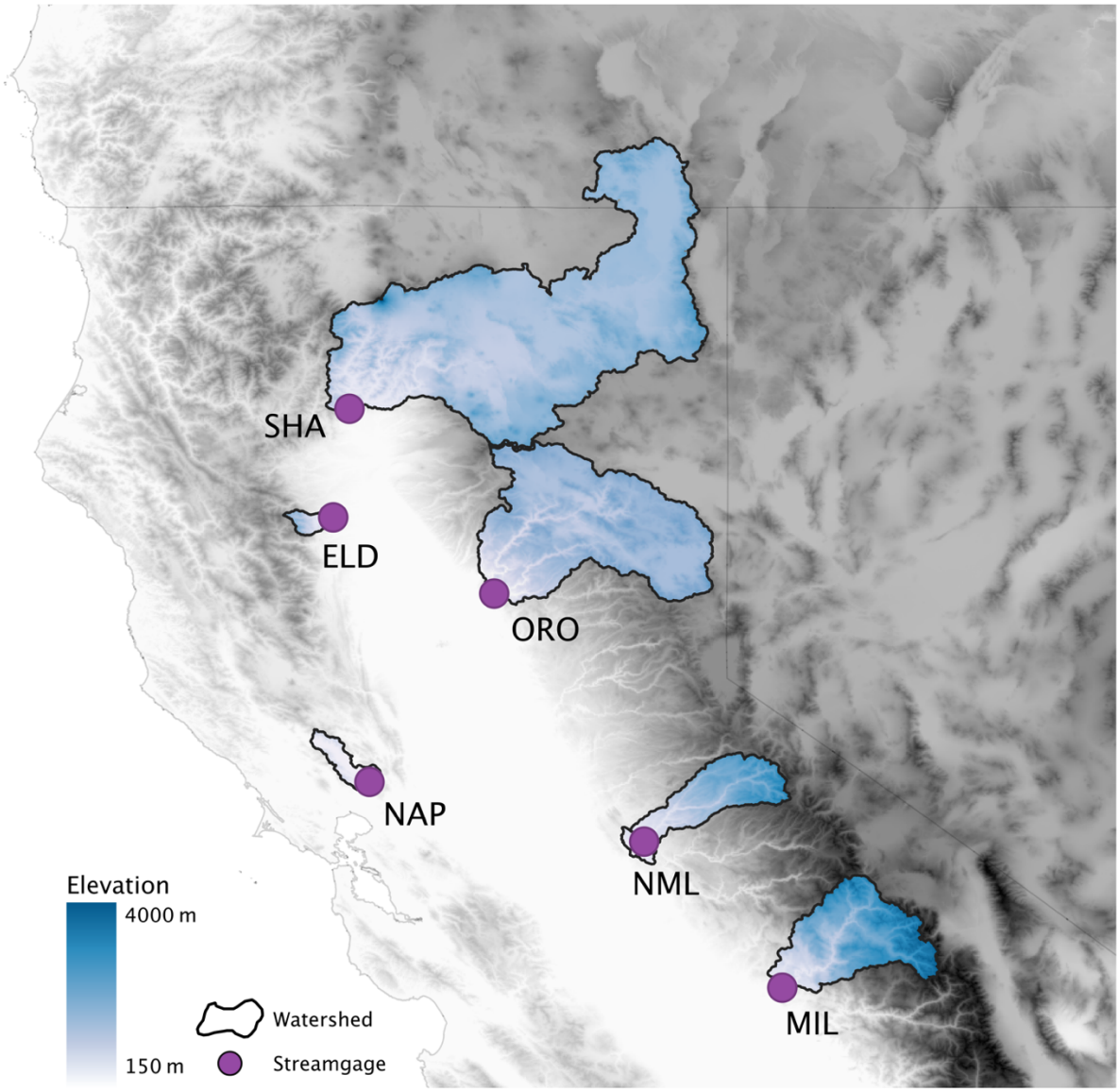

Figure 3.1. Map of the study domain with watershed boundaries (black contour), gage locations (purple circle), and three-letter abbreviations for the 6 streams alongside elevation (color shade). Characteristics of each watershed are listed in the accompanying table (Table 3.1).

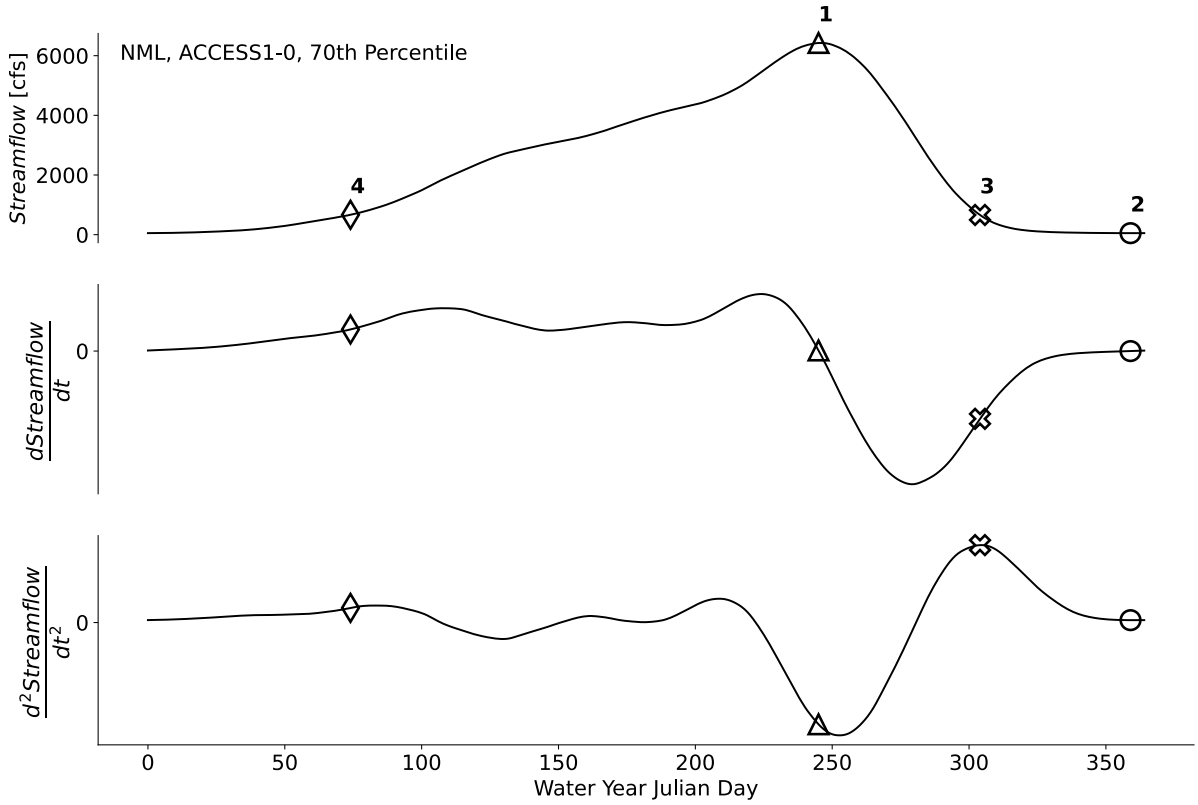

Figure 3.2. Visual depiction of the algorithm used to identify climatological milestones for the seasonally anchored windowing method. Climatological data from the New Melones stream and ACCESS1.0 GCM is shown at the 70th percentile to illustrate the method. Daily mean climatological streamflow (top), and the first and second derivatives of streamflow with respect to time (middle and bottom respectively) are plotted on against water year Julian day. Numerical annotation is used to indicate the workflow by which the four seasonal milestones are assigned: (1) Peak streamflow (triangle), (2) Minimum streamflow (circle), (3) Start of the dry season/end of receding limb (x), and (4) Start of the wet season/beginning of the rising limb (diamond).

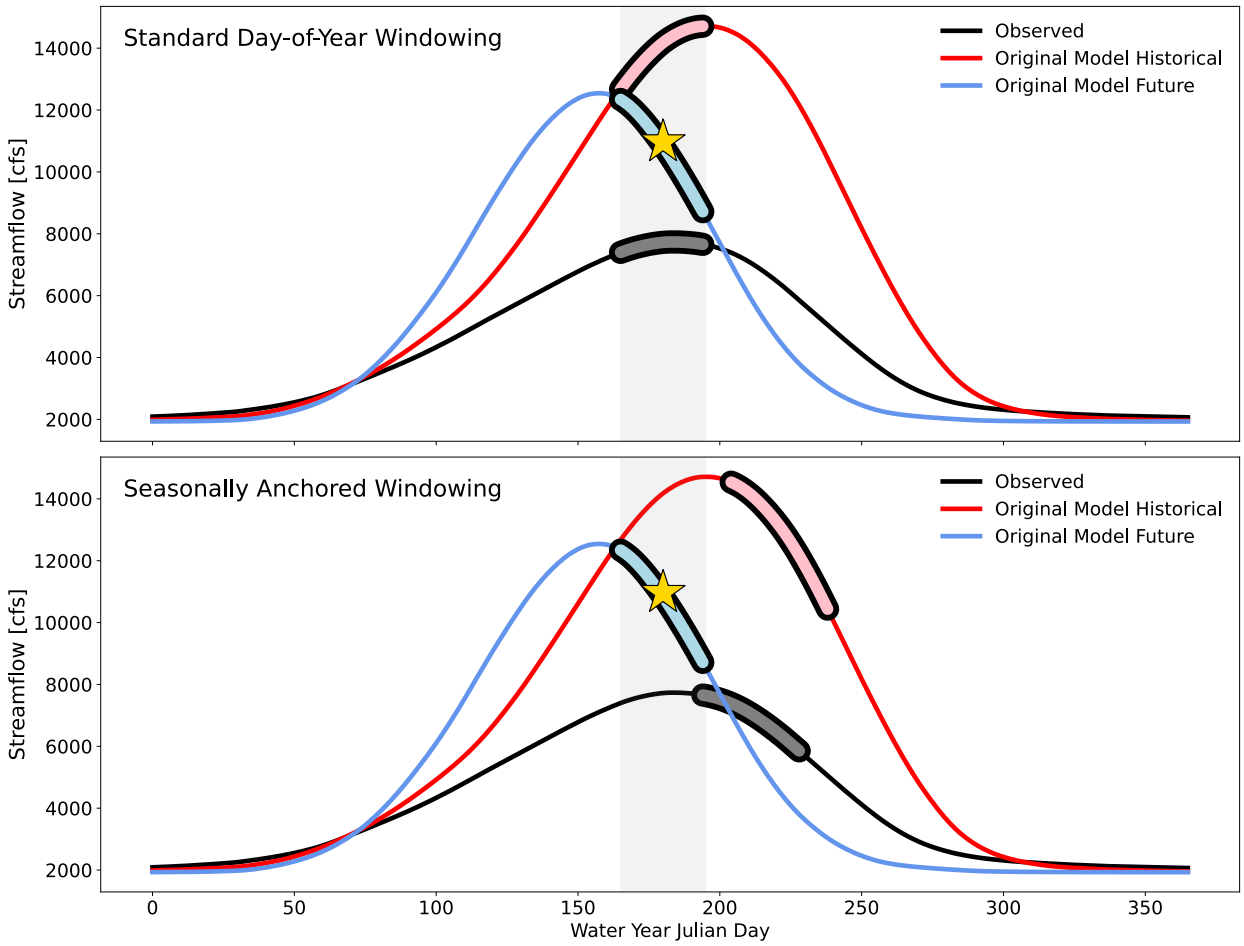

Figure 3.3. Schematic highlighting the effect of windowing technique on which segments of the climatological hydrograph are used to bias correct a given model datapoint on the 180th day of the water year (yellow star). Each panel shows the climatological hydrographs in thin lines for the observed (black), historical original model (red), and end-of-century original model (blue) data. The segments of each hydrograph used in bias correction are plotted as bolded lines. Standard day-of-year windowing (top) uses data from each curve that falls within the centered 30-day period (grey shaded region). Seasonally anchored windowing (bottom) uses a centered 30-day window over the climatological period being corrected and then finds equivalent segments of the observed and historical hydrographs to use for bias correction.

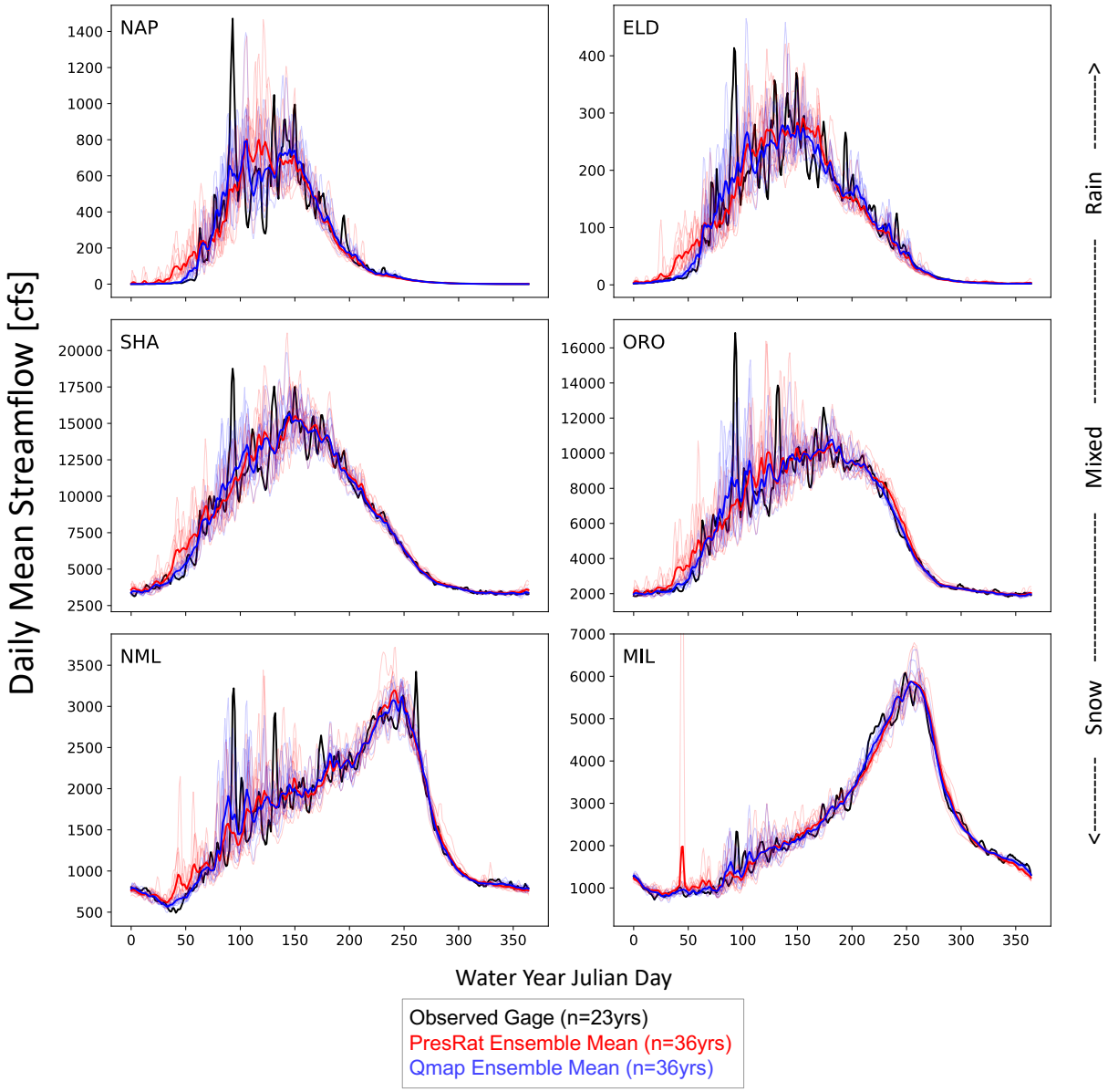

Figure 3.4. Daily mean streamflow for the observed (black), and bias corrected data over the historical period for PresRat with seasonally anchored windowing (red) and quantile mapping with day-of-year windowing (blue) for each of the 6 rivers. For the GCM data, the ensemble mean across the 10-GCMs is shown in a bolded line with individual members depicted by thin lines. Subplots are arranged such that from top-to-bottom, streams transition from rain- to snow dominated watersheds.

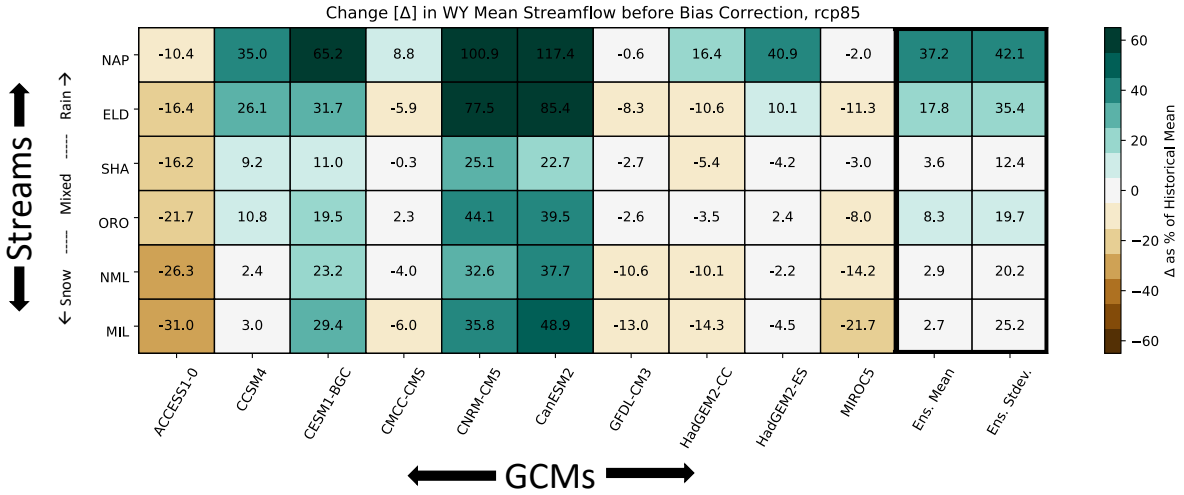

Figure 3.5. Original model projected change in water year mean streamflow across the 6 streams (rows) and 10 GCMs (columns) with the 10-member ensemble mean and standard deviation (farthest right columns). Using units of 'percent change from the historical mean', increasing streamflow is indicated by green color-shading, and decreasing streamflow by brown. Values under 5% change appear as white.

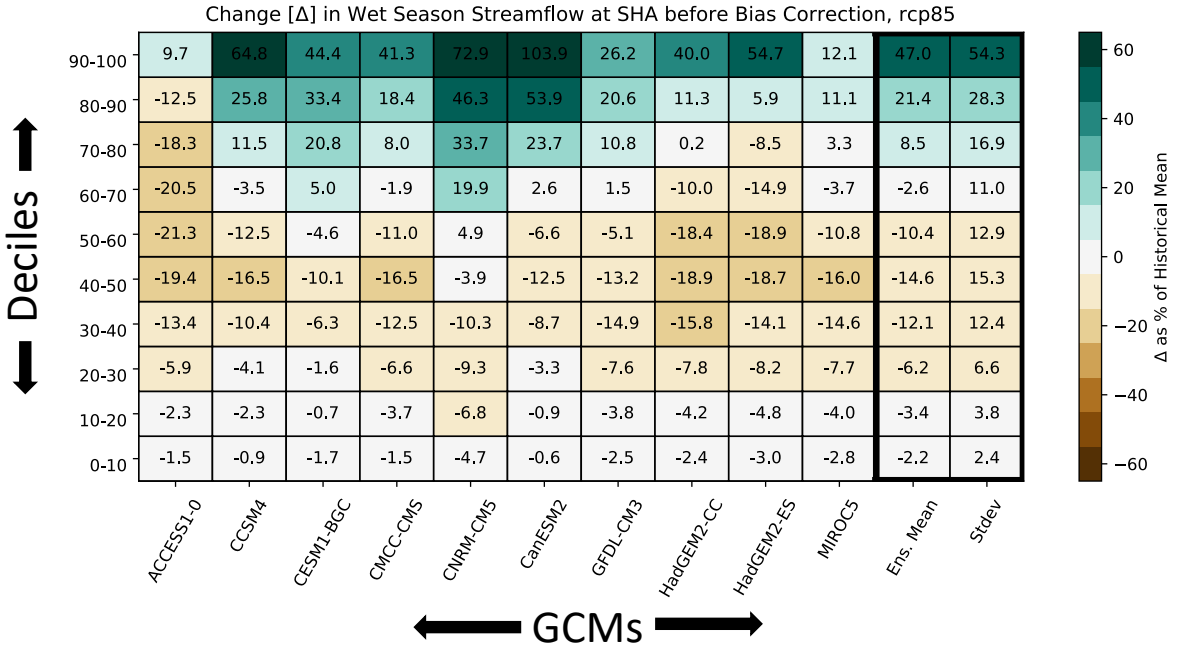

Figure 3.6. Original model projected change in Shasta streamflow by decile (rows) and GCM (columns) with the 10-member ensemble mean and standard deviation (farthest right columns). Using units of 'percent change from the historical mean', increasing streamflow is indicated by green color-shading, and decreasing streamflow by brown. Values under 5% change appear as white.

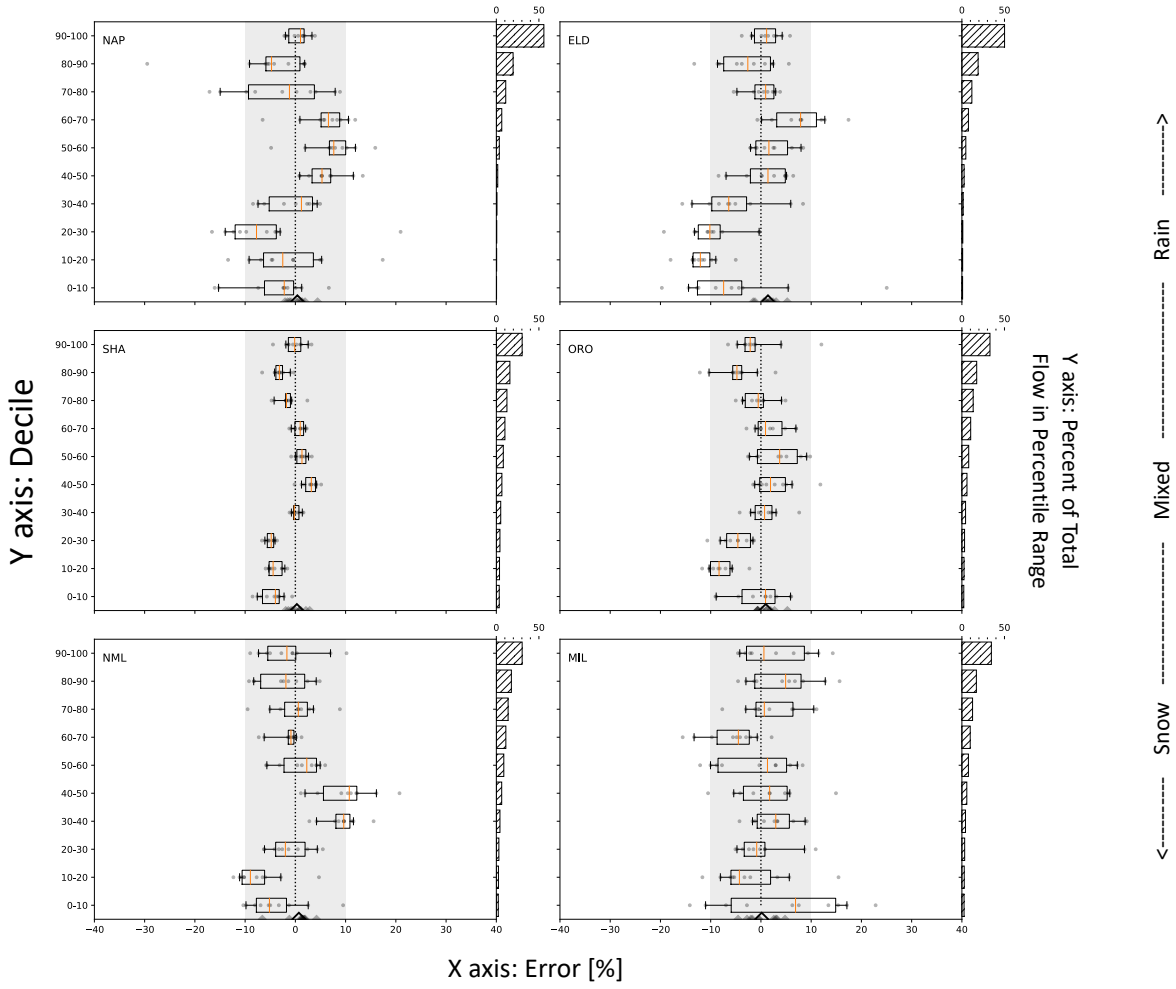

Figure 3.7. Error by decile for change in wet season streamflow for PresRat with seasonally anchored windowing. Errors (x-axis) for individual GCMs are depicted by grey circles, the mean error across the 10-member ensemble is depicted by an orange line. The box edges and whiskers represent the middle 5 and 8 GCMs respectively. The error for a single GCM averaged over all deciles is depicted as a small grey triangle on the x-axis and the value for the 10-member ensemble mean is denoted by a large triangle. For reference, the grey shading and dashed black line correspond to ± 10% error and 0% error respectively. For each stream, the right y-axis depicts the historical percentage of total wet season streamflow contained in each decile averaged across the 10-member ensemble. Subplots are organized so that as you move down the rows, streams transition from rain- to snow dominated over the historical period.

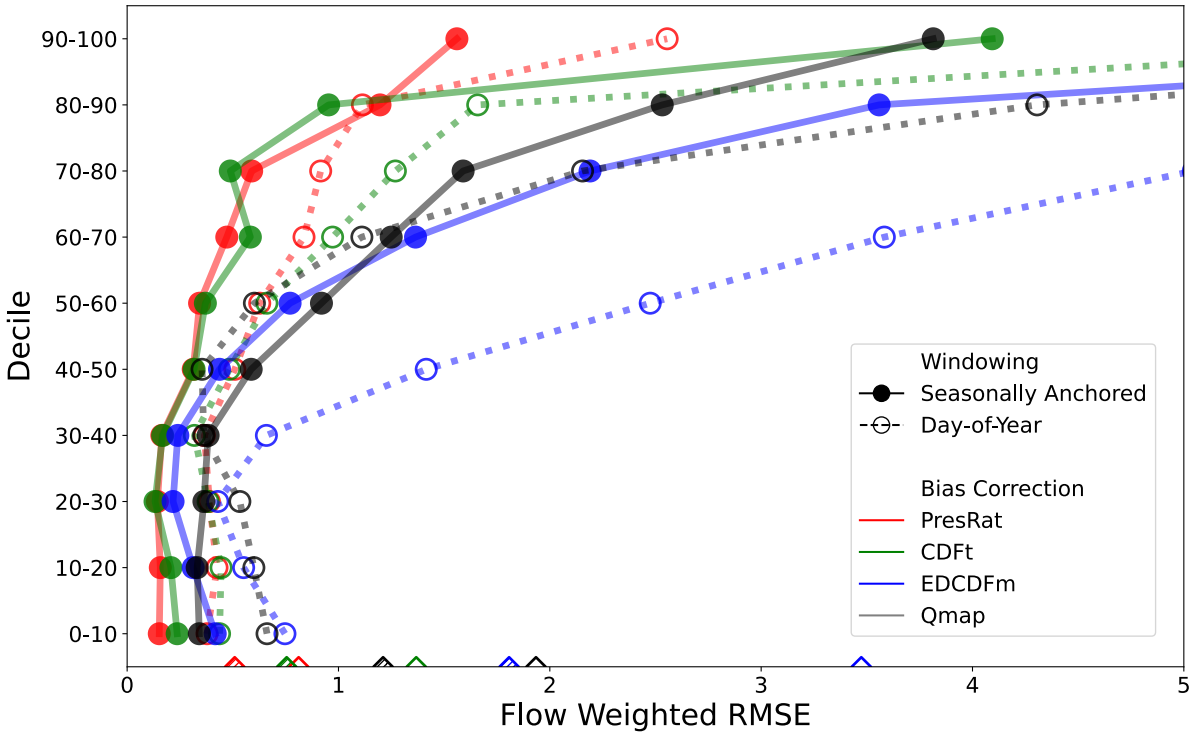

Figure 3.8. Flow weighted root-mean-square error (RMSE) in the representation of model-predicted future change in mean flow at each decile averaged across the 6 streams. Solid (dotted) lines represent correction methods using seasonally anchored (standard day-of-year) windowing techniques. For solid (dotted) lines, the value of the flow weighted RMSE averaged across all deciles is indicated by a hatched (unfilled) triangle on the lower x-axis.

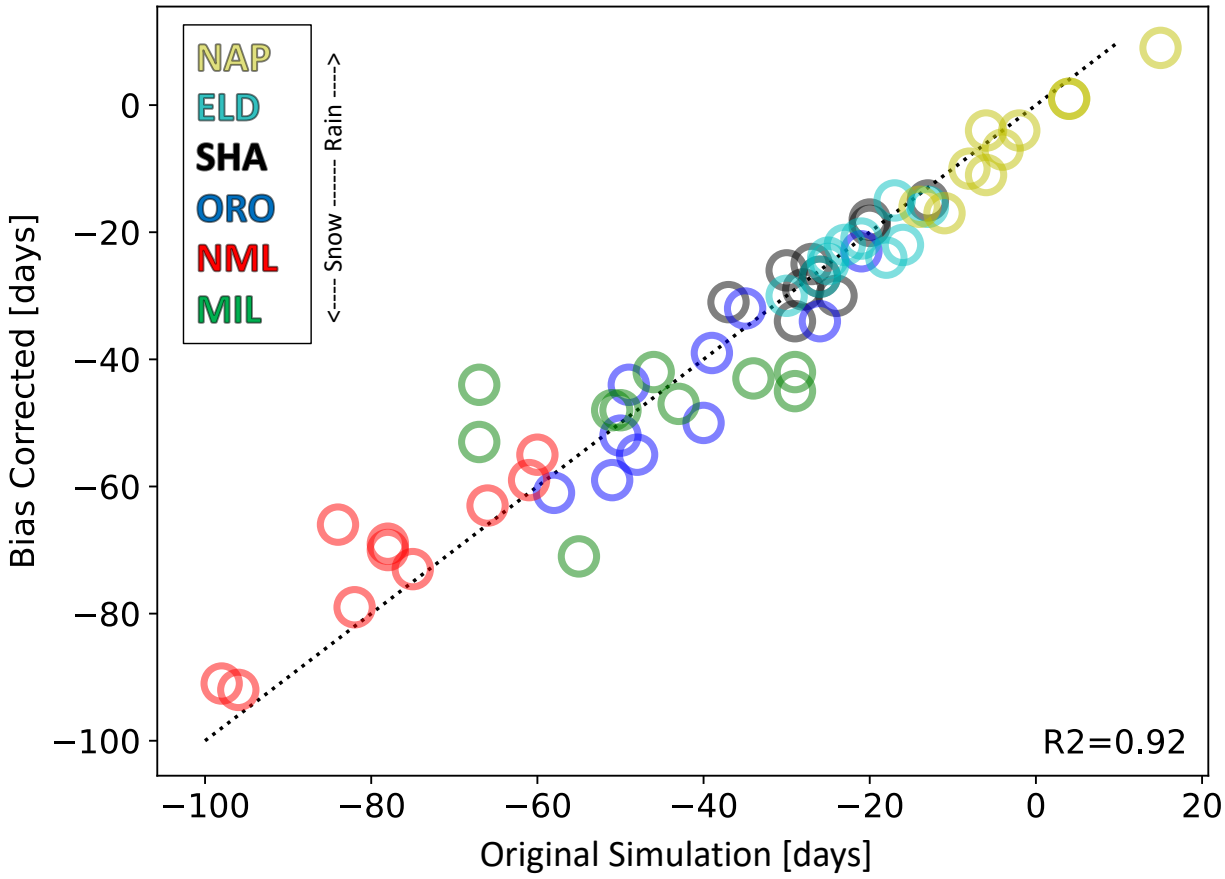

Figure 3.9. Change in timing of peak climatological streamflow for the original model change (x-axis) and PresRat with seasonally anchored windowing (y-axis) between the end-of-century and historical periods. Markers represent the change for each GCM and are color-coded by stream. A dotted black 1-to-1 line is shown for reference.

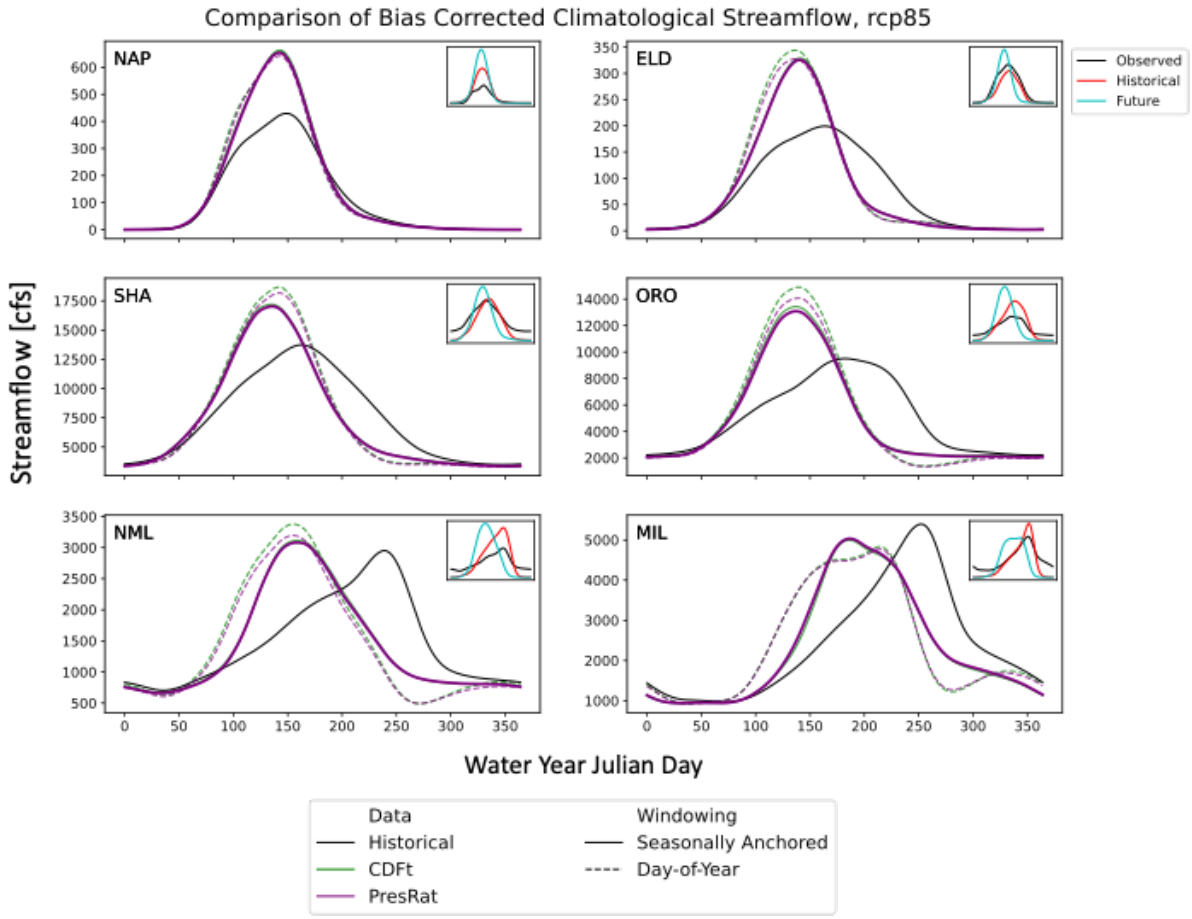

Figure 3.10. Ensemble mean climatological hydrographs for raw and bias corrected data at each of the 6 streams. The upper inlay depicts observed (black) and original model hydrographs of the historical (red) and end-of-century (blue) periods for each river. The main subplots show the bias corrected historical hydrograph (black) alongside end-of-century bias corrected hydrographs for PresRat (purple) and CDFt (green) using seasonally anchored (solid) and day-of-year (dashed) windowing methods.

3.8 Appendix A: Identification of Peak Streamflow Milestone for Bimodal Climatological Hydrographs

Section 3.4.1.2 describes the process of selecting peak streamflow milestones. While the vast majority of climatological hydrographs assessed in this study are not bimodal, for some future projections of historically snow-dominated rivers, the climatological hydrograph contains two local maxima (Figure 3.1A). Recall that the purpose of the seasonally anchored windowing technique is to conduct bias correction across data with similar background physical and environmental processes. The peak milestone in the historical period corresponds to streamflow generated from snowmelt. The future period bimodal hydrograph is characterized by what is likely an earlier rain-dominated peak and a later-season snowmelt-dominated peak. Although the rain-dominated peak may be higher in magnitude, we select the later, snowmelt peak for the location of the milestone to better ensure that the data used in the bias correction shares similar physical and environmental processes.

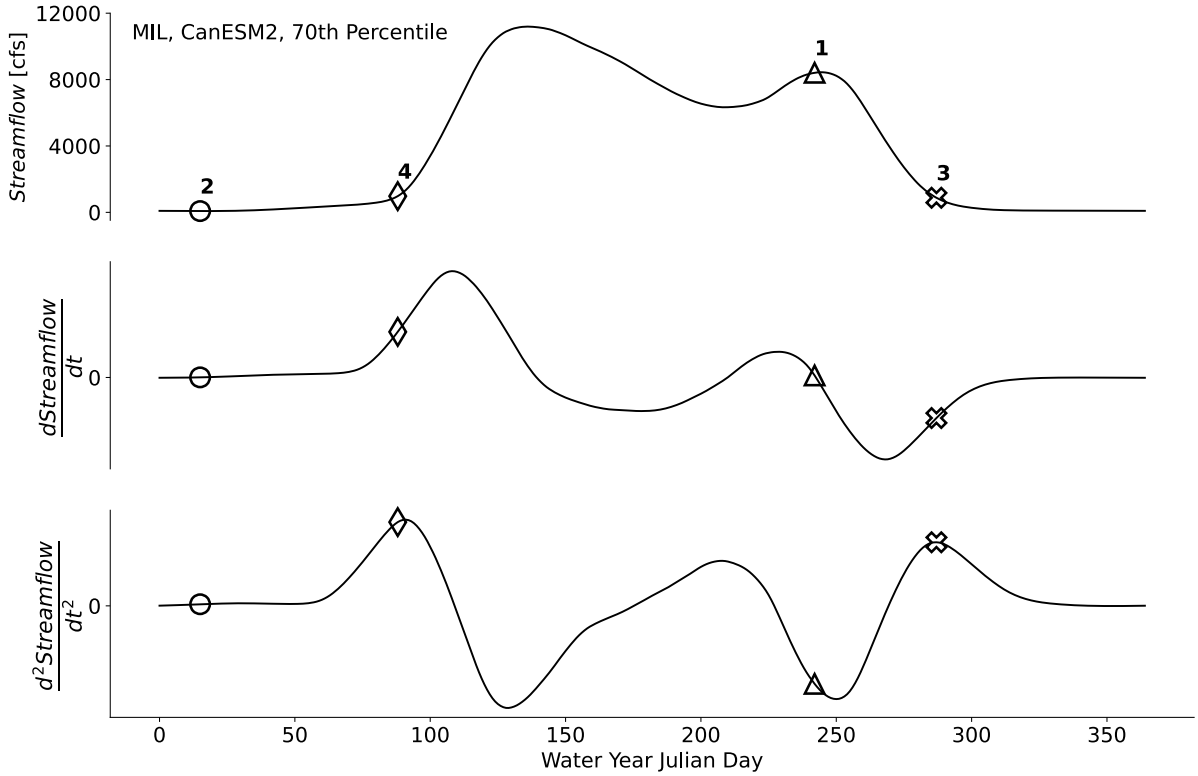

Figure 3.1A. Visual depiction of the algorithm used to identify climatological milestones for the seasonally anchored windowing method for the special case of bimodal hydrographs. End-of-century climatological data from the Millerton/Friant Dam stream and CanESM2 GCM is shown at the 70th percentile to illustrate the method. Daily mean climatological streamflow (top), and the first and second derivatives of streamflow with respect to time (middle and bottom respectively) are plotted on against water year Julian day. Numerical annotation is used to indicate the workflow by which the four seasonal milestones are assigned: (1) Peak streamflow (triangle), (2) Minimum streamflow (circle), (3) Start of the dry season/end of receding limb (x), and (4) Start of the wet season/beginning of the rising limb (diamond). Note that the peak milestone (triangle), is not associated with the true maximum value of streamflow, but rather with the local maximum during the snowmelt period.

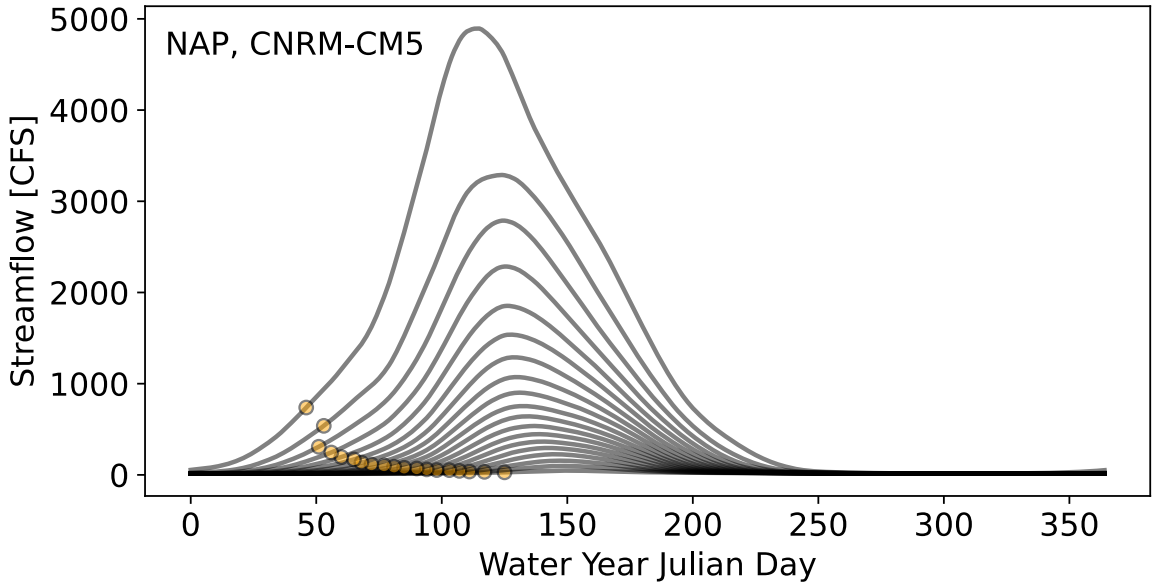

Figure 3.2A. Climatological hydrographs (lines) for flows ranging from the 5th to 95th percentile by intervals of 5 percentage points. Here, we see how the location of the 'start of wet season' milestone (circle) varies as a function of quantile.

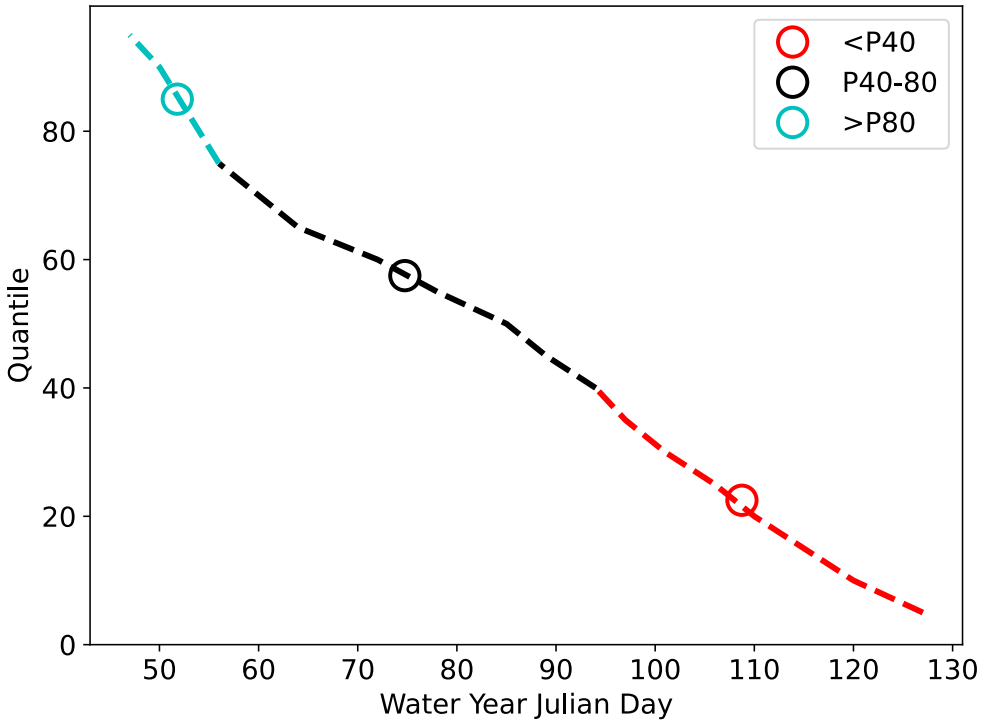

Figure 3.3A. Day of water year associated with the 'start of wet season' milestone (from Fig. 3.2A) for flows below 40th percentile (red), 40th-80th percentile (black), and above 80th percentile (blue). The mean value over each respective range is indicated by a circle.

3.9 Appendix B: Original Model Change in Wet Season Streamflow by Decile

In accompaniment of Figure 3.6 in Section 3.5.3, Appendix B provides the original model signal in wet season streamflow change by decile for the remaining 5 rivers.

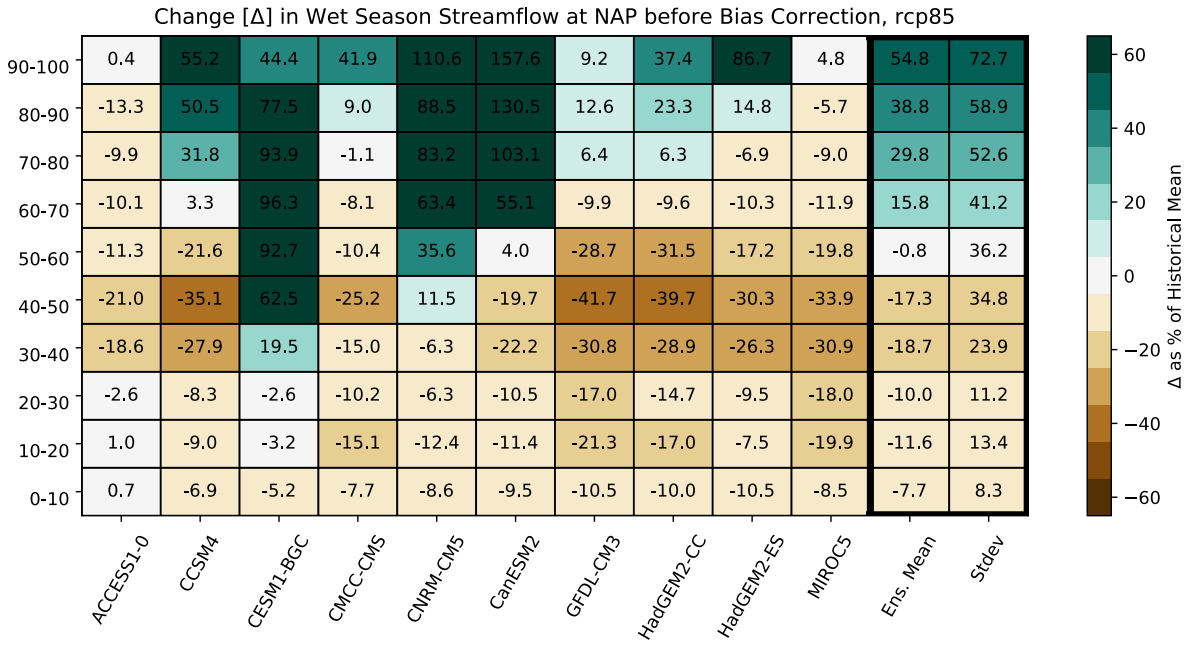

Figure 3.1B. Original model projected change in Napa River streamflow by decile (rows) and GCM (columns) with the 10-member ensemble mean and standard deviation (farthest right columns). Using units of 'percent change from the historical mean', increasing streamflow is indicated by green color-shading, and decreasing streamflow by brown. Values under 5% change appear as white.

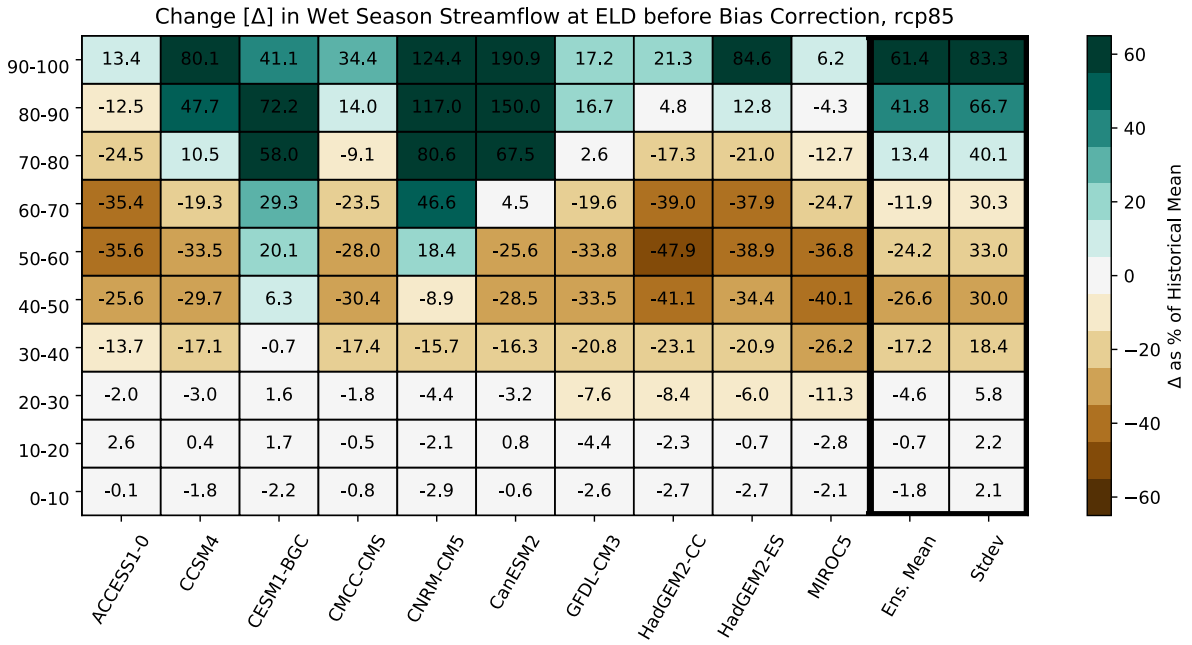

Figure 3.2B. Original model projected change in Elder Creek streamflow by decile (rows) and GCM (columns) with the 10-member ensemble mean and standard deviation (farthest right columns). Using units of 'percent change from the historical mean', increasing streamflow is indicated by green color-shading, and decreasing streamflow by brown. Values under 5% change appear as white.

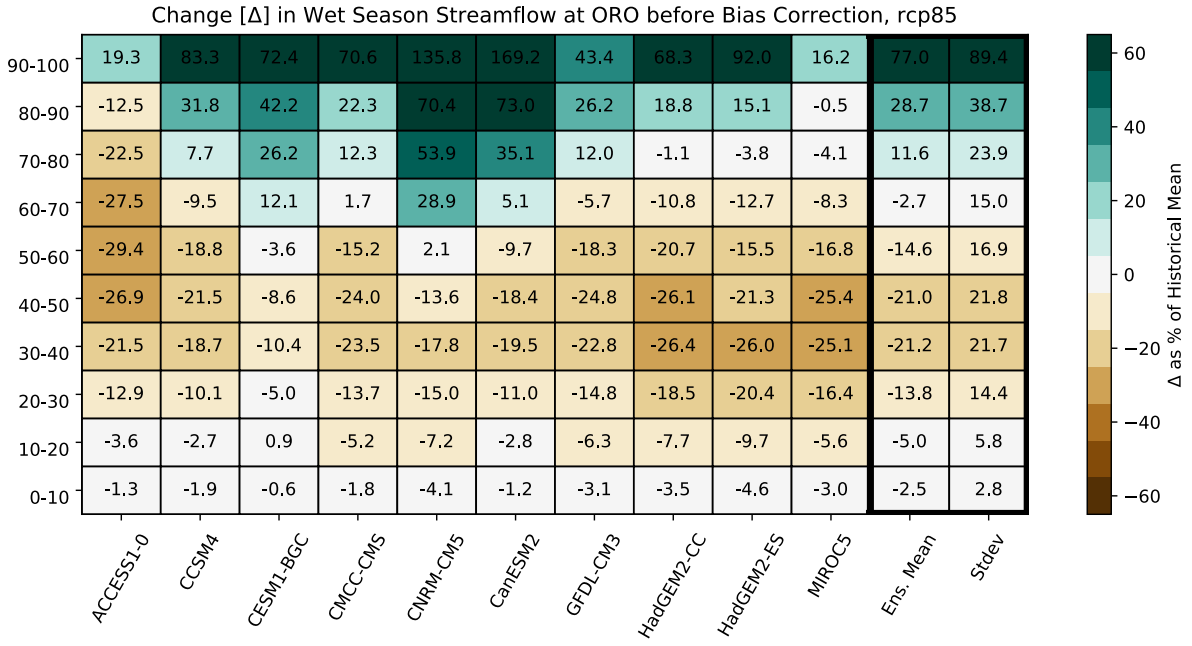

Figure 3.3B. Original model projected change in Oroville Dam streamflow by decile (rows) and GCM (columns) with the 10-member ensemble mean and standard deviation (farthest right columns). Using units of 'percent change from the historical mean', increasing streamflow is indicated by green color-shading, and decreasing streamflow by brown. Values under 5% change appear as white.

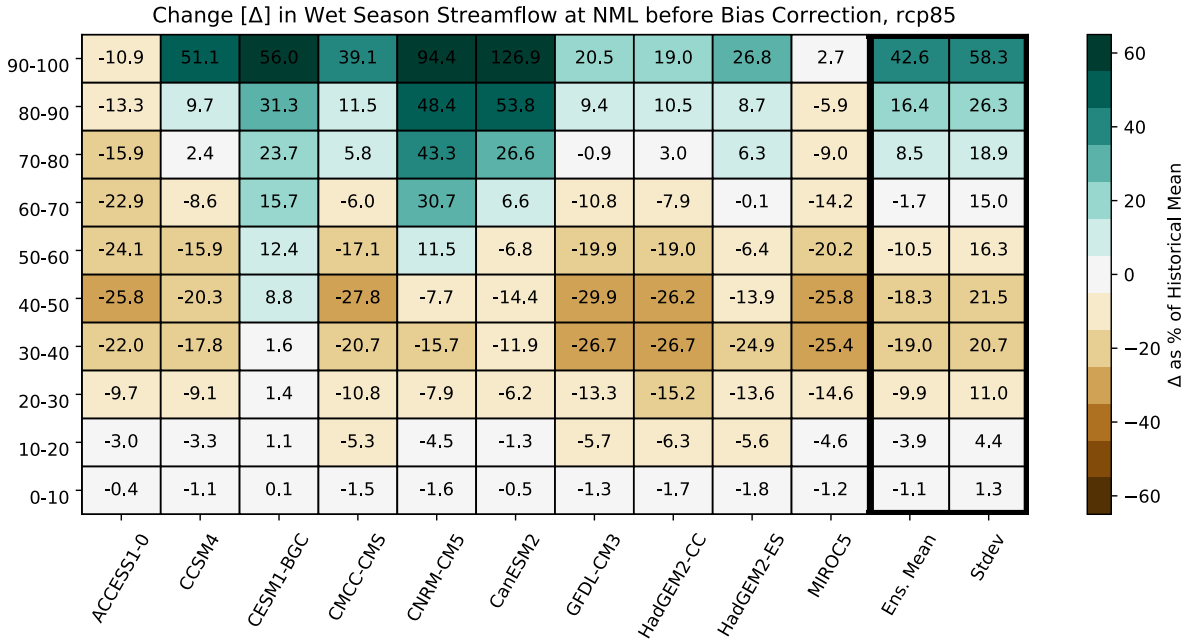

Figure 3.4B. Original model projected change in New Melones Reservoir streamflow by decile (rows) and GCM (columns) with the 10-member ensemble mean and standard deviation (farthest right columns). Using units of 'percent change from the historical mean', increasing streamflow is indicated by green color-shading, and decreasing streamflow by brown. Values under 5% change appear as white.

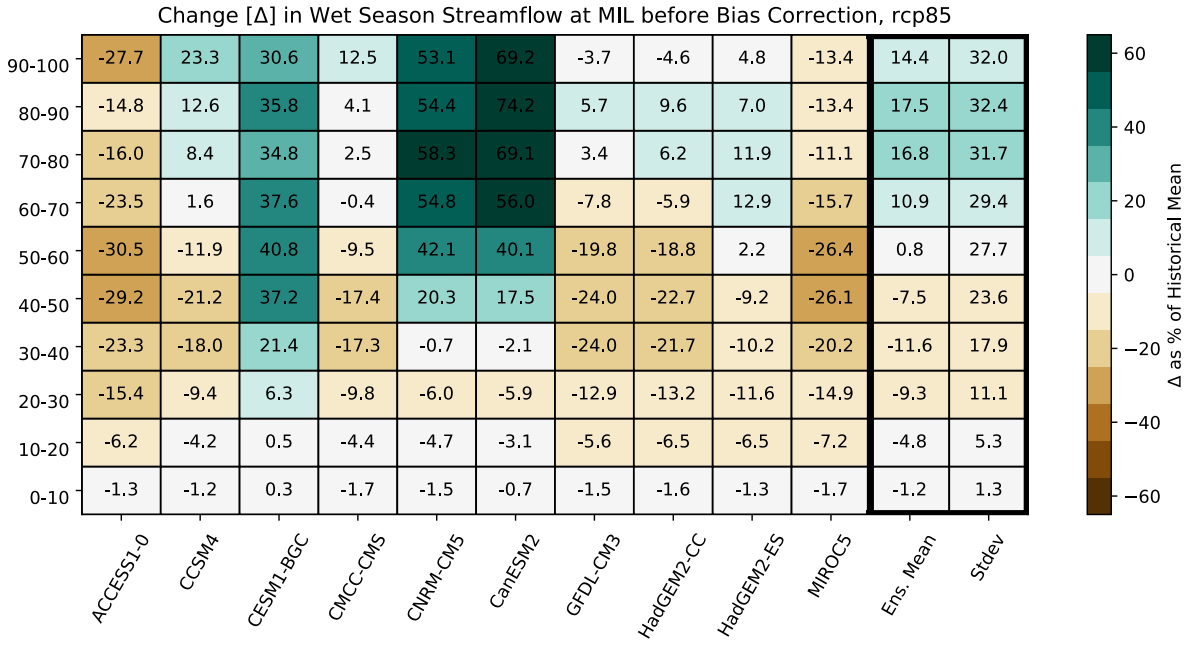

Figure 3.5B. Original model projected change in Millerton/Friant Dam streamflow by decile (rows) and GCM (columns) with the 10-member ensemble mean and standard deviation (farthest right columns). Using units of 'percent change from the historical mean', increasing streamflow is indicated by green color-shading, and decreasing streamflow by brown. Values under 5% change appear as white.

3.10 Appendix C: Error in Wet Season Streamflow by Decile

In accompaniment of Figure 3.7 in Section 3.5.3, Appendix C provides the error in wet season streamflow change by decile for the remaining combinations of bias correction and windowing techniques.

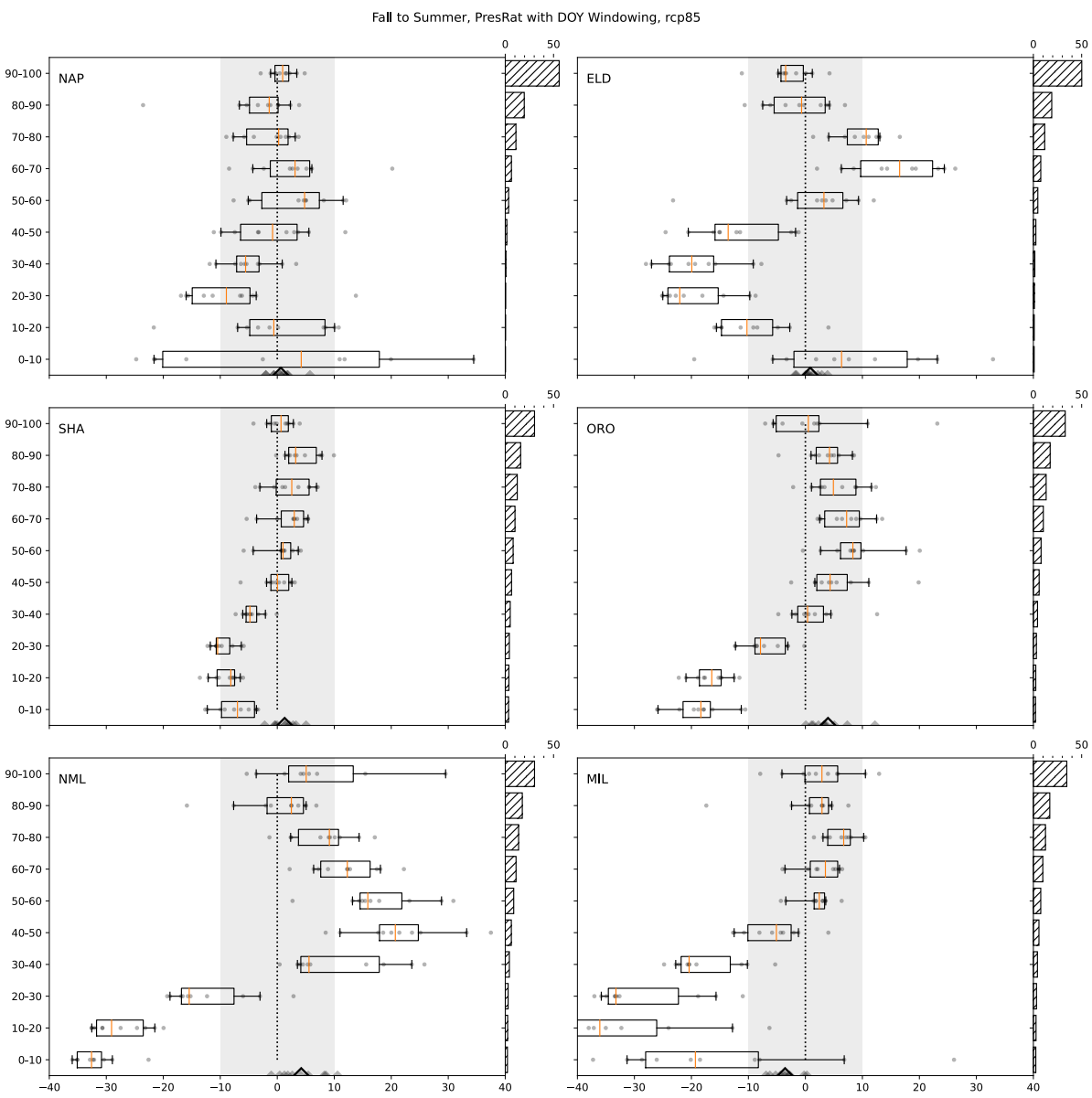

Figure 3.1C. Error by decile for change in wet season streamflow for PresRat with standard day-of-year windowing. Errors (x-axis) for individual GCMs are depicted by grey circles, the mean error across the 10-member ensemble is depicted by an orange line. The box edges and whiskers represent the middle 5 and 8 GCMs respectively. The error for a single GCM averaged over all deciles is depicted as a small grey triangle on the x-axis and the value for the 10-member ensemble mean is denoted by a large triangle. For reference, the grey shading and dashed black line correspond to ± 10% error and 0% error respectively. For each stream, the right y-axis depicts the historical percentage of total wet season streamflow contained in each decile averaged across the 10-member ensemble. Subplots are organized so that as you move down the rows, streams transition from rain- to snow dominated over the historical period.

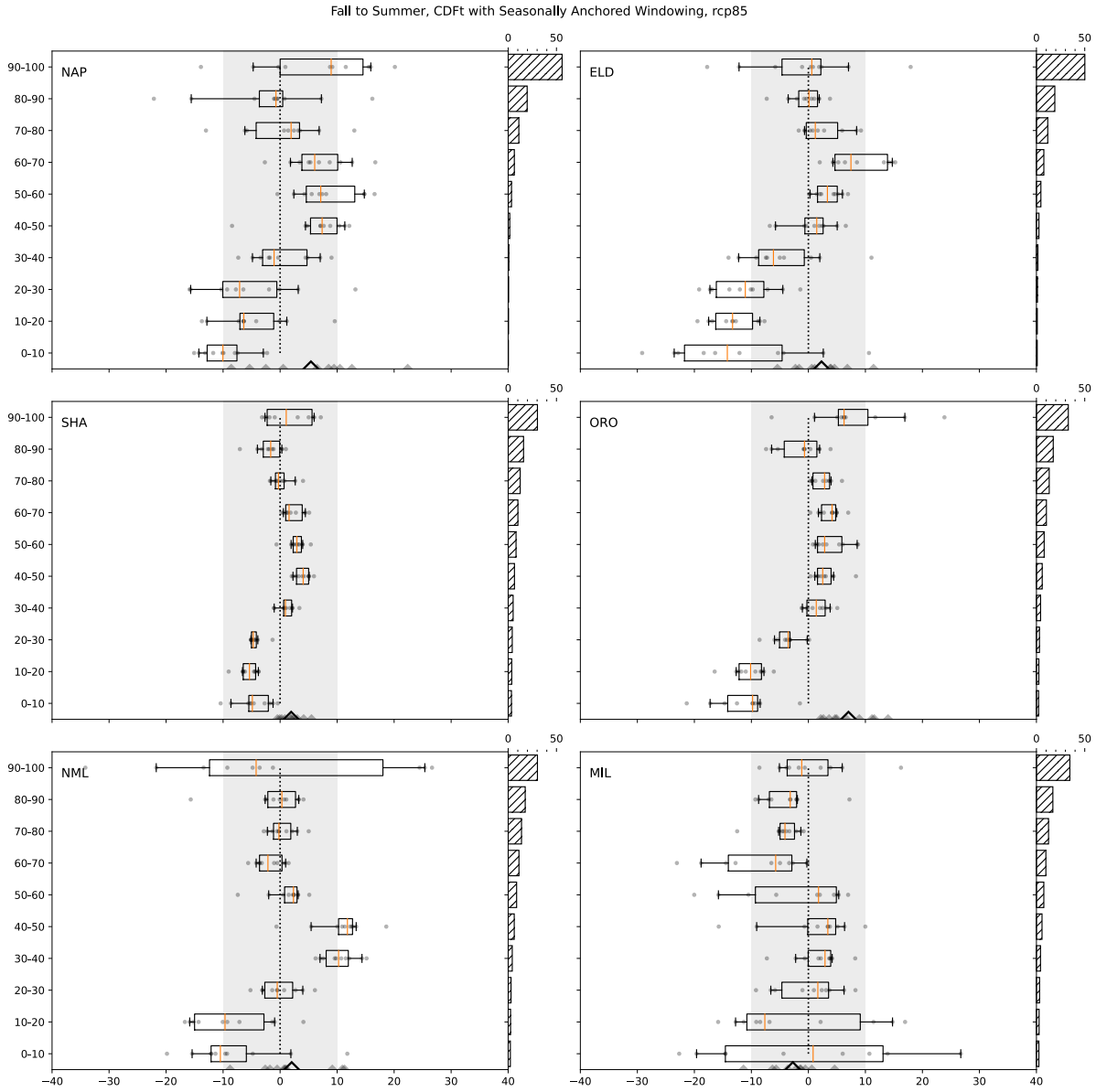

Figure 3.2C. Error by decile for change in wet season streamflow for CDFt with seasonally anchored windowing. Errors (x-axis) for individual GCMs are depicted by grey circles, the mean error across the 10-member ensemble is depicted by an orange line. The box edges and whiskers represent the middle 5 and 8 GCMs respectively. The error for a single GCM averaged over all deciles is depicted as a small grey triangle on the x-axis and the value for the 10-member ensemble mean is denoted by a large triangle. For reference, the grey shading and dashed black line correspond to ± 10% error and 0% error respectively. For each stream, the right y-axis depicts the historical percentage of total wet season streamflow contained in each decile averaged across the 10-member ensemble. Subplots are organized so that as you move down the rows, streams transition from rain- to snow dominated over the historical period.

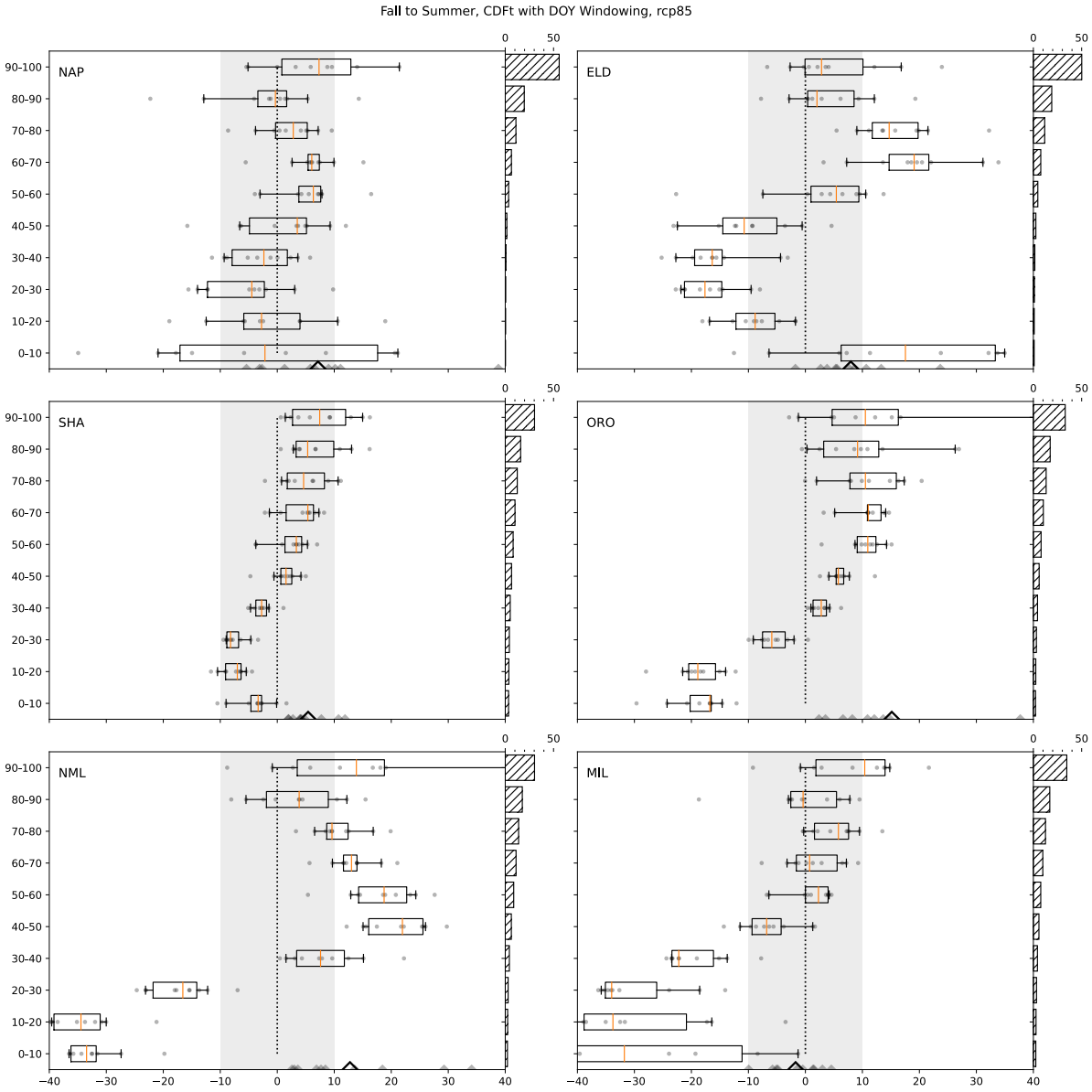

Figure 3.3C. Error by decile for change in wet season streamflow for CDFt with standard day-of-year windowing. Errors (x-axis) for individual GCMs are depicted by grey circles, the mean error across the 10-member ensemble is depicted by an orange line. The box edges and whiskers represent the middle 5 and 8 GCMs respectively. The error for a single GCM averaged over all deciles is depicted as a small grey triangle on the x-axis and the value for the 10-member ensemble mean is denoted by a large triangle. For reference, the grey shading and dashed black line correspond to ± 10% error and 0% error respectively. For each stream, the right y-axis depicts the historical percentage of total wet season streamflow contained in each decile averaged across the 10-member ensemble. Subplots are organized so that as you move down the rows, streams transition from rain- to snow dominated over the historical period.

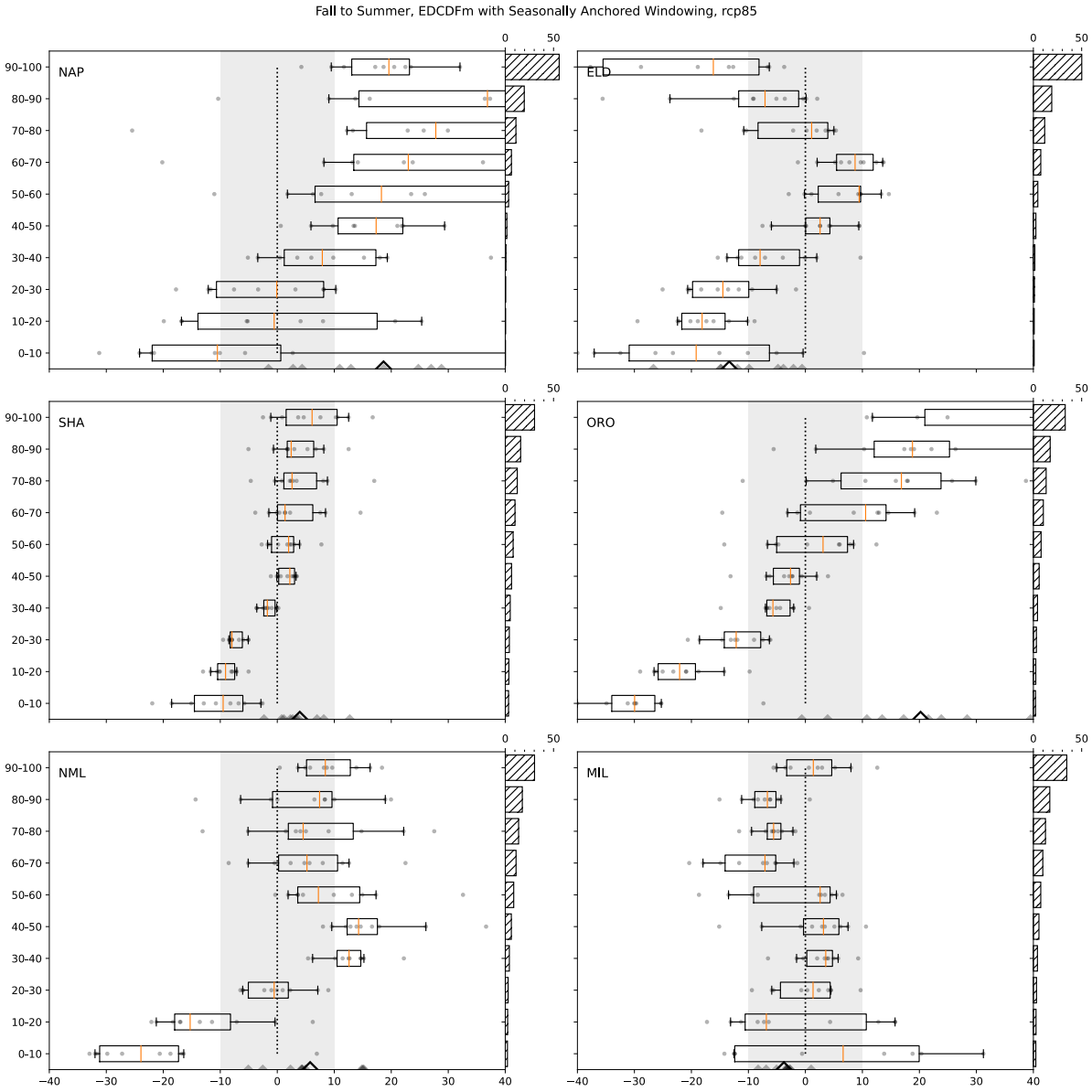

Figure 3.4C. Error by decile for change in wet season streamflow for EDCDFm with seasonally anchored windowing. Errors (x-axis) for individual GCMs are depicted by grey circles, the mean error across the 10-member ensemble is depicted by an orange line. The box edges and whiskers represent the middle 5 and 8 GCMs respectively. The error for a single GCM averaged over all deciles is depicted as a small grey triangle on the x-axis and the value for the 10-member ensemble mean is denoted by a large triangle. For reference, the grey shading and dashed black line correspond to ± 10% error and 0% error respectively. For each stream, the right y-axis depicts the historical percentage of total wet season streamflow contained in each decile averaged across the 10-member ensemble. Subplots are organized so that as you move down the rows, streams transition from rain- to snow dominated over the historical period.

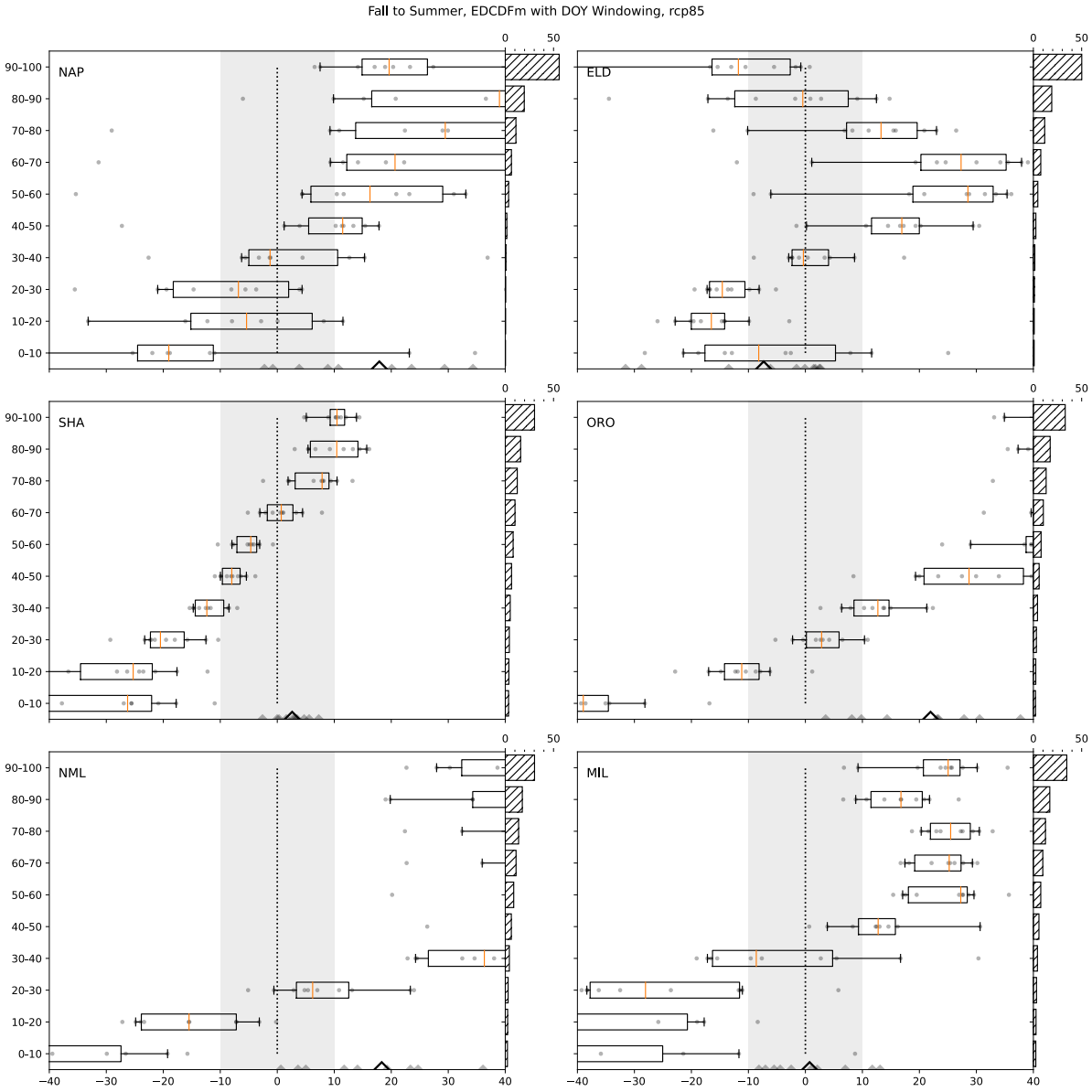

Figure 3.5C. Error by decile for change in wet season streamflow for EDCDFm with standard day-of-year windowing. Errors (x-axis) for individual GCMs are depicted by grey circles, the mean error across the 10-member ensemble is depicted by an orange line. The box edges and whiskers represent the middle 5 and 8 GCMs respectively. The error for a single GCM averaged over all deciles is depicted as a small grey triangle on the x-axis and the value for the 10-member ensemble mean is denoted by a large triangle. For reference, the grey shading and dashed black line correspond to ± 10% error and 0% error respectively. For each stream, the right y-axis depicts the historical percentage of total wet season streamflow contained in each decile averaged across the 10-member ensemble. Subplots are organized so that as you move down the rows, streams transition from rain- to snow dominated over the historical period.

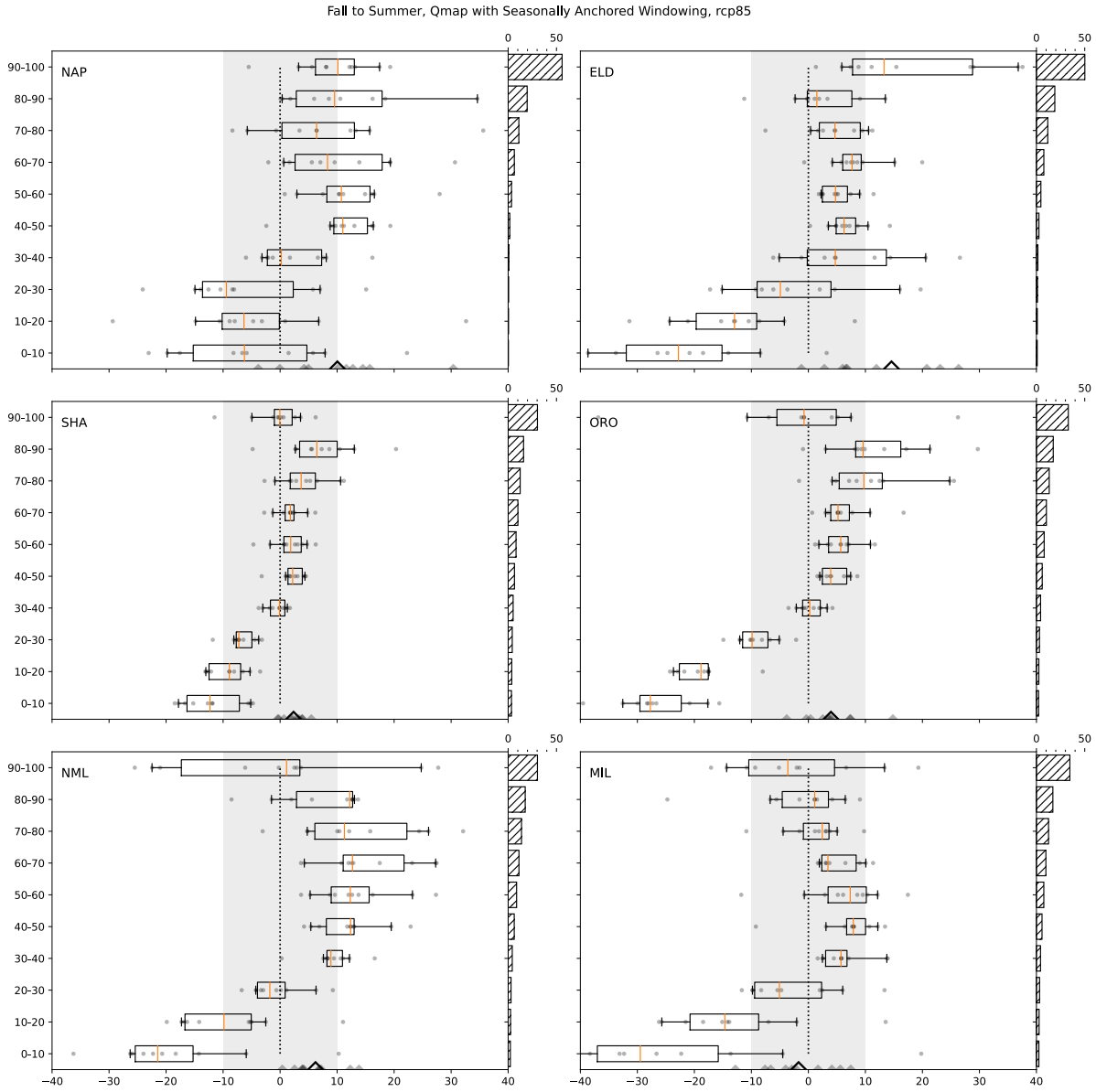

Figure 3.6C. Error by decile for change in wet season streamflow for Qmap with seasonally anchored windowing. Errors (x-axis) for individual GCMs are depicted by grey circles, the mean error across the 10-member ensemble is depicted by an orange line. The box edges and whiskers represent the middle 5 and 8 GCMs respectively. The error for a single GCM averaged over all deciles is depicted as a small grey triangle on the x-axis and the value for the 10-member ensemble mean is denoted by a large triangle. For reference, the grey shading and dashed black line correspond to ± 10% error and 0% error respectively. For each stream, the right y-axis depicts the historical percentage of total wet season streamflow contained in each decile averaged across the 10-member ensemble. Subplots are organized so that as you move down the rows, streams transition from rain- to snow dominated over the historical period.

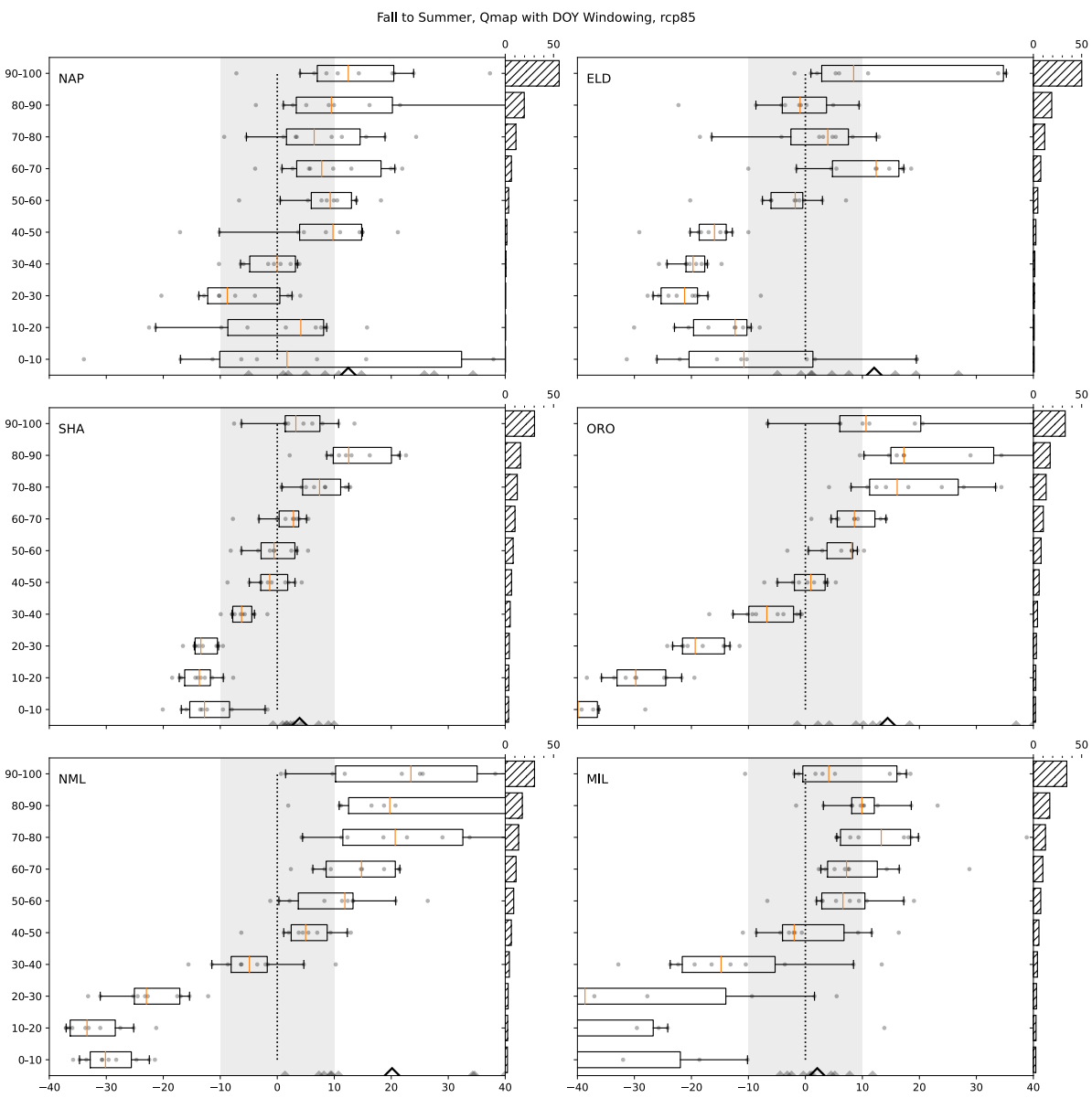

Figure 3.7C. Error by decile for change in wet season streamflow for Qmap with standard day-of-year windowing. Errors (x-axis) for individual GCMs are depicted by grey circles, the mean error across the 10-member ensemble is depicted by an orange line. The box edges and whiskers represent the middle 5 and 8 GCMs respectively. The error for a single GCM averaged over all deciles is depicted as a small grey triangle on the x-axis and the value for the 10-member ensemble mean is denoted by a large triangle. For reference, the grey shading and dashed black line correspond to ± 10% error and 0% error respectively. For each stream, the right y-axis depicts the historical percentage of total wet season streamflow contained in each decile averaged across the 10-member ensemble. Subplots are organized so that as you move down the rows, streams transition from rain- to snow dominated over the historical period.

Chapter 4

Climate Change Impacts on Lake Shasta: Assessing Adaptation Measures for California's Largest Reservoir

Abstract

Climate change is exacerbating the long-standing tensions between water supply and flood-risk mitigation across the Western US and beyond. As springtime snowmelt declines in the face of warming trends, reducing opportunities to refill reservoirs after wintertime flood risks subside, water managers face the decision whether to continue operations designed for a bygone era or to pursue adaptation measures. Differences in factors such as climate, hydrology, and reservoir operations between basins require that impacts of climate change and proposed adaptation strategies be examined on a case-by-case basis. This study investigates projected climate change impacts on California's Lake Shasta and identifies specific variables that govern its vulnerability. Using a newly developed, highly flexible model, we analyze coming threats to water supply and flood risk under existing operations and several forms of adaptive responses to climate change. Compared to the historical period, we simulate 27% declines in carryover storage at the end of the 21st century, under the more severe of two warming scenarios, if operations are left unchanged. Compounding the direct impacts due to decreased snowpack, we find existing reservoir operating procedures are responsible for one-third of average losses. Both operational and infrastructural adaptive measures were explored by altering rule curve and increasing reservoir storage capacity. Despite many interventions favoring water supply over flood risk, historical levels of carryover

storage were irretrievable at the end of the century under the warmer of the two warming scenarios examined in this study.

4.1 Introduction

The water-supply and flood-management systems of the western US were built for hydroclimates that no longer exist. Mountain snowpack, once robust and dependable, has previously been the backbone of the water resources used to fuel economic and agricultural expansion-- at the expense of Indigenous people and native ecosystems (Middleton-Manning et al., 2018). Carefully designed to exploit the past's asynchronous arrivals of rain-driven and snowmelt-fed streamflows, many reservoirs are managed to maintain a measure of empty space behind the dam during boreal winter (called the flood-pool) as a trap for possible flood inflow in order to reduce downstream flooding, while also relying on springtime snowmelt to refill storage capacity after major flood risks have completed most of their "normal" seasonal declines (US. Army Corps of Engineers, 1977). Since the mid 20th century, snowmelt and snow-fed streamflows have been arriving earlier in the year (Mote et al. 2005; Stewart et al. 2005), and projections of 21st Century climates confidently indicate that snowpack will continue to decline and seasonal inflow peaks come earlier as freezing levels rise and a greater fraction of precipitation falls as rain as opposed to snow (Barnett et al., 2008; Leung et al., 2004; Nijssen et al., 2001) . As a result of these earlier inflows, the long-standing seasonal separation between most flood risks and substantial snow-fed inflows is breaking down, in ways that will necessarily stress water resource management (Barnett et al., 2008; Brekke et al., 2009; Cayan et al., 2001; Cohen et al., 2020; N. Knowles et al., 2018; Pierce et al., 2008).

An inflow season that is condensed to the winter and early spring, paired with additional climate change impacts such as increased likelihood of rain-on-snow events and more intense

storms, pose greater flood risk for mountain reservoirs (Barnett et al., 2008; Cohen et al., 2020). Additionally, because a large fraction of reservoir inflows during the wet season are not converted to storage gains (being sapped instead by flood-management releases), in the absence of snowmelt inflows, reservoirs will not be able to refill as designed (Cohen et al., 2020; Knowles et al., 2018; Sterle et al., 2020). Without the vast natural reservoir of mountain snowpack that has historically characterized many of the West's river basins, the longstanding competition between flood-risk mitigation and water supply reliability will intensify as water managers are forced to respond to increasingly difficult scenarios with infrastructure designed for a bygone hydroclimate (Christensen et al., 2004; Knowles et al., 2018; Knowles et al., 2006; Lee et al., 2006).

In response, there is a large body of work focused on operational or structural adaptation strategies to combat projected climate change impacts (Brown et al., 2012; Christensen & Lettenmaier, 2007; Cohen et al., 2020; Georgakakos et al., 2012; He et al., 2020; Moody & Brown, 2013; Steinschneider & Brown, 2012; Sterle et al., 2020; Wilby & Keenan, 2012, and many others). Future conditions are imposed using either global climate model (GCM) simulations (e.g. He et al., 2020; Payne et al., 2004) or synthetic scenarios corresponding to a particular risk exposure (e.g. Herman et al., 2016; Weaver et al., 2013) and these vulnerability and adaptation studies can vary widely in scope. Some apply a systems-level approach and investigate multiple reservoirs within the context of larger interconnected and highly dynamic water resources portfolios (e.g. Knowles et al., 2018; Tanaka et al., 2006). Others offer insight on local scales and individual reservoirs (e.g. Sterle et al., 2020; Willis et al., 2011). Often, experiments are designed to focus either specifically on flood risk, often analyzing a small number of selected storms at a daily timestep, or water supply issues, typically resolved at a monthly timestep over long periods.

The present study explores impacts at Shasta from a multi-objective (water supply and flood-risk mitigation) perspective on timescales ranging from days to decades.

To accomplish this, we developed a simplified model of California's largest reservoir, Lake Shasta, which is capable of responding to downscaled and bias corrected global climate model (GCM) data to simulate reservoir operations and releases on a daily timestep over many decades. We begin by projecting climate-change-driven inflows and then respond to those inflows using the reservoir's operating protocol. We then evaluate climate-change impacts on projected reservoir performance under existing protocols. With baseline performance established, we investigate the capacity of both operational and infrastructural adaptation measures to mitigate increasing tensions between water supply and flood-risk mitigation.

The paper is structured in the following manner. Section 4.2 details pertinent hydrological and operational details of Lake Shasta. Section 4.3 discusses both the data used in model development and that used for the future simulations. The model development and validation is detailed in Section 4.4 with further information in the Supplemental. Section 4.5 presents results from future climate runs under existing operations and selected adaptations. Lastly, Section 4.6 summarizes and connects this work to the broader literature.

4.2 Background

4.2.1 Lake Shasta Watershed

Lake Shasta, contained by Shasta dam, is located in the Trinity Alps of California roughly 260 km north of Sacramento, CA (Figure 4.1). Completed by the U.S. Bureau of Reclamation in 1949 as a major part of the Central Valley Project, Shasta Lake is the largest reservoir in California with over 4.5 million acre feet (MAF) of storage capacity and represents roughly 10% of the state's storage capacity (US. Army Corps of Engineers, 1977). Historically, the cumulative water year

inflow to the reservoir is 5.9 MAF, or enough to fill the entire reservoir 1.3 times (US Department of Interior, 2011). The reservoir operates with joint water supply and flood control objectives and is managed by the U.S. Bureau of Reclamation.

Shasta Dam drains 16,500 km^2 of mountains and plateaus including parts of the Trinity and Cascade Ranges at the head of Sacramento Valley. The two principal tributaries to the Sacramento River above the dam are the Pit and McCloud Rivers. Although there is a network of small hydroelectric dams along the Pit River, they develop very little storage and do not significantly modify flood flows (US. Army Corps of Engineers, 1977). Elevations within the basin range from 180 m at the dam to 4,250 m at Mt. Shasta with 65% of the basin lying below the climatological snowline (1,200 m) and 97% below 2,100 m (US. Army Corps of Engineers, 1977). Above the dam, the Sacramento River, which flows into Lake Shasta and which Shasta manages downstream flows to Sacramento Valley, has two distinct seasonal peaks--one during winter fed by rainfall and early snowmelt runoff and one spring in springtime fed by snowmelt. This bimodal hydrograph distinguishes it from most other major northern California rivers, such as the Feather and Yuba, which are principally snow-dominated and have their only major seasonal peaks in springtime (e.g., Dettinger & Cayan, 2003).

4.2.2 Reservoir Operations

Like so many reservoirs engineered to provide flood-risk mitigation and water supply benefits, Lake Shasta is operated using a 'rule curve' that dictates the maximum allowed storage level on an individual day of the year. During the flood-risk season, this level is kept low to ensure sufficient vacant space is available to capture high inflow events and then rises through the spring as flood risk wanes. Unlike many reservoirs, maximum storage values at Shasta are not dictated by a single rule curve but by 6 separate curves, referred to here as sub-rule curves. The decision of

which sub-rule curve to enforce on a given day is determined by the current Inflow Parameter (Equation 4.1) based on the magnitude of recent reservoir inflows, according to

$$\boldsymbol{Inflow\ Parameter_i} = (\mathbf{0.95} * \boldsymbol{Inflow\ Parameter_{i-1}}) + \boldsymbol{Inflow_i} \quad (4.1)$$

where i indicates the date. When the inflow parameter value increases, the mandated sub-rule curve (dictated by the day's inflow parameter) favors flood-risk mitigation by lowering the mandated maximum storage level (darker blue curves in Fig. 4.2); when the parameter decreases, the mandated sub-rule curve allows maximum storage levels to rise reflecting a growing prioritization of water supply (paler blue curves). Each of the 6 sub-rule curves has a corresponding range of inflow parameter values (Supplemental section 4.8.1). Over the course of a given water year, the operative rule curve (red) can jump between each of the 6 individual curves (blue shading) based on recent inflows. The vertical black dashed line (Fig. 4.2) corresponds to what we will refer to as the reservoir's refill date when the sub-rule curves transition overall from favoring flood-risk mitigation to favoring refilling of the water supply. Coinciding with the historical peak in mean daily inflow, the refill date at Lake Shasta occurs on March 20th.

4.3 Data

4.3.1 Historical Period

Historically measured data for a variety of Shasta-specific variables (reservoir inflows and outflows, air temperature, evaporation) and weather and snow stations around its watershed (precipitation and snow water equivalent) were obtained from the California Department of Water Resources Data Exchange Center (CDEC) for water years 1996-2017 (See list of stations in Supplemental section 4.8.6). Gridded reanalysis snow-water equivalents (SWE) data from Broxton et al. (2019) and Livneh et al. (2013), together with precipitation data from PRISM (Daly et al., 1994) and Livneh et al. (2013) were also used (with the station data) in development of the

statistical model of Lake Shasta described in Section 4.4. We use multiple gridded datasets for a given variable to extend temporal coverage over the entire period of record (discussed further in Supplemental section 4.8.5).

4.3.2 Future Climate Projections

For climate-change experiments, daily temperatures, precipitation, and SWE values statistically downscaled using the Localized Constructed Analogs (LOCA) method (Pierce et al., 2014) applied to Coupled Model Intercomparison Project Phase 5 (CMIP5; Taylor et al., 2012) climate change scenarios were obtained. LOCA is designed especially to be advantageous for investigations of extreme precipitation (Pierce et al., 2014), which are critical to reservoir operation. Streamflow projections used in this study come from Sierks et al. (2022), which provides secondary bias-corrections of data from Knowles and Cronkite (2018) and Ratcliff (2018) that was derived from the variable infiltration capacity (VIC) hydrologic model (Liang et al., 1994) simulations of responses to the same downscaled CMIP5 projections (see Sierks et al. 2022 for details). In the present study, we investigate projections from 10 GCMs chosen by the California DWR Climate Change Technical Advisory Group as providing good simulations of the California hydroclimate (California Department of Water Resources Climate Change Technical Advisory Group, 2015, listed here in Table 4.1) and examine climates projected under radiative concentration pathways (RCP) 4.5 and 8.5.

4.4 Model Development and Validation

The daily simulation of Lake Shasta storage is governed by a simple water balance equation,

$$Storage_i = Storage_{i-1} + Inflow_i - Outflow_i - Evaporation_i \quad (4.2)$$

at each day, i. Inflow is available at each timestep, initial storage is known, and evaporation can be estimated through linear regression based on storage and temperature data (see Supplemental). Simulation and testing of the evolution of storage, historically and in future-climate experiments, is thus contingent on estimation of daily outflows, which are the managed controls on the right side of Equation 4.2. The reservoir outflows (also referred to as releases) vary greatly by season and are decided based on a wide range of local and remote conditions, for a variety of flood-risk, instream-flow requirements, agricultural demands, and Bay-Delta salinity management purposes (U.S. Bureau of Reclamation, 2019b). Reflecting the differences between wet- and dry-season operations, the model of Lake Shasta has separate modules for the flood-risk management and water-supply seasons, which are outlined briefly below and covered in detail in Supplemental sections 4.8.2 and 4.8.3.

4.4.1 Wet-Season Operations

Because flood risk can change rapidly from day-to-day, faithful simulation of daily releases during the winter is required to properly reproduce historical and future wintertime storages and flood risks. If the 24-hr inflow volume, when added to the previous day's storage, causes the reservoir stage to increase above the rule curve, releases are dictated by the US Army Corps of Engineers Flood Control diagram (Chart A-8; US. Army Corps of Engineers, 1977), shown in Fig. 4.2. We refer to this as a flood-risk release. From October 1st through April 30th, if reservoir storage is below the rule curve, simulated outflow is based on climatological mean values. Complete details about rule curve and climatological releases can be found in Supplemental section 4.8.2.

4.4.2 Dry-Season Operations

Unlike winter releases that are based on daily reservoir inflow and storage values, May 1st through September 30th outflows are based on a predicted total seasonal release volume (unless a flood-risk release is required on a given day). This seasonal release volume is derived from the California Department of Water Resources (DWR) Bulletin-120 (B120), which forecasts dry-season runoff across major watersheds in the state. In the process, DWR calculates a Water Year Index (WYI), a nondimensional value related to 'how wet' a water year is in relation to a baseline (See Supplemental section 4.8.3). Although complex external variables such as Bay-Delta salinity, stream temperatures, total California reservoir storage, and agricultural demand impact daily summertime deliveries, our aim is to analyze water-supply risk on timescales of seasons to decades, not days. Thus, we focus on total dry season release volumes for our water supply analysis. In practice, the U.S. Bureau of Reclamation relies on seasonal inflow forecasting in part to allocate releases (U.S. Bureau of Reclamation, 2019a). So, we find that the B120 information is both sufficient for our purpose and in-line with official reservoir operations. For complete details on dry-season operations, including how the WYI is estimated and then translated into a seasonal release volume, see Supplemental section 4.8.3.

4.4.3 Model Calibration and Validation

Using, leave 1-year out, cross-validation over the historical period (WYs 1996-2017), we calibrate and evaluate the model's performance over the period of record. Each of the 22 WYs is simulated independently while estimating model parameters (namely, WYI and associated principal components, see Supplemental section 4.8.3 for full details) from the remaining 21 years of data. Figure 4.3 shows the daily storage in Lake Shasta over the historical period for the observed and simulated data with lower subplots depicting mean outflow and storage performance. We validate our model in this manner to ensure that our system generalizes for each year well and

does not over-fit the training data. Relevant summary statistics are provided in Table 4.2 as well. As anticipated due to the complexity of water supply operations, the model has better daily performance during the wet season. However, residuals in both daily storage and carryover storage, a good indicator of system performance (Draper & Lund, 2004) defined as storage on September 30th, are small (in R2 sense), randomly distributed, do not manifest a significant systematic bias, and importantly lead to no long-term model drift.

4.5 Results and Discussion

4.5.1 Streamflow Changes

Before examining whether and how simulated reservoir performance is impacted by global warming, we must understand how the underlying hydrological conditions change. We do so by first evaluating how Shasta inflows are impacted by climate change, and second, how such changes relate to operations. Concerning both total WY precipitation and total WY inflows, there is a large spread among the 10 GCMs about the sign and magnitude (in units of percent of historical value) of change. The range of 30-yr means from the various GCMs is roughly between -15 % change and +25% change for both precipitation and streamflow variables. Focusing now on streamflow, the ensemble mean increases by 3.5% in both RCPs when comparing inflows during the historical period (1970-2005) to the end-of-century (2069-2099). Unlike the mean signal, however, there is unanimous agreement that the top decile of streamflow values will increase in magnitude. Additionally, daily peak streamflow shifts earlier by nearly 1 month, causing the average inflow volumes to increase during the October-April season and decrease in the May-September season (Fig. 4.4). This seasonal shift occurs under both RCP scenarios, though winter (spring/early summer) streamflow increases (decreases) more under RCP8.5 than it does under the RCP4.5 scenario.

4.5.1.1 Seasonal Inflow Timing and Magnitude Changes

In the context of Shasta's specific operations, we find that inflows increase during the flood-risk season (prior to the refill date of March 20th) throughout the 21st century whereas those occurring after the refill date decline (Fig. 4.5). Compared to the 1970-2020 historical mean, there is an average 23% (15%) decrease in cumulative streamflow after the refill date under RCP8.5 (RCP4.5). These decreases prevent the reservoir from refilling as much of the flood pool as during the historical period. Concerning projected winter inflows, ensemble mean changes reflect a 21% (17%) increase in pre-March 20th reservoir inflows under RCP8.5 (RCP4.5). Whereas the historical partition between pre- and post-refill inflows was fairly balanced at 56% to 44% of total WY flows respectively, the gap widens to 67% to 33% (64% to 36%) under RCP8.5 (RCP4.5) as inflows consolidate into the flood-risk season.

4.5.1.2 Inflow Parameter

Because the daily rule-curve storage limit at Lake Shasta is based on the magnitude of recent reservoir inflows (Section 4.2.2), both the increase in high decile flows and the condensed (see Fig. 4.5), earlier inflow season have direct impacts on reservoir operations. Recall that, when inflows are large, the mandated operations favor flood-risk mitigation by enforcing a more restrictive sub-rule curve. Figure 4.6 shows the average percentage of days between December 23rd and March 20th, the period before refill, that each of the 6 sub-rule curves is mandated during a given winter. As October-April inflow increases throughout the century, so too does the frequency of inflow-parameter values that require enforcement of more restrictive storage limits. In fact, the frequency of the most conservative sub-rule curve (Fig. 4.6, dark blue), quadruples (doubles) by the end of the century climbing from 5% to 20% (10%) of days for RCP8.5 (RCP4.5).

Here we see how the increase in streamflow magnitude during the flood-risk season results in lower annual-mean levels of maximum-allowable storage.

4.5.2 Operations Under Existing Rules

Before potential adaptation measures are addressed, we quantify the impacts of climate change on reservoir performance under existing operations. To do so, we compare water supply and flood-risk mitigation objectives over 50-year periods (historical: WYs 1970-2020, end-of-century: WYs 2050-2099). Figure 4.7 highlights the ensemble-mean 50-yr mean values of cumulative inflow, storage, and the mandated rule curve (RC) for each day of the water year. Additionally, the right y-axis shows the frequency distributions of daily storage from each year in the 50-yr period for each individual GCM as for comparison to the ensemble mean. Under the RCP8.5 (RCP4.5) scenario, we find a 17% (10%) decrease in WY mean storage, 11% (5%) decrease in WY maximum (referred to as 'peak') storage, and a 27% or 710 TAF (16% or 420 TAF) decrease in carryover storage, measured on September 30th of each water year, compared to the historical period.

As described in Section 4.5.1, a transient climate state will alter water supply attributable to both hydrological (decreased snowmelt) and operational (dynamic rule curve) drivers. With cumulative storage losses detailed, we now seek to isolate the individual contribution of each of the above components. To understand the impact of the dynamic rule curve on carryover storage loss, we identify the date and value of the rule curve on each instance when a flood-risk release occurs (i.e., if $Storage_{i-1} + Inflow_i > RC_i$). This is illustrated in Figure 4.7 which shows the evolution of simulated reservoir storage for WYs 1989 (solid black) and 2095 (solid red) with corresponding rule curve values as dashed lines. The date and storage level associated with the final flood-risk release of each WY is depicted by a circle. Broadly, the rule curve has the largest

impact on storage when a flood-release is required late in the wet season (ex. April) and the rule curve is more restrictive (WY2095 vs. WY1989). The value of the rule curve matters because it dictates the extent to which storage levels are suppressed (i.e., a more restrictive sub-rule curve leads to greater impact on peak/carryover storage). The timing of the flood-risk encounter matters because only reservoir inflows occurring after the final flood-risk release can build storage above the encountered rule curve value. Therefore, we track the date and storage value of the rule curve on the final flood-risk release of a given water to estimate the impact of the dynamic rule curve on reservoir storage.

Figure 4.8 highlights the 50-yr average date and storage value associated with the final flood-risk release in a given water year (large circle – ensemble mean, small circle – individual GCM). We find very little change in the timing of the ensemble mean final flood-risk release from the historical era (which occurs on March 12th) with RCP8.5 (RCP4.5) moving earlier 3 days (1 day) on average. Note that the date of the final flood-risk release is similar to the reservoir refill date of March 20th. We find a small decrease in the variability (measured by the ensemble standard deviation) concerning the timing of the final flood-risk release from the historical value of 7 days to 6.5 days under both RCP scenarios. When comparing the ensemble mean storage value of the rule curve associated with the final flood-risk release, we find increasingly restrictive values compared to the historical (3.68 MAF). Under RCP8.5 (RCP4.5), the end-of-century mean value is 3.48 MAF (3.53 MAF), which corresponds to a 200 TAF (160 TAF) reduction in storage compared to the historical average.

Although we simulate little change in the timing of the final flood-risk release, we see markedly decreased amounts of reservoir inflow after the final flood-risk release compared to the historical era (2.64 MAF) due to the hydrological changes (decreased snowmelt). Under RCP8.5

(RCP4.5), we simulate reservoir inflows occurring after the final flood-risk release of a given WY to be 2.20 MAF (2.40 MAF) yielding a decrease of 440 TAF or 17% (250 TAF or 9%) relative to historical values.

As detailed in Section 4.5.1, increased flood-risk under projected future climate is manifested into operations through the dynamic rule curve and directly impacts the reservoir's ability to build storage by enforcing more restrictive sub-rule curves on average. Further, we simulate decreased (relative to the historical baseline) reservoir inflows occurring after the final flood-risk release of a given water year coinciding with decreasing snowmelt. When we examine these two components against the total carryover storage loss, we find that diminished snowmelt inflow and increased flood-risk are responsible for 66% and 33% of the total carryover storage loss respectively under both of the RCP scenarios.

To quantify flood-risk, we evaluate the frequency with which emergency spillway releases are required (see Supplemental for further details). In short, this occurs when the reservoir is experiencing large inflows and storage levels are relatively high and increasing, signaling potential for serious flood risk. Over the historical period under simulated existing operations, at least one of the 10 ensemble members requires the use of the emergency spillway in 0.6% of the water years. In our simulation, the frequency of emergency spillway years increases to 2.8% (1.4%) under RCP8.5 (RCP4.5) over the 2050-2099 period. Despite more frequently operating under a rule curve that favors flood-risk mitigation (at the expense of water supply), we find flood risk still increases by a factor of 4.5 (2.3) for RCP8.5 (RCP4.5) during the end-of-century period. Though not shown here, we will illustrate how flood-risk evolves in time in the following sections.

Given these significant declines in reservoir storage under climate change, we next explore the efficacy of several much-simplified options for changing reservoir operations and capacity as

possible directions for climate-change adaptation. For each option, the sensitivity of (and ability to recoup losses from) these climate-change impacts under current operating rules is simulated and summarized below.

4.5.3 Sensitivity to Changing the Refill Date

Similar to Cohen et al. (2020) and Sterle et al. (2020), we assess whether moving the refill date earlier in the water year is an effective operational adaptation strategy in the face of waning snowmelt. For Shasta, the refill date (as defined here) occurs on March 20th in anticipation of the historical transition from flood-risk to snowmelt seasons. Conceptually, allowing the reservoir to refill earlier in the water year in response to a future with earlier inflows might recoup otherwise lost storage. To examine the sensitivity of storage losses to the reservoir refill date, we run the model with refill dates ranging from 10-to-40 days before and after March 20th and compare resulting reservoir operations by the end-of-century period under these modified rule curves to the historical baseline under existing operations. Figure 4.9a shows that peak and carryover storage increase almost linearly as the refill date is moved to earlier in the water year. As detailed in Section 4.5.2, under historical operations (0-days of refill date shift in Fig. 4.9a), peak storage levels (pink markers) drop by roughly 0.4 MAF (0.2 MAF) under RCP8.5 (RCP4.5). By moving the refill date 20 days earlier in the year, the historical levels of peak storage could be recovered under RCP4.5, but carryover storage (teal markers) losses would still be well below historical levels (by roughly 0.2 MAF). Indeed, even at 40 days earlier, under RCP8.5, peak storage levels only just meet the historical baseline while carryover storage loss totals 0.34 MAF (a -13% historical decrease). For context, although this is a marked decrease under RCP8.5, the 40-day-earlier shift does recoup roughly ½ the carryover storage that would have been lost under existing operations. Under

RCP4.5, nearly all the lost carryover storage is recovered simply by shifting the refill date back by 40 days.

While carryover storage is a useful metric to track long-term water-supply reliability (Draper & Lund, 2004), we also examine the impact of shifted refill dates on the occurrence of critically low reservoir levels (Fig. 4.9b), defined here as carryover storage values below the 10th percentile of historical carryover storage volumes. By the end of the century, the average water year sees 4 (2) out of 10 GCMs yielding carryover storage values that are below this critically low level under RCP8.5 (RCP4.5). Shifting the refill date 40 days earlier reduces the frequency of reaching the critical value to 23% (12%) of ensemble members for RCP8.5 (RCP4.5) respectively.

Meanwhile, the water-supply storage benefits owing to setting earlier reservoir refill dates (Fig. 4.9) come at the cost of increased flood risk. Over the historical period under simulated existing operations, at least one of the 10 ensemble members requires the use of the emergency spillway in a 0.6% of the water years. If the refill date and rule curves are not modified, the frequency of emergency spillway use increases by 4-fold (2-fold) under RCP8.5 (RCP4.5) over the 2050-2099 period. Here, in the earliest refill experiment (40 days prior to March 20th), future spillway frequency is 8x (6x) higher than the historical period under existing operations (Fig. 4.10). While recouping some storage losses when compared to existing operations, this adaptation mechanism roughly doubles the simulated end-of-century flood-risk.

4.5.4 Sensitivity to Use of a Single Rule Curve

In response to the role of the dynamic rule curve in storage decline, we also perform an experiment in which the existing sub-rule curves are replaced with a single curve. Unlike existing operations, the daily value of maximum storage in this experiment is independent of recent inflows. Here, we simulate reservoir performance using each of the 6 current sub-rule curves

shown in Figure 4.2. As before, we compare the end-of-century performance of the adaptation simulations to simulated performance during the historical period with existing operations. Fig 4.11a shows ensemble-mean changes in peak and carryover storage when each of the sub-rule curves is applied separately under RCP4.5 (hollow circles) and RCP8.5 (filled circles) climates. On average, operating Shasta with the least restrictive sub-rule curve (RC 1 in Fig. 4.2) yields carryover storage levels about equal to the historical norms under RCP4.5 and losses are limited to about 0.2 MAF or -7% under RCP8.5 (compared to 27% by century's end under RCP8.5 and existing operations). Interestingly, when compared to the single rule curve operations, we find that the existing dynamic rule curve (diamond markers) yields similar end-of-century carryover and peak storage to the single-RC4 simulation. When examining critically low carryover storage, enforcing only the least restrictive sub-rule curve (RC1) reduces the frequency of reaching critical values from 45% (23%) under existing operations to 16% (9%) for RCP8.5 (RCP4.5) respectively.

Analogous to the previous section, the water-supply storage benefits resulting from enforcing less restrictive sub-rule curves (Fig. 4.11) come at the expense of increased flood risk. Compared to existing operations, which resulted in a 4-fold (2-fold) increase in flood-risk, we simulate a 13-fold (12-fold) increase in the frequency of spillway releases under the least restrictive sub-rule curve for RCP8.5 (RCP4.5) highlighting the steep cost of limiting water supply losses in this adaptation scheme (Fig. 4.12). For the sub-rule curve RC4 experiment, which had similar storage metrics to existing operations, we find that flood-risk increased by a factor of 5 (2) under RCP8.5 (RCP4.5) yielding similar results to the existing operations which had a 4-fold (2-fold) increase.

4.5.5 Sensitivity to Raising the Dam

Infrastructure changes at Shasta Dam have been proposed and studied at length as an improvement or adaptation option (United States Bureau of Reclamation, 2015). Specifically, a proposal exists to raise the height of the dam by 18.5 feet (5.6 m), which would increase storage capacity by 634,000 TAF or 14% of existing capacity. To examine the impact of additional storage on the system's climate-change vulnerability, we conduct several experiments. First, we increase the storage capacity in the model, including raising all sub-rule curves along with the dam by increasing all rule curve values to include the new 634,000 TAF of storage. This approach retains the current pool volume and effectively just adds the new capacity to the non-flood-pool storage. In a second simulation, we raise the top of the rule curve (the warm-season storage limit) while leaving the bottom of the winter flood pool at the current value of 3.25 MAF. Conceptually, this second scenario increases the volume of the flood pool available to capture larger inflows while also increasing the capacity for long-term carryover storage.

As the difference between the two experiments centers on how the rule curve is adapted, we follow the analysis presented in Section 4.5.2, which focuses on the impact of the dynamic rule curve in restricting storage. Similar to existing operations, there is little change in the timing of the final flood-risk release of a given water year (Fig. 4.13 circle marker, x-axis value) in either experiment. However, the storage value associated with the final flood-risk release (Fig. 4.10 circle marker, y-axis value) is roughly 0.6 MAF higher (meaning less restrictive) for the experiment that raises all rule curve values (brown shading) than the experiment that leaves the bottom of the winter flood pool at the current value of 3.25 MAF while raising the warm season storage limit (blue shading).

In comparison to baseline historical operations (Fig. 4.13, black lines), raising the dam and sub-rule curves (first approach; Fig. 4.13, brown lines) is simulated to yield a 105 TAF decrease

(160 TAF increase) in carryover storage under RCP8.5 (RCP4.5). As context, adding 14% additional storage capacity results in a 4% decrease (6% increase) in carryover storage at the end of the century under RCP8.5 (RCP4.5) compared to the historical norm. If we raise the dam and only the top of the rule curve (second approach; Fig. 4.13, blue lines), so that the bottom of the rule curve stays at historical values, only marginal end-of-century improvements from existing operations (710 TAF and 420 TAF losses for RCP8.5 and RCP4.5 respectively) are simulated. In this scenario, carryover storage losses total 630 TAF or 24% (330 TAF or 13%) under RCP8.5 (RCP4.5) compared to the historical average. Clearly stated, if the storage value associated with the bottom of the flood-pool (3.2 MAF) is left unchanged (Fig. 4.13, blue lines), the rule curve restricts storage in a way that negates any potential carryover storage benefits from increased capacity.

Directly comparing the two experiments, measured against existing operations, raising everything (increase all rule curve values by new capacity) buys 0.6 MAF of additional carryover storage under both RCP scenarios while raising the warm-season storage limit and leaving the bottom of the winter flood pool at the current value of 3.25 MAF yields roughly 0.08 MAF of additional storage under both RCP scenarios. Of the two experiments, from a water-supply perspective, raising all rule curve values alongside the additional storage would be the only useful approach as a climate-change adaptation.

Due to its larger flood-pool, the second experiment, in which only the top of the rule curve is raised with the dam, decreases flood risk relative to existing operations under simulated future climate. Under both RCPs, flood-risk at the end of the century matches that of the existing operations for the historical period thus highlighting the efficacy of this adaptation strategy at mitigating projected increases in flood-risk. When both the rule curve and top of the dam are

increased together (first experiment), the rule curve operations and flood-pool volume are unchanged from existing operations. Therefore, the resulting flood-risk, as measured by the frequency of years requiring emergency spillway releases, is identical to existing operations under projected future climate and results in a 4-fold (2-fold) increase compared to the historical period under RCP8.5 (RCP4.5).

4.5.5 Sensitivity to Perfect Forecast Operations

Having examined both rule curve- and infrastructure-based adaptation mechanisms at Lake Shasta, we perform a final experiment that is a much-idealized version of forecast-informed reservoir operations. To try to determine theoretical maximum storages possible under the stresses of climate change, we set aside rule curve-based reservoir operations and instead simulate operations that manage flood releases based entirely on perfect forecasts. Under this scheme, there is no mandated flood pool during the winter so that the maximum-allowable storage is the highest rule curve value (4.55 MAF) every day of the water year. Using a version of the forecast-operations strategy developed by Delaney et al. (2020) we simulate reservoir operations assuming perfect forecast skill at a range of lead times. Rather than respond to 'water on the ground', the reservoir operator makes pre-releases, if necessary, to vacate space for imminent inflows. When forecasted inflows would raise storage above the maximum-allowable level, the releases that are just enough water so that the reservoir storage is returned to the maximum allowable value at the end of the forecast window are determined each day. This release rate is then capped to restrict release rates to the reservoir's maximum non-spillway release of 79 TCFS. If the cumulative inflow volume exceeds the cumulative maximum release integrated over the forecast window, rather than trigger a spillway release, storage may increase beyond the maximum allowable value. We evaluate reservoir operations under assumptions of perfect forecasts with forecast horizons of 1-, 3-, 5-, 7-

,10-, and 14 days, which sits at and beyond the theoretical limit of weather predictability (Lorenz, 1963). In the event that pre-releases are not required to prevent storage from increasing above the 4.55 MAF level, existing protocols (Section 4.4.1 and 4.4.2, Supplemental section 4.8.2 and 4.8.3) of non-flood-risk release are followed.

We note that different forecast horizons will yield different flood-risk metrics (due to varied ability to vacate empty storage volume behind the dam). Because 1) all forecast horizons allow storage to increase up to its maximum-allowable level, and 2) forecast horizons are only important for operations when flood-risk releases are necessary, as storage begins its seasonal decline (when reservoir releases exceed inflows during the spring/summer) forecast horizons become irrelevant to operations. Owing to this fact, both peak and carryover storage metrics are independent of perfect forecast window in this experiment.

Under these idealized operations, for years in which the wet-season inflow volume is enough to fill the reservoir, Lake Shasta is kept full for as long as inflows meet or exceed releases. In years with insufficient inflow to fill the reservoir, which is projected to occur with increasing frequency under both warming scenarios (though more under RCP8.5), storage will remain below capacity. Using the approach shown in Figure 4.7, we track the daily values of the ensemble mean storage averaged across the 50-yr climatological period (Fig. 4.14). With existing operations over the historical era shown for context (black curves), we illustrate the annual cycle of storage under perfect forecast operations using a 7-day forecast horizon (although this result is not sensitive to forecast horizon) under RCP8.5 (purple) and RCP4.5 (orange) scenarios. Whereas the historical storage curve (solid black) climbs slowly from December to May (while being subjected to the rule curve), the perfect forecast simulations (purple and orange lines) rise more rapidly (uninhibited by any flood-pool) as a larger volume of water fills the reservoir during the winter

months on average. In response, ensemble mean peak storage over the 50-yr period increases by 0.18 MAF (0.26 MAF) from the historical baseline of 3.97 MAF to reach values of 4.15 MAF (4.23 MAF) under RCP8.5 (RCP4.5). As spring inflows wane and demand-driven releases begin, the perfect forecast storage begins its decline up to 20-30 days earlier than the pre-warming era. Despite the increase in peak storage, under RCP8.5 (RCP4.5), end-of-century carryover storage decreases (increases) by roughly 0.07 MAF, or 3% of the historical level. Here, we see that even if we abandon enforcement of a flood-pool, allow the reservoir to reach full capacity as early in the water year as possible, and allow it to stay at full volume for as long as possible, earlier peak streamflow and reduced snowmelt during the spring/early summer result in a perfect forecast simulation that only just maintains historical values of carryover storage on average. Put another way, if it is barely possible to achieve historical levels of carryover storage (on average) by the end of the century under RCP8.5 using this idealized scheme built to explore the upper limit of theoretical storage, then it is unlikely that any operational adaptation measure (apart from one that reduces spring release volumes or increases capacity) will be able to achieve historical carryover storage.

Concerning flood risk, for existing operations, we simulated the frequency with which the reservoir requires a spillway release. As mentioned at the start of Section 4.5.6, the perfect forecast simulation doesn't use a spillway (by design). If cumulative reservoir inflow over the forecast horizon exceeds the cumulative allowable releases, storage is permitted to rise above the maximum allowable value. For perfect forecast simulations, we assess flood risk by identifying all years when the storage increases above the maximum allowable value (orange dashed line, Fig 4.14). This metric is analogous to tracking emergency spillway use in existing operations and both represent situations of imminent and extreme risk. Figure 4.15 shows how the frequency of

pseudo-spillway release changes with time under both existing operations (dashed black line) and various perfect forecast horizons (blue lines). Recall that under existing operations, the simulated future climate of RCP8.5 (RCP4.5) yielded a 4-fold (2-fold) increase above historical levels. Placing flood risk under existing operations in the context of perfect forecast simulations, we find that it falls between a 7- and 10-day perfect forecast for both warming scenarios, reflecting the low appetite for flood risk in current reservoir operations. In contrast to this factor of 4 (2) increase, the 3-day perfect forecast simulation yields a 17-fold (12-fold) increase in flood-risk compared to the historical level under existing operations highlighting the sharp increase in flood risk as the forecast horizon is shortened in the absence of any wintertime flood-pool.

4.6 Summary and Conclusion

Climate change will continue to amplify the ever-present tension facing water managers (Christensen et al., 2004; Knowles et al., 2018; Knowles et al., 2006; Lee et al., 2006). Reservoirs that depend on snowmelt to refill after flood-risk subsides, like so many in California, will be confronted with an inflow season that is condensed in time, peaks earlier, is punctuated with higher magnitude runoff events, and finishes with greatly reduced snowmelt contribution. In the face of this growing threat, water managers will be left with the daunting challenge of either continuing to operate a reservoir designed for a bygone era or determining how to adapt operations (or infrastructure) without exacerbating growing risk.

This study develops a simplified model of operations at California's largest reservoir, Lake Shasta, driven by downscaled and bias corrected global climate model (GCM)-driven simulated inflows for the purposes of identifying 1) how climate change impacts reservoir performance, 2)

which variables drive its sensitivity to those changes, and 3) the efficacy of various adaptation mechanisms to mitigate adverse effects of anthropogenic warming on reservoir performance. Capable of faithfully simulating the most pressing operations at daily resolution, we are able to explore impacts on both water supply and flood-risk at timescales ranging from days to decades.

Interestingly, we find that climate change signals are manifested into reservoir performance through both hydrological and operational mechanisms. Compared to the historical average, despite little change in total water year (WY) reservoir inflow, we find a 15% decrease in cumulative inflow during Shasta's refill season (beginning on March 20th) as reduced snowpack limits the ability to rebuild storage after flood-risk wanes. Conversely, we find a 17% increase in inflow volume arriving during the period when the flood risk is largest (pre-March 20th). Because Shasta's rule curve enforces lower maximum-values of storage when recent inflow volumes have been large, the concentration of inflow volume into the winter, coupled with an increase in high magnitude streamflow events, results in more time spent under more restrictive rule curves (from a water supply perspective) thus inhibiting the reservoir's ability to build storage (Figs. 4.5 and 4.6).

Under the stresses of climate change, end-of-century (WYs 2050-2099) carryover storage, measured as storage on September 30th, declines by 27% or 710 TAF (16% or 420 TAF) on average compared to the 1970-2020 baseline under RCP8.5 (RCP4.5). Like Cohen et al. (2020), we find lost snowmelt-driven inflow to be the primary driver of carryover storage loss (responsible for 66% of total decline). However, we also find the impact of Shasta's inflow-dependent dynamic rule curve to be a meaningful contributor, accounting for the other 1/3 of carryover storage loss (Fig. 4.8). Framing the lost storage volume in the context of water demand, to maintain historical carryover storage levels at the end of the century, total May-September reservoir releases would

have to be cut by 20% (10%) on average under RCP 8.5 (RCP4.5) in our simulation. In addition to impacts on reservoir storage, we evaluate the evolution of flood risk in the changing climate by examining how often reservoir emergency spillway releases are required. Despite more frequently operating under a rule curve that increasingly favors flood-risk mitigation (at the expense of storage), we find flood risk increases by a factor of 4 (2) for RCP8.5 (RCP4.5) during the end-of-century period.

Having established a baseline of projected performance under existing operations, we examine the efficacy of several much-simplified options for changing reservoir operations and capacity as possible directions for climate-change adaptation. We begin by simulating two operational strategies that alter the implementation of the existing rule curve. For a first set of experiments, like Cohen et al. (2020) and Sterle et al. (2020), in response to the projected shift of snowmelt-driven inflows earlier in the year, we change the reservoir refill date such that the reservoir is allowed to refill up to 40 days earlier (Fig. 4.9 and 4.10). In the second experiment, motivated by the demonstrated storage-impact of the dynamic rule curve, we remove the inflow-dependency dictating the maximum-allowable storage and simulate operations using each of the 6 individual sub-rule curves (Fig. 4.11 and 4.12). Both schemes recover some lost storage (compared to existing operations) though the amount depends on the degree to which the adaptation measure was taken (refilling 40-days vs. 10-days earlier, using the least restrictive sub-rule curve vs. medium restrictive sub-rule curve). Under RCP8.5, even the most extreme measures are unable achieve historical levels of carryover storage (on average) by the end of the century. In both experiments, altering the rule curve such that it favors water supply results in substantial increases in flood risk, highlighting the tension of the reservoir's competing objectives (Figs. 4.10, 4.12).

Motivated by long-term discussions regarding the raising of Shasta's dam (adding 0.63 MAF, 14% of current capacity), we simulate two scenarios in which the storage capacity is physically expanded. One approach raises all sub-rule curves along with the dam by increasing all rule curve values to include the new 0.63 MAF of storage. This approach maintains the volume of the existing flood-pool, effectively just adding the new capacity to the non-flood-pool storage (Fig. 4.13, brown lines). In the second experiment, we raise the top of the rule curve (the warm-season storage limit) while leaving the bottom of the winter flood pool at its current level of 3.25 MAF (Fig. 4.13, blue lines). Conceptually, this second scheme increases the size of the flood pool available to capture larger inflows while also increasing the capacity for long-term carryover storage. Under the first experiment, nearly all the additional capacity is converted to carryover storage, meaning that instead of the simulated 710 TAF (420 TAF) decreases with existing operations under RCP8.5 (RCP4.5), carryover storage only slightly decreases (4%) from the historical mean under RCP8.5, and actually increases by 6% under RCP4.5. In stark contrast, if the bottom of the flood-pool is left unaltered (experiment 2 here), carryover storage losses nearly match those of existing operations under future climate, although improvements in flood-risk management are realized. Of the two experiments, from a water-supply perspective, raising all rule curve values along with the additional storage would be the more useful approach as a climate-change adaptation.

Finally, we interrogate the theoretical maximum carryover storage under future climate projections. By removing the flood-pool, thus setting the maximum allowable storage to equal the full reservoir capacity on all days of the WY, we operate the reservoir under the assumptions of perfect forecast skill. Conceptually, we permit the reservoir to reach full capacity as early in the water year as possible and allow it to stay at full volume for as long as possible. Despite this highly

idealized operation, reflecting the growing offset between the inflow season and the demand season, earlier peak streamflow and reduced snowmelt during the spring/early summer result in perfect-forecast operations only just maintaining historical values of carryover storage on average (Fig. 4.14). From a flood-risk perspective, we find that existing reservoir operations have the equivalent flood-risk exposure of perfect forecast operations using between a 7- and 10-day horizon while also noting an increase in flood-risk both with respect to decreasing forecast horizons as well as increasing global mean temperatures (Fig. 4.15).

Figure 4.16 presents a comparison of reservoir performance across all operational schemes simulated throughout the study (marker style) under both warming scenarios (color). Flood-risk, evaluated as the mean percentage of ensemble members requiring a spillway release during a given water year averaged over the climatological era, is plotted on the y-axis. Water supply risk, evaluated as the mean percentage of ensemble members whose carryover storage falls below the 10^{th} percentile of historical operations averaged over the climatological era, is plotted on the x-axis. The baseline performance of existing operations over the historical period is indicated by a black-spotted diamond marker with black dashed lines representing its x- and y-values. Simulations with comparable performance to the historical baseline have markers that fall close to the black diamond. Reflecting the tension between the water supply and flood risk, many adaptation measures sacrificed performance in one objective for the other. However, because they make a conscious effort to address (or at least not exacerbate) both flood risk and water supply objectives, the 7-day perfect forecast and increasing both the rule curve and storage capacity (circle and star markers respectively) schemes have the best results.

While the simulated adaptation strategies all mitigated carryover storage losses, to varying extents, compared to existing operations (i.e., adaptation schemes appear to the left of spotted

diamond markers), under RCP8.5, none were able to achieve historical carryover storage levels at the end of the century. Under RCP4.5, the only approaches that matched historical carryover storage without greatly elevating flood risk were the 7-day perfect forecast or increasing both the rule curve and the storage capacity by 0.63 MAF (yellow circle and star respectively).

Setting infrastructure improvements aside, although the 7-day perfect forecast is clearly idealized, forecasts do not need to be perfect to be useful. If we think about the current flood-pool volume (1.3 MAF) in terms of an equivalent number of days at maximum allowable release, we find the flood-pool is equal to 8.3 days at 79 TCFS, the maximum 'non-spillway' release. Using this framework, if forecasts were skillful at 3-day lead time, for example, the flood-pool could be reduced by the volume equivalent of 3 days at maximum allowable release, or 470 TAF here, without increasing the flood risk.

As Lake Shasta is comparatively low in elevation, it has a much more mixed hydrograph (with comparable components of rainfall-runoff and snow-fed runoff) than other basins farther south in the high Sierra Nevada range (Dettinger and Cayan, 2003). Because of that, the amplitudes of climate change signals are smaller than in snow dominated basins, yet we see significant levels of increasing risk to reservoir operations nonetheless. Apart from the $1 billion infrastructure improvement and idealized 7-day perfect forecast, no single adaptation method was able to preserve historical levels of water supply and flood-risk mitigation. However, individual methods assessed in this study adapt to different aspects of the changing climate. Therefore, it is conceivable to combine tactics such as eliminating the inflow-dependent rule curve (impacted by increasing flood-flows) and allowing the reservoir to refill earlier (impacted by decreasing snowmelt). Further, at the time when many of these reservoirs were constructed, existing forecast skill was poor-to-nonexistent (Magnusson & Källén, 2013). Thanks to improvements in both observational

networks and technology, it is possible to leverage existing (or potential) forecast skill to improve operations (Delaney et al., 2020; Nayak et al., 2018). Whether employed individually or in concert, operational adaptation commits to responding to specific climatic changes using a dynamic approach. Because these tactics are operational in implementation and not physical, they require a significantly lower amount of capital than physical improvements. Like United States Bureau of Reclamation (2015), this study showed increasing the storage capacity of Lake Shasta to be an effective adaptation strategy strictly from a water balance perspective. With a price tag exceeding $1 billion, in addition to the cultural and environmental costs, it is unclear how transferrable this approach might be across the West given it does not address the growing incompatibilities of reservoir operations with future climate.

These simplified experiments assume that historical levels of water demand, by proxy of dry season reservoir releases, don't change in time. Although not explicitly included in this analysis, whether or how the amount of water demanded, and the time of year it is needed, for agricultural, metropolitan, or environmental flows changes will have a large impact on future reservoir performance. Additionally, our model follows closely to the historical operations with respect to reservoir releases. In the future, it is certainly possible that Lake Shasta, a single piece of a much larger portfolio of storage and conveyance, may be operated in an ahistorical manner due to new system constraints and demands (i.e., combat sea level rise and bay-delta salinity rather than water supply). Altogether, this work contributes to the growing body of literature highlighting the increasing risks to water supply- and flood-risk mitigation under a warming planet while investigating the sensitivity of adaptation measures in combatting projected changes. Several avenues of future work, such as testing the implementation of several adaptive measures in tandem and examining the existing inflow-forecast skill at Lake Shasta, have the potential to provide

additional insight to those in the water resources community interested in adapting operational strategies to a changing climate. Further, the model developed in this study has the potential to be augmented to investigate reservoir dependent processes such as the projected impacts of climate change on hydropower generation at Lake Shasta or important environmental/ecosystem variables such as stream temperature in the Sacramento River.

Finally, we note that the choice of a specific adaptation scheme is only one part of the decision facing water managers. Next, they must decide how and when operations/infrastructure should be transitioned. One approach could be to choose a given calendar year (ex. 2050) based on GCM projections of simulated hydroclimate; however, such an approach is subject to uncertainties in both GCMs and future human emissions. Another approach could rely on observed climatological shifts (like those seen in Fig. 4.4) to trigger action, focusing on specific signals of warming rather than trusting a given ensemble of GCMs. Given the latter option, our model, or others with a similar approach, could be a useful and important tool in exploring the risks and benefits of transitioning operations at various points of a watershed's response to climate change.

4.7 Acknowledgments

Thank you to Mike Anderson and Randi Field for your insightful conversations regarding Lake Shasta and potential research directions. Chapter 4, in part, is currently being prepared for submission for publication of the material. Sierks, M., Dettinger, M., Chapman, W. E., Ralph, F. M. The dissertation author was the primary investigator and author of this paper.

Table. 4.1. The10 CMIP5 GCMs from which downscaled and bias-corrected projections were used in this study, and their originating institutions.

Model Acronym	Model Source/Institution
ACCESS1.0	Commonwealth Scientific and Industrial Research Organisation (CSIRO) and Bureau of Meteorology, Australia
CCSM4	National Center for Atmospheric Research (NCAR), United States NCAR, United States
CESM1-BGC	National Center for Atmospheric Research (NCAR), United States NCAR, United States
CMCC-CMS	Centro Euro-Mediterraneo per I Cambiamenti Climatici
CNRM-CM5	Centre National de Recherches Météorologiques, France
CanESM2	Canadian Centre for Climate Modelling and Analysis, Canada
GFDL-CM3	Geophysical Fluid Dynamics Laboratory (GFDL), Princeton, New Jersey, United States
HadGEM2-CC	Met Office Hadley Center, UK
HadGEM2-ES	Met Office Hadley Center, UK
MIROC5	Atmosphere and Ocean Research Institute and NIES, Japan

Table 4.2. Summary of Nash-Sutcliffe efficiency (NSE) and additional relevant statistics detailing model performance over the validation period (WYs 1996-2017) for both storage and outflow metrics. NSE values are denoted with an asterisk where the associated p-value is significant at the 1% level.

	Nash-Sutcliffe Efficiency (NSE)	Bias [TAF]	RMSE [TAF]
Daily Storage	0.90*	-19.1	269.9
Monthly Mean Storage	0.90*	-19.1	266.3
Water Year Mean Storage	0.84*	-19.1	230.1
Carryover Storage	0.78*	-8.3	326.3
Water Year Maximum Storage	0.87*	-57.3	225.2
Water Year Minimum Storage	0.80*	35.8	296.1
Daily Outflow	0.64*	0.1	8.3
Monthly Mean Outflow	0.89*	0.1	3.8
Water Year Mean Outflow	0.98*	0.1	0.7
October-April Mean Outflow	0.97*	0.2	1.5
May-September Mean Outflow	0.47*	-0.1	1.9

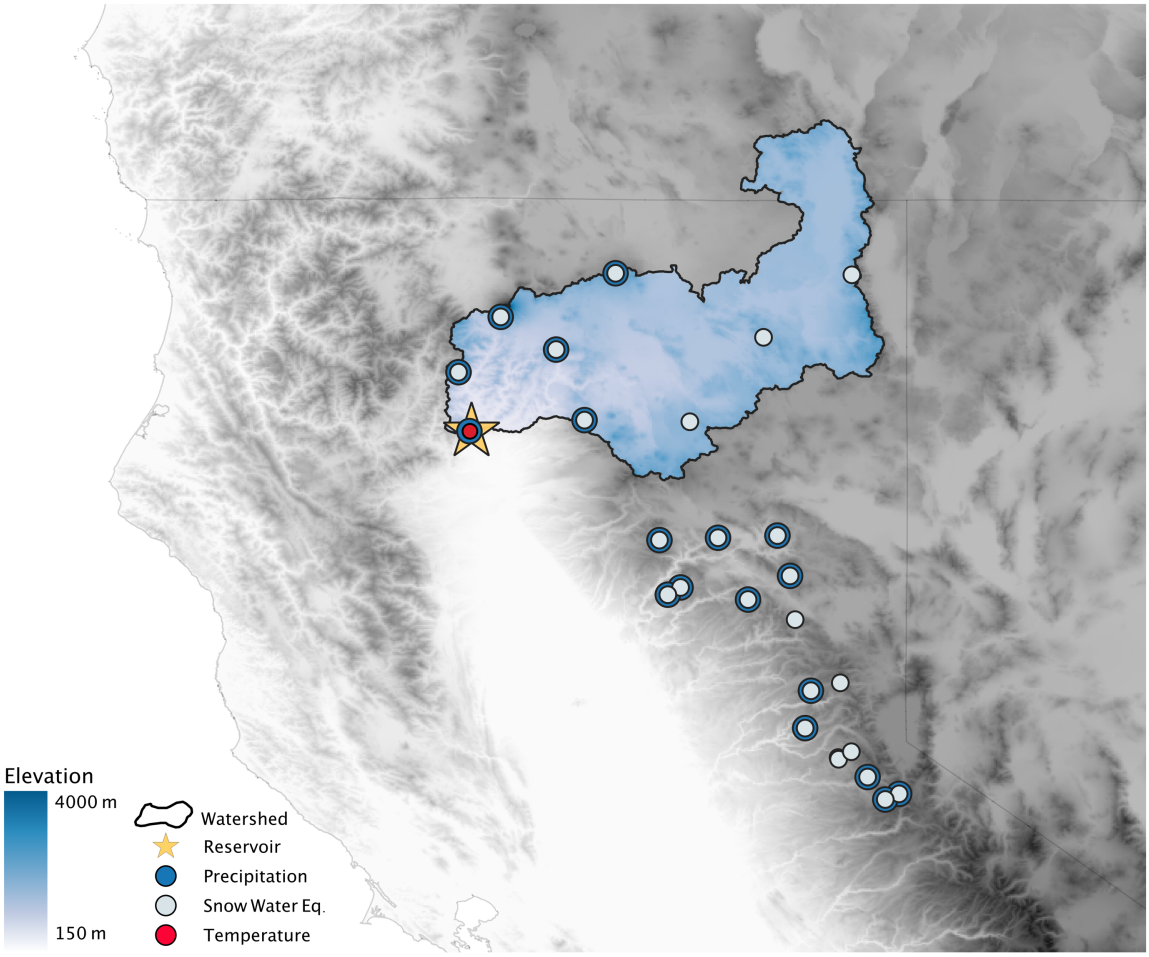

Figure 4.1. Map of study area showing the Lake Shasta watershed (black contour), elevation (color shade), and station location for observational data.

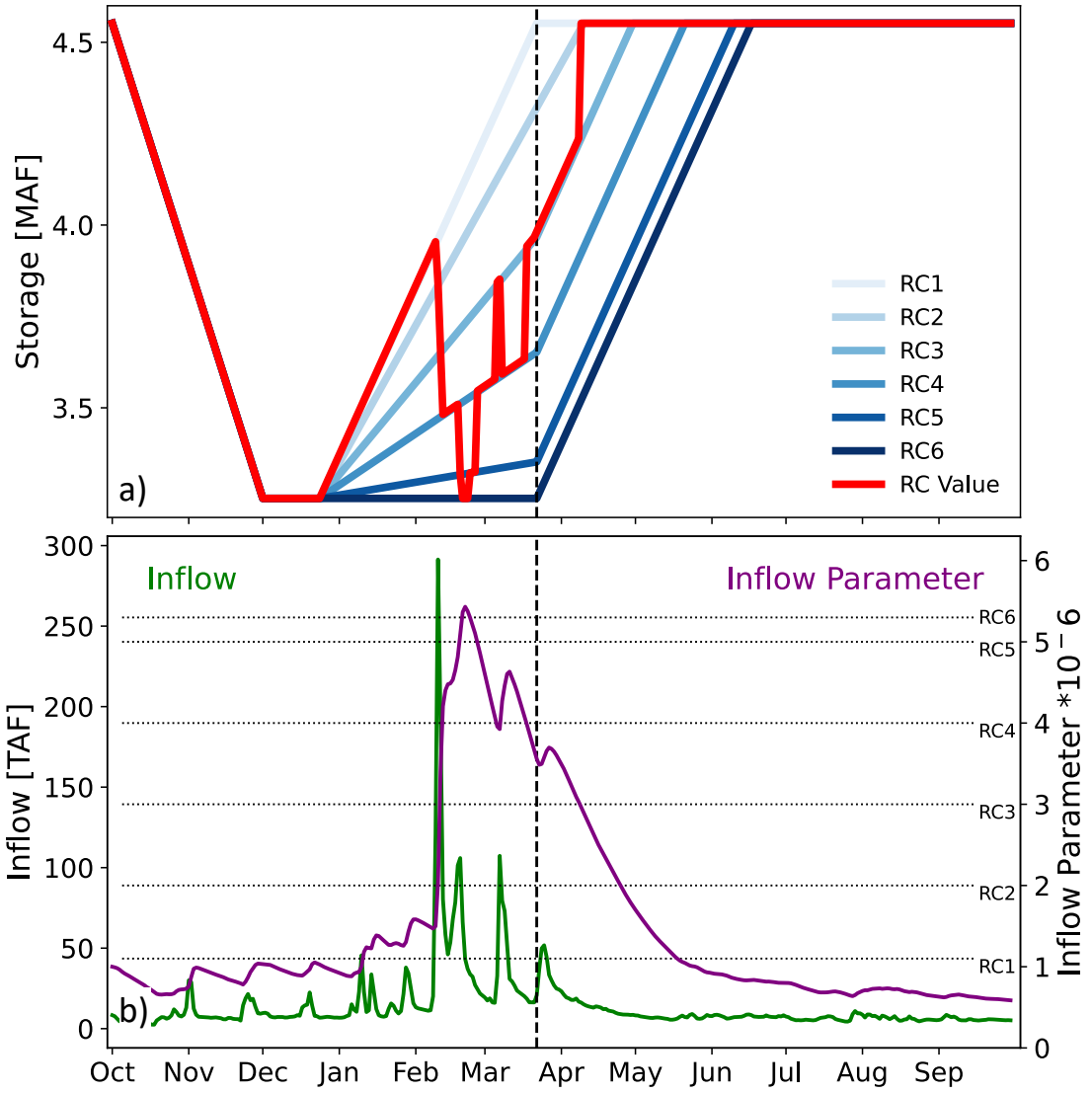

Figure 4.2. a) The maximum allowable storage behind the dam is governed by Shasta's rule curve, which mandate 1 of 6 possible sub-curves (blue shading) on each day of the water year depending on the inflow parameter that day. The enforced values (red) over the course of a hypothetical year are dictated by changes in the inflow parameter. The refill date (black dashed) is shown to highlight the shift in priorities from flood-risk mitigation to water supply. b) The corresponding timeseries of reservoir inflow (green) and inflow parameter (purple) are shown. Responding to changing reservoir inflow, if the inflow parameter rises above the threshold value associated with a sub-rule curve (dotted black lines), it triggers the 'activation' of said sub-rule curve (ex. RC6 becomes enforced during late February). When the inflow parameter falls below a threshold (ex. RC3 in early April), the subsequent sub-curve (in this case, RC2) becomes activated.

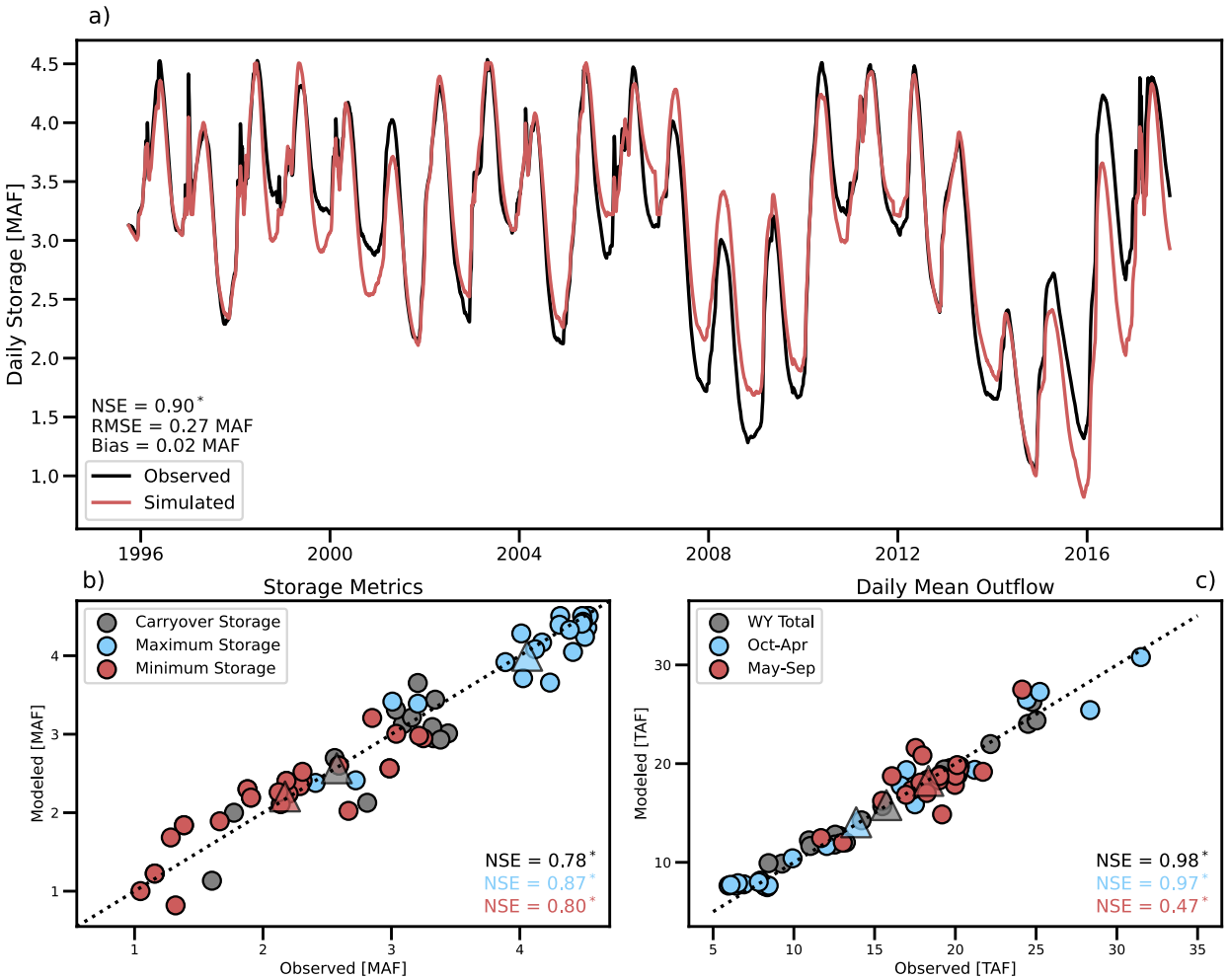

Figure 4.3. Model performance over the validation period (WYs 1996-2017); a) timeseries of observed (black) and simulated (red) daily reservoir storage, b) WY storage metrics, and c) daily outflow metrics. Performance is measured by Nash-Sutcliffe efficiency (NSE) and is denoted with an asterisk where the associated p-value is significant at the 1% level.

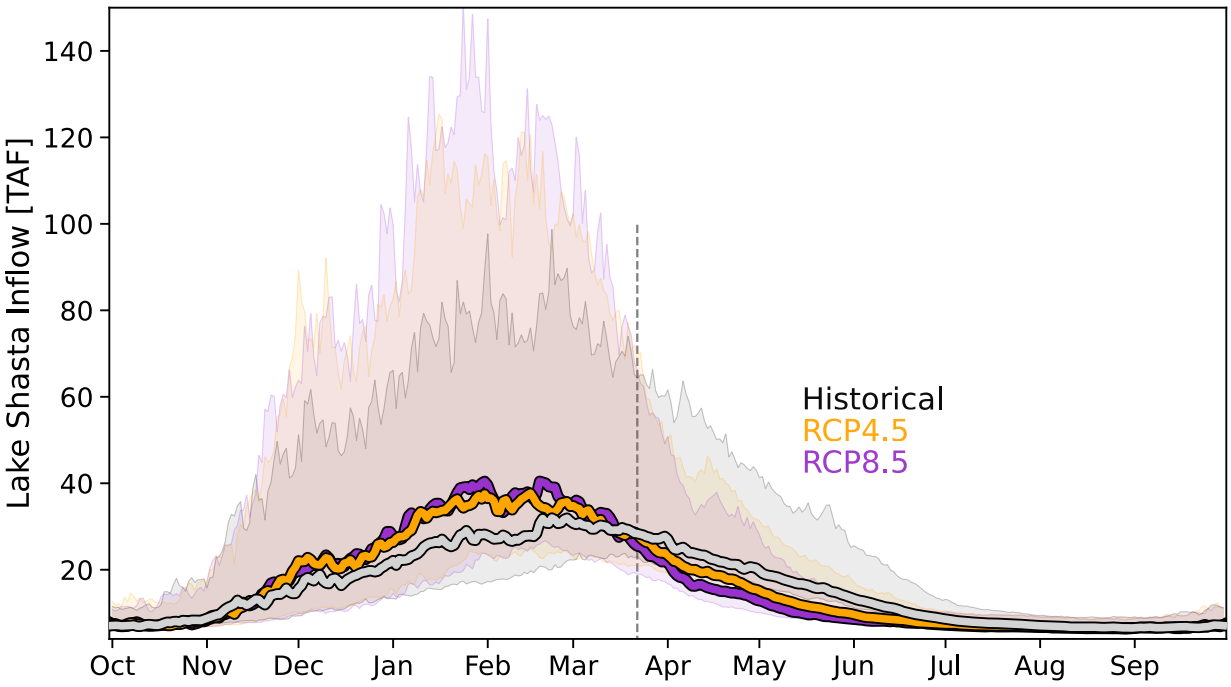

Figure 4.4. Lake Shasta inflow for the historical (grey, 1970-2020) and end of century (2050-2099) GCM periods for RCP4.5 (orange) and RCP8.5 (purple). Ensemble mean daily mean values averaged over the climatological era (solid lines) and 50th-95th percentile range (shading) are shown. Lake Shasta's refill date (March 20th) appears as a dashed vertical line.

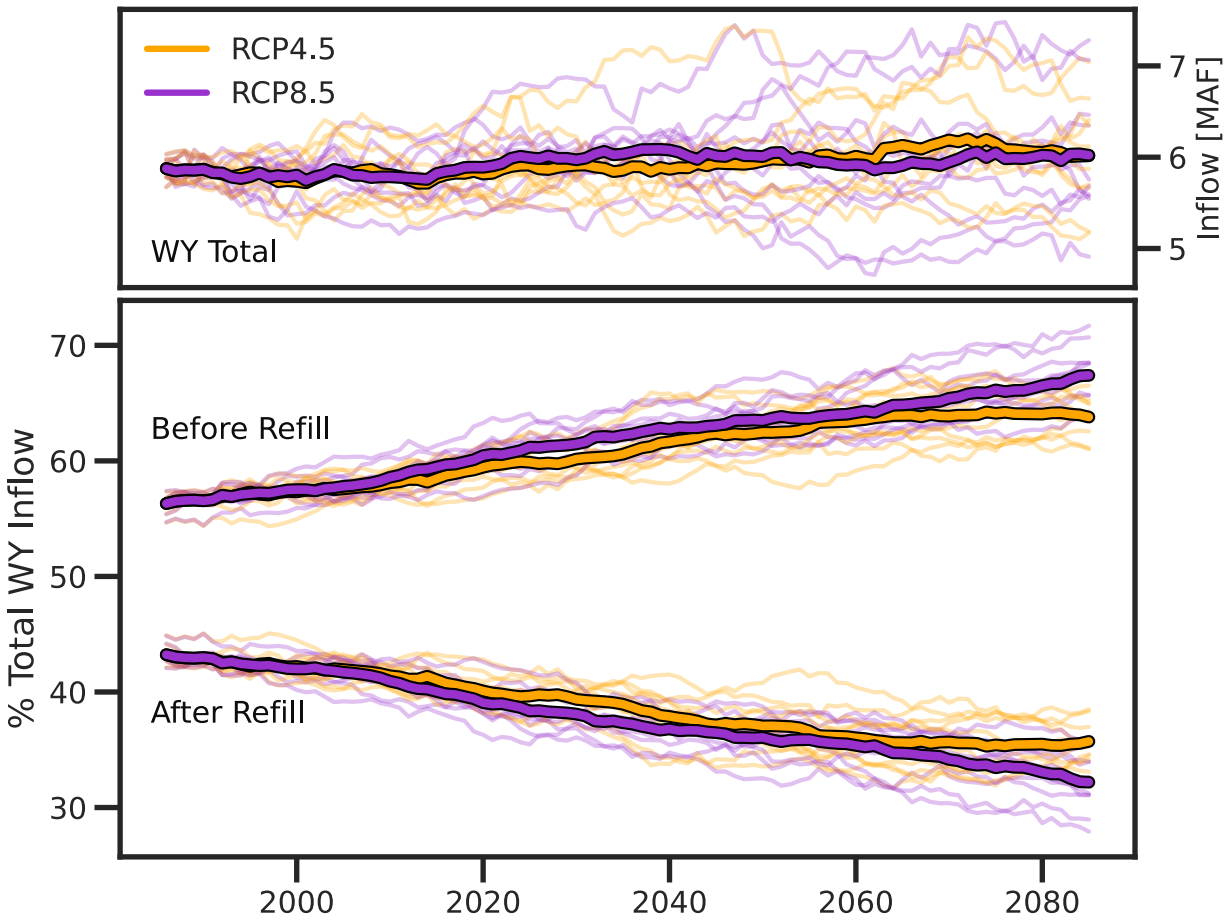

Figure 4.5. Centered 30-year averages of cumulative inflow over entire WY (top) and the percent of total WY inflow occurring before and after the reservoir refill date (March 20th, bottom). Ensemble mean (bolded lines) and individual GCMs (traces) are shown for RCP4.5 (orange) and RCP8.5 (purple) projections.

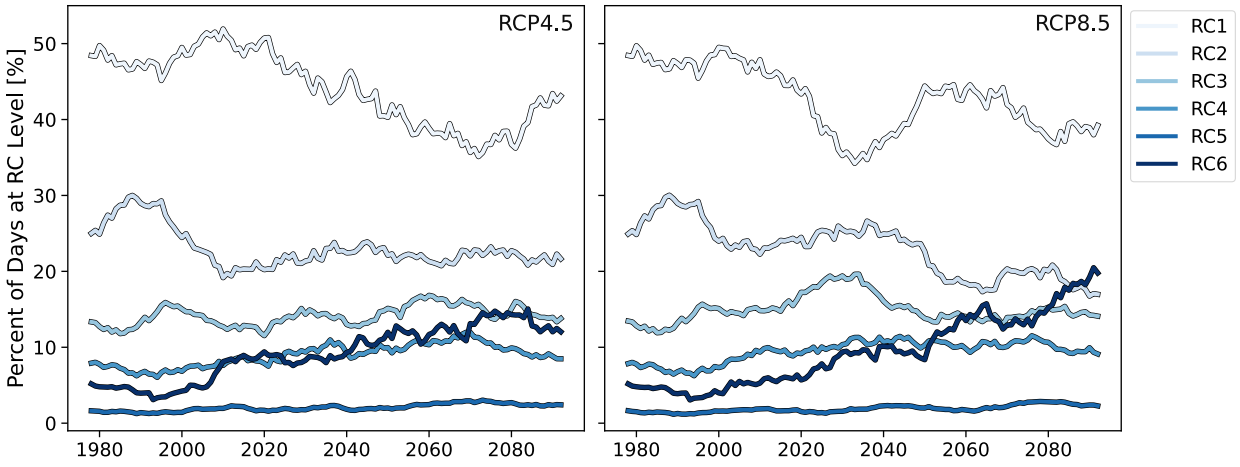

Figure 4.6. Ensemble mean centered 30-year averages of the percentage of days between December 23rd and March 20th that each of the 6 possible sub-rule curves is enforced. Sub-rule curves move from least-to-most restrictive with increasing color shade.

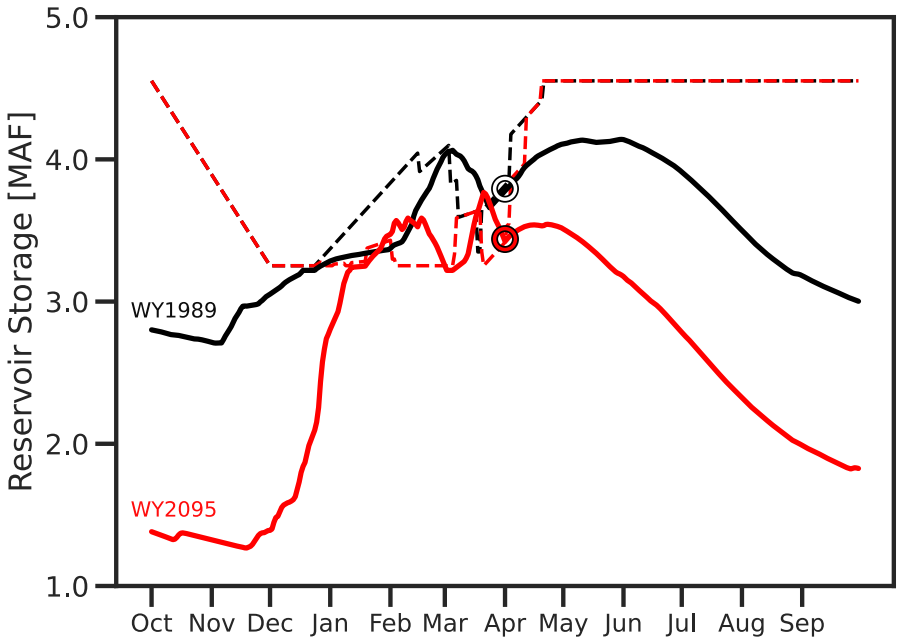

Figure 4.7. Timeseries of daily storage (solid) and operative rule curve (dashed) values for 2 individual water years in CCSM4. The date and associated storage value of the final flood-risk release of the year is marked with a circle.

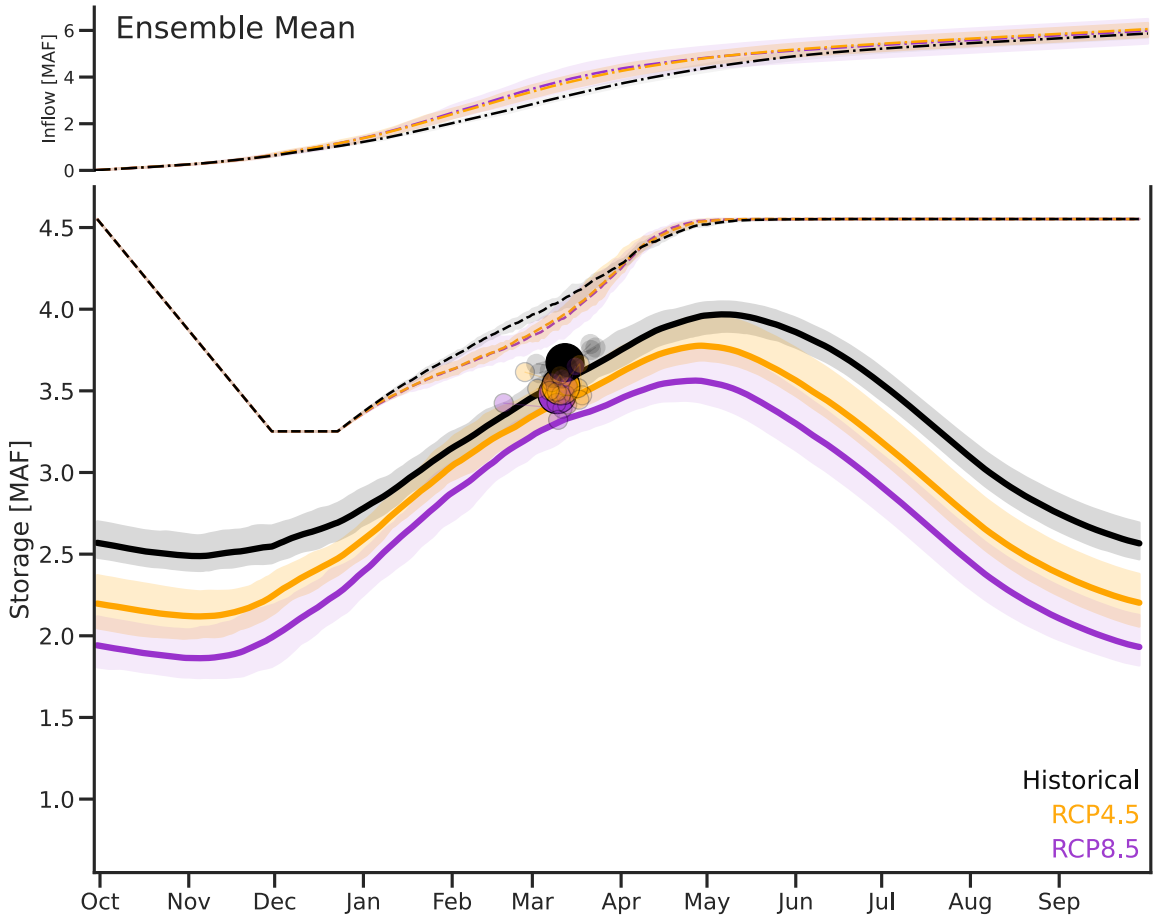

Figure 4.8. Averaged over each climatological era, ensemble mean values of daily mean cumulative inflow (top, dot-dashed), storage (center, solid), and the operative rule curve (center, dashed) are show. Shading represents the spread of daily mean values for the middle 6 GCMs for historical (black), RCP4.5 (orange) and RCP8.5 (purple) simulations. The average storage value and date associated with the final flood-risk release of a given water year (circles) is shown for the individual GCMs (small markers) and ensemble mean (large markers).

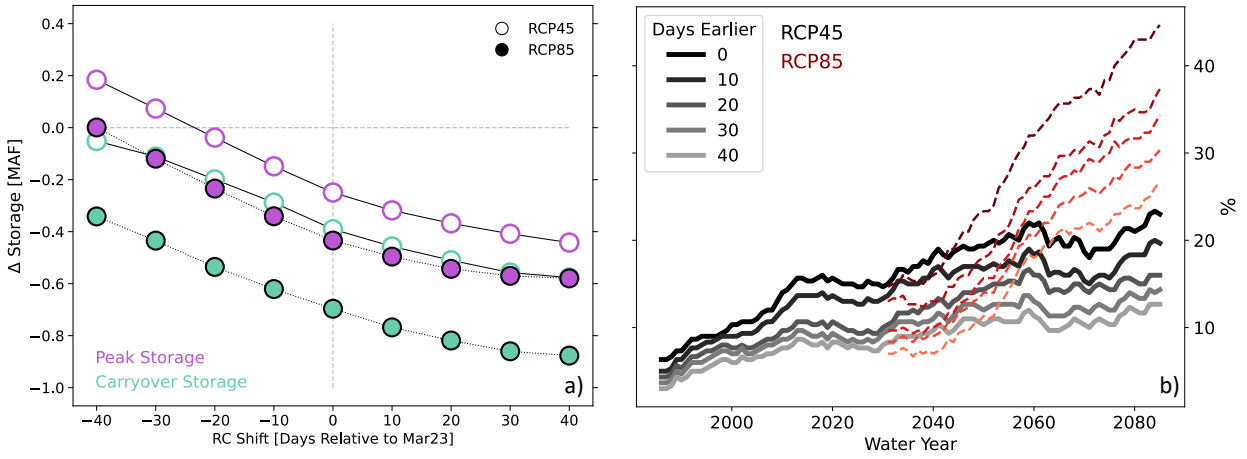

Figure 4.9. Ensemble mean water supply metrics of a) carryover and peak storage, and b) critically low storage levels, under adaptive operations in which the reservoir is allowed to begin refilling earlier or later. (a) 50-yr average difference in carryover (teal) and peak (pink) storage from historical levels (horizontal dashed line) under existing operations for RCP4.5 (hollow markers) and RCP8.5 (filled markers) scenarios. (b) Centered 30-year mean percent of ensemble members for which carryover storage falls below the 10th percentile of historical operations for RCP4.5 (grey solid lines) and RCP8.5 (red dashed lines) for experiments with earlier (only) refill dates. The lighter the curve the earlier the refill date with existing operations in black.

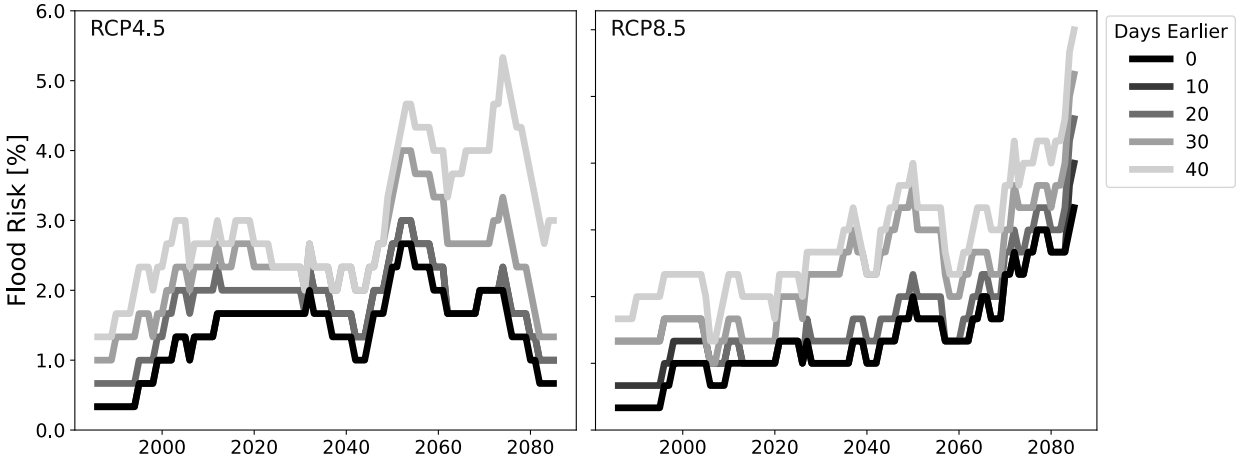

Figure 4.10. Centered 30-year mean values of flood risk as measured by the average percentage of ensemble members requiring a spillway release during a given water year for RCP4.5 (left panel) and RCP8.5 (right panel). The lighter the curve the earlier the refill date with existing operations (0-day earlier) in black.

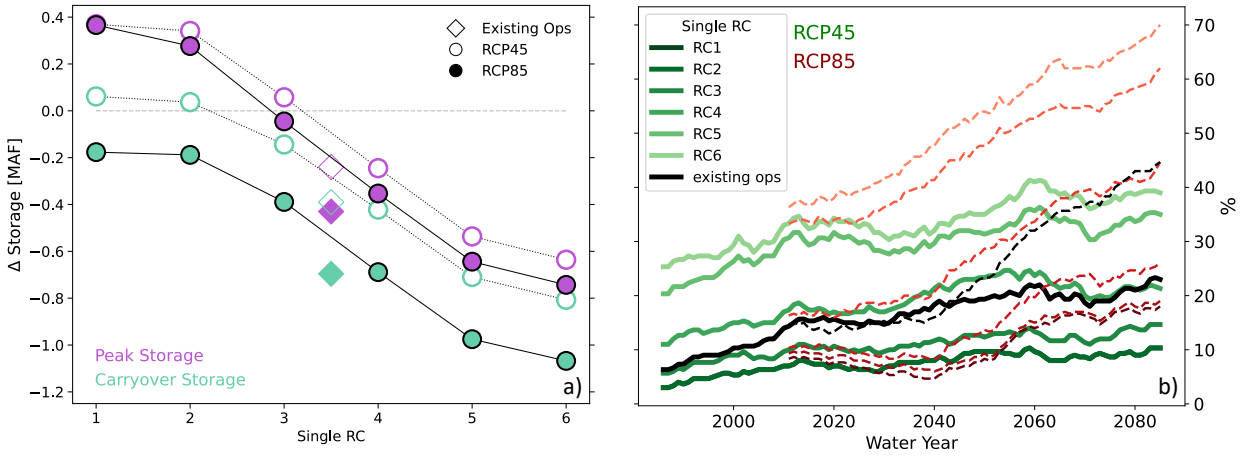

Figure 4.11. Water supply metrics of mean (a) and critically low (b) storage levels under adaptive operations in which the reservoir uses a fixed, rather than dynamic rule curve. (a) Difference in carryover (teal) and peak (pink) storage from historical levels under existing operations for RCP4.5 (hollow markers) and RCP8.5 (filled markers) scenarios. Adaptive simulations (circles) and existing operations (diamonds) are both shown. (b) Centered 30-year mean values of the fraction of ensemble members whose carryover storage falls below the 10th percentile of historical operations for RCP4.5 (green solid lines) and RCP8.5 (red dashed lines). Lighter shading corresponds to less restrictive rule curves with existing operations shown in black.

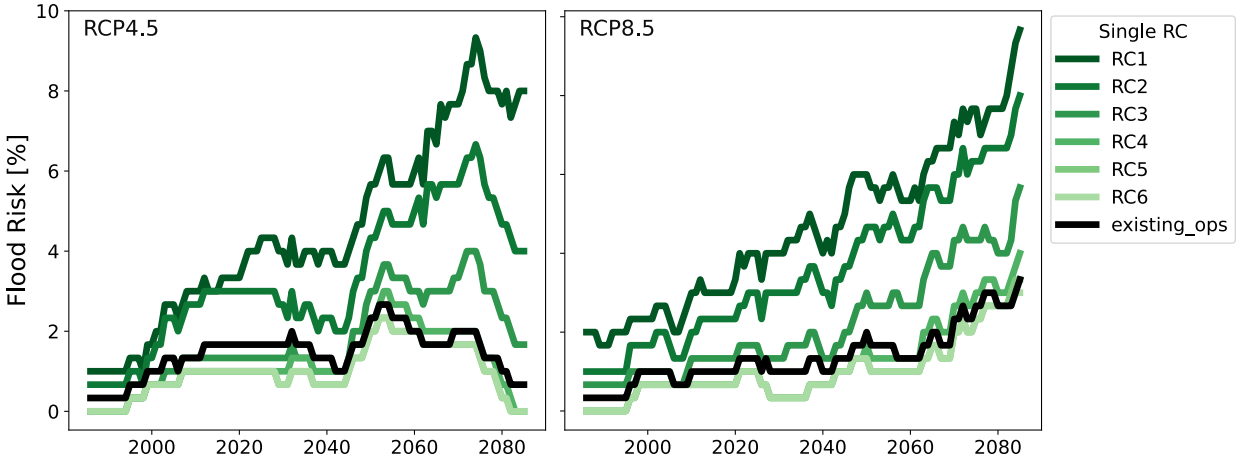

Figure 4.12. Centered 30-year mean values of flood risk as measured by the average percentage of ensemble members requiring a spillway release during a given water year for RCP4.5 (left panel) and RCP8.5 (right panel). Lighter line color corresponds to more restrictive sub-rule curves with existing operations (dynamic rule curve) in black.

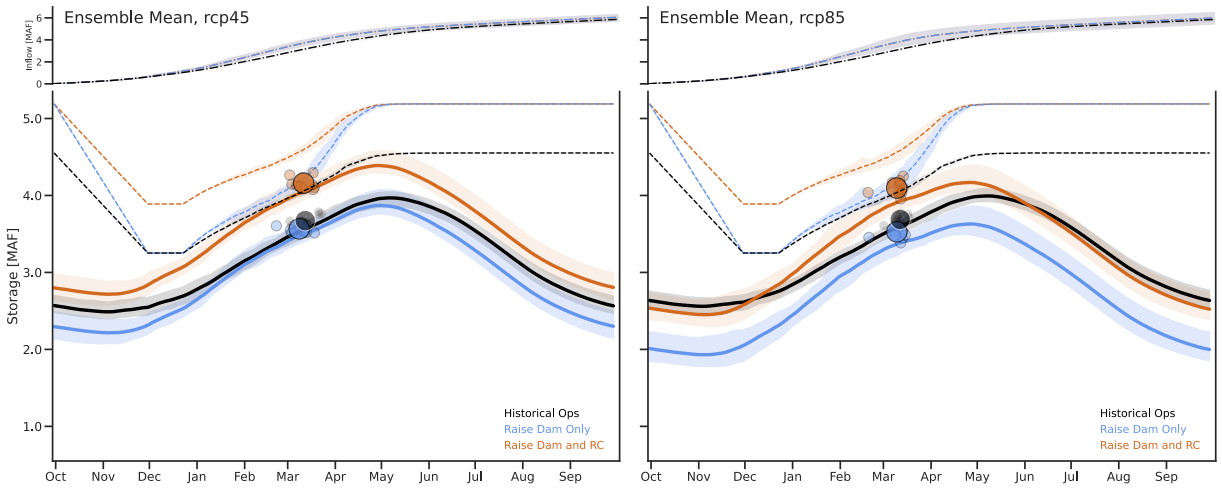

Figure 4.13. Averaged over each climatological era, ensemble mean values of daily mean cumulative inflow (top, dot-dashed), storage (center, solid), and the average operative rule curve (center, dashed) are show for historical (black), raised dam and rule curve (brown), and raised dam with increased flood-pool (blue) simulations under RCP4.5 (left panel) and RCP8.5 (right panel). Shading represents the spread of daily mean values for the middle 6 GCMs for each simulation. The average storage value and date associated with the final flood-risk release of a given water year (see Section 4.5.2 for context) is shown for the individual GCMs (small circles) and ensemble mean (large circles).

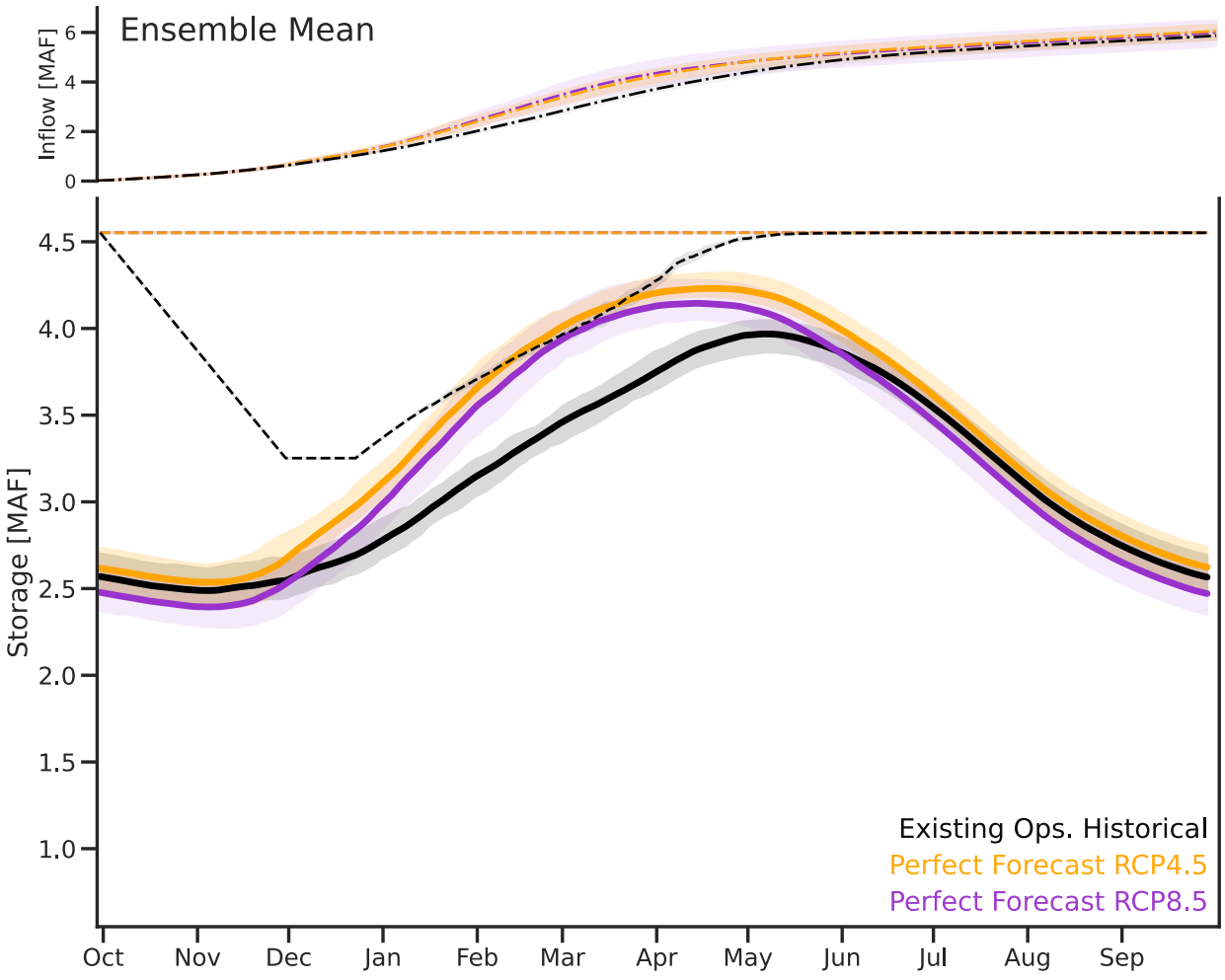

Figure 4.14. Averaged over each climatological era, ensemble mean values of daily mean cumulative inflow (top, dot-dashed), storage (center, solid), and the average operative rule curve (center, dashed) are show for existing operations over the historical period (black) and 7-day perfect forecast simulation under RCP4.5 (orange) and RCP8.5 (purple). Shading represents the spread of daily mean values for the middle 6 GCMs for each simulation.

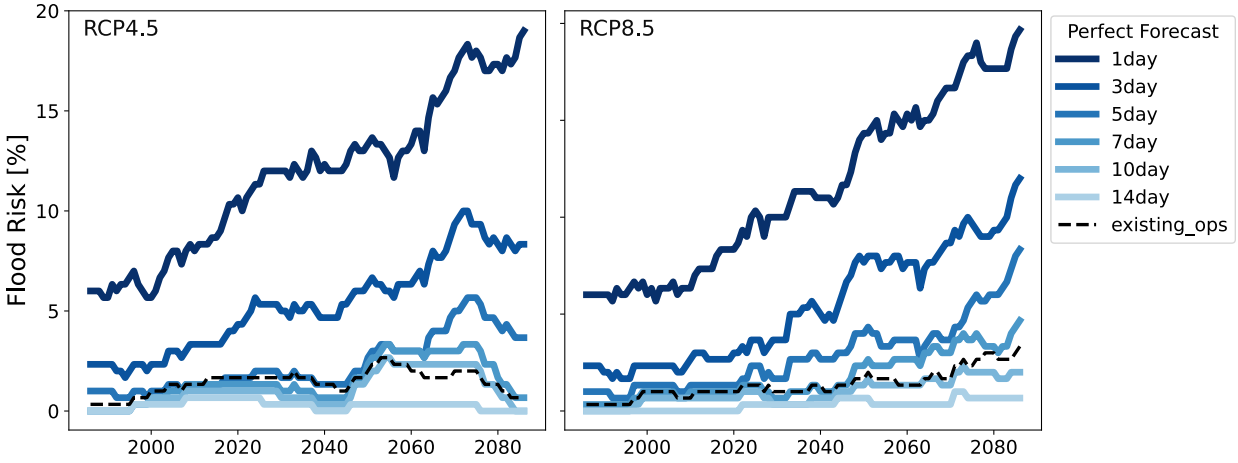

Figure 4.15. Centered 30-year mean values of flood risk as measured by the average percentage of ensemble members requiring a spillway release during a given water year for RCP4.5 (left panel) and RCP8.5 (right panel). Increasing perfect forecast horizons correspond to lighter blue curves with existing operations (black dashed) shown for context.

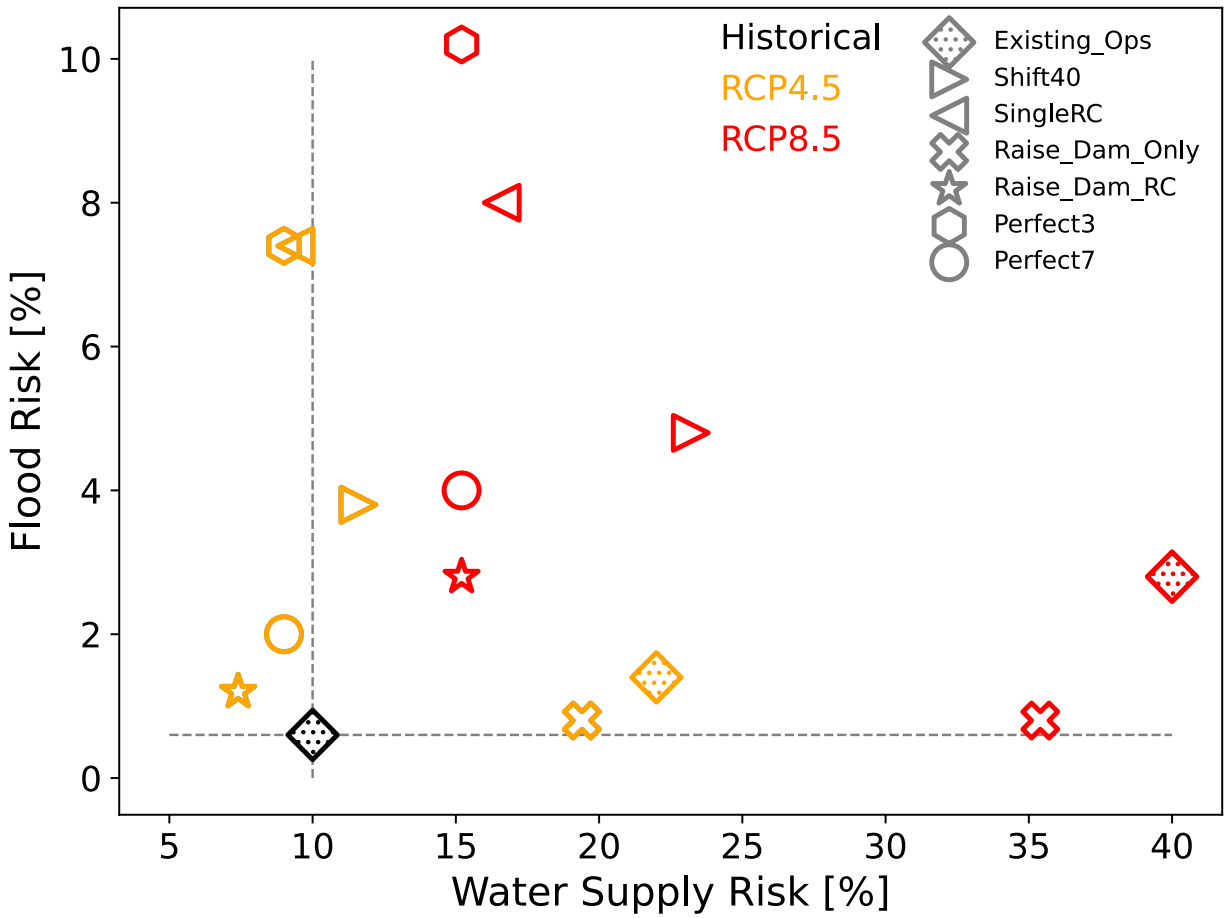

Figure 4.16. Scatterplot summarizing the risks to water supply and flood mitigation for historical (1970-2020, black marker), RCP4.5 (2050-2099, orange markers), and RCP8.5 (2050-2099, red markers) simulations. Flood-risk, evaluated as the mean percentage of ensemble members requiring a spillway release during a given water year averaged over the climatological era, is plotted on the y-axis. Water supply risk, evaluated as the mean percentage of ensemble members whose carryover storage falls below the 10^{th} percentile of historical operations averaged over the climatological era, plotted on the x-axis. Marker type signifies a particular adaptation experiment with existing operations (diamond marker) shown for context.

4.8 Supplementary Materials

4.8.1 Variable Rule Curve

The operational rule curve (RC) for Lake Shasta does not have a fixed value for each day of the water year. Instead, from December 23rd through June 15th, the maximum allowable storage volume is selected from one of six possible sub-rule curves (US. Army Corps of Engineers, 1977). A nondimensional quantity, the Inflow Parameter, also referred to as the ground-wetness parameter, is calculated daily to decide which of the six possible sub-RCs is enforced. On October 1st, at the start of each water year, the Inflow Parameter is set to a value of 100,000. Restated here from Eq. 4.1 in the main text,

$$\boldsymbol{Inflow\ Parameter_i} = (\mathbf{0.95} * \boldsymbol{Inflow\ Parameter_{i-1}}) + \boldsymbol{Inflow_i}$$

where i represents a given day. The parameter is not based entirely on given day's inflow. The first term on the left-hand side acts as a memory term, carrying information from recent days. In practice, the reservoir maintains a larger flood pool when the inflow parameter is large, and favors building water supply when the value is small. Table 4.1S outlines the parameter values associated with each rule curve and is adapted from US ACE Chart A-8 (US. Army Corps of Engineers, 1977).

Table 4.1S. Associated Inflow Parameter value for each of the 6 sub-rule curves governing Lake Shasta's operational rule curve. Table recreated from data appearing in US ACE Chart A-8 (US. Army Corps of Engineers, 1977).

Sub-Rule Curve	Parameter Value Range
1	0-200,000
2	200,000-300,000
3	300,000-400,000
4	400,000-500,000
5	500,000-530,000
6	530,000+

4.8.2 Simulated Wet-Season Operations

From October through April, simulated releases are calculated in one of two scenarios: 1) storage value exceeds the RC, 2) storage value is below the RC.

4.8.2.1 Storage Exceeds the Rule Curve

To determine if storage will increase above the RC, the 24-hour inflow volume is added to the storage from the previous day, assuming no releases or evaporative losses on the current day. If this volume exceeds the RC for that day (i.e. if $Storage_{i-1} + Inflow_i > RC_i$), US ACE Chart A-8 is used to determine the appropriate release given the flood risk (US. Army Corps of Engineers, 1977). The release is based on the magnitude of the inflow and the percentage of the flood-pool currently available. The release schedule from the US ACE Chart A-8 is used except when releases are governed by the emergency spillway diagram, discussed below.

In rare cases when the reservoir stage is rising and there is risk of uncontrolled releases, US ACE Chart A-9 is enforced (US. Army Corps of Engineers, 1977). Under normal conditions, the maximum release from Shasta is 79,000 CFS, however, the spillway diagram can dictate a maximum release of 320,000 CFS, which carries great risk, though less than uncontrolled spill

over the top of the dam. Our model abides by the rules directly and will use the spillway diagram as detailed in US ACE Chart A-9 (US. Army Corps of Engineers, 1977).

4.8.2.2 Storage Below the Rule Curve

Absent flood risk, the model makes a climatological release during the wet season. Climatological releases are computed in the following manner. First, to smooth any RC releases, a centered 30-day rolling mean is applied to the daily outflow timeseries. Next, the data is subset by taking the 30 days on either side of the given model day across all available data (n=21 years). Using a bin size of 100 CFS, we sort the subset data and take the first 'm' bin values that compose 50% of the cumulative distribution. Next, we create a new synthetic distribution composed of 100 random draws with replacements from these 'm' values and randomly select a single value as the outflow for the given model day.

4.8.3 Simulated Dry-Season Operations

From May 1st though the end of the water year, absent any RC required releases, we base the daily outflow on the predicted total volume of water to be released during May-September. Because this period coincides with high demand, low inflows, and environmental requirements, this process is more complex than the climatological release described above. Motivated by the fact that outflows are related to the Sacramento Valley water year index (WYI), a nondimensional variable used by the California DWR as a proxy for how much runoff occurs in the Sacramento basin during a given year, our warm season outflow prediction relies on the WYI.

The CA DWR calculates the WYI in their Bulletin-120 (B120) through the following equation,

$$\boldsymbol{WYI_i = 0.4 * Q_{Apr-Jul\,fcst} + 0.3 * Q_{Oct-Mar} + 0.3 * WYI_{i-1}}$$

where $\boldsymbol{i}$ represents a given year and $\boldsymbol{Q}$ is streamflow. The first term represents the forecasted total streamflow volume for April-July and, the second term is the observed streamflow volume from October-March, and the final term is the value of the previous water year index. Here, we describe how we predict the WYI value each year using water year-to-date (WYTD) precipitation, snow water equivalent (SWE), and Shasta inflow on April 1st. Since the Sacramento Valley, for which the WYI is calculated, encompasses a greater area than just the Lake Shasta watershed, we compute basin-wide averages of precipitation and SWE for the Shasta, Feather, and Yuba-American watersheds. The area-average is composed of data from individual stations represented on Figure 4.1 of the main text. The names and locations of these stations are given below in Section 4.8.6.

To compute the WYI, first, the raw values of April 1st data of basin-average SWE for the Shasta, Feather, and Yuba American watersheds, April 1st data of basin-average precipitation for the Shasta, Feather, and Yuba American watersheds, rolling 3-yr averages of April 1st data of basin-average precipitation for the Shasta, Feather, and Yuba American watersheds, and October-April cumulative inflow are converted to Z-scores. We then conduct principal component analysis (PCA) on the normalized data. All 10 principal components are used to learn coefficients in our multi-linear regression model which predicts the final WYI value (see the concluding paragraph in section 4.8.3 for commentary on how the approach differs for the calibration/validation era and the simulated climate runs).

To predict the total May-September reservoir outflow, we first conduct PCA using normalized values of WYI, cumulative April 1st precipitation in the Shasta basin, and cumulative

April 1st reservoir inflows. All 3 principal components are used as training data to learn coefficients in our multi-linear regression model which calculates the total dry-season reservoir outflow volume. Under the special scenario called a "Shasta Critical" year, wherein inflow deficits over a given water year or successive water years exceeds a threshold set by the Bureau of Reclamation, deliveries can be reduced by 25% (Section 4.4, U.S. Bureau of Reclamation, 2019). If these conditions are met for a given WY, we reduce the projected total May-September outflow volume by 25%. To determine the daily release, we multiply the total seasonal outflow by the climatological percentage (calculated over the historical record) of total May-September releases made on a given day.

As described in the main text, for a given WY during the validation period, we predict a given WYI and summer release volume excluding data from the water year being simulated (a N-year cross-validation procedure). This is done to ensure that the model is not overfit on the current data and generalizes well to data that it is not trained on. Prior to running the GCM simulations, we use all data from the validation period to compute the linear regression coefficients (generated through the PCA) which are then used to simulate the reservoir operations driven by GCM inflows.

4.8.4 Estimation of Daily Evaporation

At each timestep in the model simulation, we estimate the value of evaporative loss through multi-linear regression using temperature and storage data. For a given WY during the calibration/validation period, we again predict daily evaporation using only data from the other WYs. In practice, normalized daily temperature and storage data are used to learn coefficients in our multi-linear regression model which predicts daily evaporative loss. Prior to running the GCM simulations, we use all data from the validation period to compute the linear regression coefficients which are then used to simulate daily evaporative losses driven by GCM temperature.

4.8.5 Downscaling GCM Data Using Station Data

4.8.5.1 Station-to-Gridded Data

When model coefficients learned over the calibration/validation period are applied to projected climate runs, the result simulations are be sensitive to differences in the distributions of relevant hydroclimate variables (precipitation, SWE) between the historical model period (1970-2005) and the model calibration/validation period (1996-2017). As a result, we incorporate a step called secondary bias correction in which data (already having undergone bias correction) are bias corrected again to remove systematic biases between some historical dataset (observed or reanalysis) and the pre-warming model data. Ideally, CDEC station data would be used for this purpose. However, bias correction is more robust with at least 30-years of data and the calibration/validation period only covers 1996-2017. To ensure that we have a consistent dataset used in both the calibration/validation and projected climate simulations, we leverage a combination of reanalysis and observational data to create a final dataset that both 1) has a period of record long enough to be used for bias correcting the model data (30 yrs), and 2) covers the period of record used in the calibration/validation step. This process is described below and is done for April 1st values of precipitation and SWE at the stations listed in Section 4.8.6.

We choose to build this dataset from Livneh reanalysis (Livneh et al., 2013) because it has a long record (1950-2005) and is widely used in the community. Because it does not cover the calibration/validation period, we extend it by building statistical relationships, through linear regression, between overlapping years of data between the Livneh and PRISM (Daly et al., 1994) (for precipitation) and Broxton et al (2019) (for SWE). Then, to better account for biases between the gridded reanalysis (6-km resolution) and station data, we again use linear regression to transform the station data to better fit the Livneh distribution at each station. The resulting

dataset is one that covers both the calibration/validation period and has a sufficient historical record to be used to bias correct the projected climate data.

4.8.5.2 Secondary Bias Correction

As described above, secondary bias correction is used to ensure the distributions of pre-warming data used in model parameters are identical to the calibration/validation data. To ensure that any changes in simulated reservoir performance under future climate are due to relative changes between the historical and future model runs, and not differences between the mean statistics of the calibration/validation and GCM data, we employ the PresRat method (Pierce et al., 2015). PresRat is an extension of quantile mapping proven to better ensure that the signal the model data is altered to a lesser extent by the bias correction process than other commonly employed practices (Pierce et al., 2015) such as quantile mapping (Panofsky & Brier, 1968; Wood et al., 2002) or CDF-transform (Michelangeli et al., 2009).

4.8.6 Station Data Information

4.8.6.1 CDEC Rainfall Stations

Table 4.2S. Station information for all CDEC rainfall data used to calculate watershed average values.

Station Abbreviation	Longitude	Longitude
SHA	40.71	-122.42
SDF	41.35	-122.24
MED	41.59	-121.61
SNM	40.77	-121.78
SLT	41.04	-122.48
STM	41.16	-121.93
BKL	39.85	-121.25
FOR	39.81	-121.32
GRZ	39.91	-120.64
HMB	40.11	-121.36
PLP	39.78	-120.87
RTL	40.12	-121.04
KTL	40.14	-120.71
CAP	38.71	-120.04
FRN	38.80	-120.21
GKS	39.07	-120.56
HYS	39.28	-120.52
SIL	38.67	-120.11

4.8.6.2 CDEC SWE Stations

Table 4.3S. Station information for all CDEC SWE data used to calculate watershed average values.

Station Abbreviation	Latitude	Longitude
ADM	41.23	-120.79
BLA	40.76	-121.19
CDP	41.58	-120.30
SDF	41.35	-122.24
MED	41.59	-121.61
SNM	40.77	-121.78
SLT	41.04	-122.48
STM	41.16	-121.93
BKL	39.85	-121.25
GOL	39.67	-120.61
FOR	39.81	-121.32
GRZ	39.91	-120.64
HMB	40.11	-121.36
PLP	39.78	-120.87
RTL	40.12	-121.04
KTL	40.14	-120.71
ALP	38.80	-120.21
CAP	38.71	-120.04
CSL	39.32	-120.36
FRN	38.80	-120.21
GKS	39.07	-120.56
HYS	39.28	-120.52
RBB	38.91	-120.37
RBP	38.90	-120.37
SIL	38.67	-120.11
VVL	38.94	-120.30

4.8.6.3 CDEC Temperature Stations

Table 4.4S. Station information for all CDEC temperature data used to estimate evaporation values.

Station Abbreviation	Latitude	Longitude
SHS	40.71	-122.41

4.8.6.4 CDEC Reservoir Inflow Stations

Table 4.5S. Station information for all CDEC reservoir inflow data.

Station Abbreviation	Longitude	Longitude
SHA	40.71	-122.42

Chapter 5

Conclusion

5.1 Summary of Major Contributions

Through the development of novel statistical methods and modeling, this dissertation leverages a combination of historical weather station observations, atmospheric reanalysis products, and future climate simulations to evaluate the impacts of extreme precipitation and potential impacts of climate change on the vulnerable water resources of the southwestern United States. The second chapter focuses on the North American Monsoon (NAM) region over the historical record to examine the atmospheric forcing of large storm events. The subsequent two chapters shift their attention to examining future climate projections from global climate models (GCMs) for the northern California region and how such changes in precipitation, snowpack, and streamflow may impact reservoir operations.

In Chapter 2, we present a climatological characterization of summertime precipitation, defined as July, August, and September (JAS), in the Lake Mead watershed, located on the periphery of the NAM region, and detail the importance of extreme events through both composite and individual event analysis of the synoptic environment. In contrast to the core NAM region to the south, where easterly upper-level disturbances such as inverted troughs are the dominant driver of extreme precipitation, Chapter 2 finds anticyclonic Rossby wave breaking (RWB) in the midlatitude westerlies over the US west coast are associated with 89% of precipitation events >10 mm (98^{th} percentile of wet days) over the Lake Mead basin. Due to the synoptic nature of RWB events, corresponding impacts and hazards extend beyond the Lake Mead watershed and are relevant for the greater U.S. southwest.

Motivated by a desire to connect bias correction techniques to the underlying dynamics within earth systems models, in Chapter 3, a novel statistical method is developed for projected streamflow wherein data are windowed based on hydrograph-relative time, rather than Julian day. Four existing bias correction methods, each using both the standard day-of-year and novel 'seasonally aware' windowing approaches, are applied to daily streamflow projections driven by climate simulations from 10 GCMs across a characteristically-diverse subset of six watersheds in California. The resulting bias corrected time series are evaluated to determine how the methods alter the original model climate change signal. We find the novel method, when compared with the others, better preserves the original simulated climate change signal. These improvements are realized in the water year mean signal, which is important as it relates to the total volume of water flowing through the river over the course of the year. Crucially, though, improvements are also realized for both low and high streamflow events which have an outsized imprint on California's hydroclimate, water resources, and ecosystems.

In Chapter 4, we develop a highly flexible model of California's largest reservoir, Lake Shasta, to analyze simulated future threats to water supply. The model simulates reservoir operations on a daily timestep and accounts for both flood-risk mitigation and water supply objectives. During the wet season, the model operates under a complex set of rules, as laid out by real-life dam operators, to prioritize the mitigation of flood risk. During the dry (demand) season, the model estimates water deliveries based on forecasted warm-season streamflow volume, informed by springtime snowpack data. Calibrated and validated over the historical record, the model simulates daily storage accurately enough for the purposes of exploring climate change impacts and adaptations. Using the bias corrected streamflow data from Chapter 3, we investigate projected climate change impacts on Lake Shasta operations under both existing and simplified

adaptation strategies. Compared to the historical period, we simulate 27% declines in carryover storage at the end of the 21st century under more extreme climate-changed scenarios and if operations are left unchanged. While a majority of storage loss is attributed to decreased snowpack, we find that existing reservoir operating procedures under the changed climates is responsible for one-third of the losses. Next, we explore the efficacy of both operational and infrastructural adaptation measures including altering the flood-control rule curves and increasing reservoir storage capacity. Despite application of many different interventions designed to recover historical levels of water supply over management of the enhanced future flood risks, historical levels of carryover storage were irretrievable at the end of the century under the more extreme levels of climate change.

5.2 Directions for Future and Related Research

While this dissertation strives to answer fundamental questions about the drivers of warm season extreme precipitation and projected future changes in California's water resources, there are several unanswered questions that can be the focus of future research. Within the scope of Chapter 2, after identifying the importance of Rossby wave breaking (RWB)in driving extreme warm season precipitation in the Lake Mead area, additional research should explore how frequently this RWB occurs over the US west coast and whether all RWB events cause precipitation. Further, due to their impact on the region, it would be interesting to examine whether and how the number of summertime RWB events changes under global warming scenarios.

After demonstrating, in Chapter 3, the improved ability of the 'seasonally aware' bias correction technique to preserve climate model signals, it would be useful to expand the dataset to a wider range of streams across California and to rivers across the west more broadly. Bias corrected simulations of future climate streamflow at important rivers could be useful for many

applications in this water-supply challenged region. Additionally, an important next step would be to evaluate the method for snow water equivalent (SWE) data as projections of snow are also characterized by changes in magnitude and seasonality.

Several directions for future work could build upon the results of Chapter 4 to increase their utility. Given that no one of the adaptation measures managed to undo the loss of historical storage levels, combinations of the several adaptation approaches need to be explored. Further, an assessment of existing inflow-forecast skill at Lake Shasta will be needed to determine the actual potential of adaptations based on forecast-informed operations, whereas here only a very idealized version of forecast-informed operations was explored. Both areas of research should be of interest to the water resources community that is going to be tasked with adapting operational strategies to a changing climate in the real world. Lastly, the model developed in this study has the potential to be augmented to investigate reservoir dependent processes such as the projected impacts of climate change on hydropower generation at Lake Shasta or important environmental/ecosystem variables such as stream temperature in the Sacramento River.

Chapter 6

References

Abatzoglou, J. T. (2016). Contribution of Cutoff Lows to Precipitation across the United States. *Journal of Applied Meteorology and Climatology*, *55*(4), 893–899. https://doi.org/10.1175/JAMC-D-15-0255.1

Abatzoglou, J. T., & Magnusdottir, G. (2006). Planetary wave breaking and nonlinear reflection: Seasonal cycle and interannual variability. *Journal of Climate*. https://doi.org/10.1175/JCLI3968.1

Adams, D. K., & Comrie, A. C. (1997). The North American Monsoon. *Bulletin of the American Meteorological Society*, *78*(10), 2197–2213. https://doi.org/10.1175/1520-0477(1997)078<2197:TNAM>2.0.CO;2

Baray, J. ., Baldy, S., Diab, R. ., & Cammas, J. . (2003). Dynamical study of a tropical cut-off low over South Africa, and its impact on tropospheric ozone. *Atmospheric Environment*, *37*(11), 1475–1488. https://doi.org/10.1016/S1352-2310(02)00999-8

Barnes, E. A., & Hartmann, D. L. (2012). Detection of Rossby wave breaking and its response to shifts of the midlatitude jet with climate change. *Journal of Geophysical Research Atmospheres*, *117*(9), 1–17. https://doi.org/10.1029/2012JD017469

Barnett, T. P., & Pierce, D. W. (2009). Sustainable water deliveries from the Colorado River in a changing climate. *Proceedings of the National Academy of Sciences of the United States of America*, *106*(18), 7334–7338. https://doi.org/10.1073/pnas.0812762106

Barnett, T. P., Pierce, D. W., Hidalgo, H. G., Bonfils, C., Santer, B. D., Das, T., … Dettinger, M. D. (2008). Human-Induced Changes United States. *Science*, *319*(February), 1080–1083.

Berg, N., & Hall, A. (2017). Anthropogenic warming impacts on California snowpack during drought. *Geophysical Research Letters*, *44*(5), 2511–2518. https://doi.org/10.1002/2016GL072104

Bieda, S. W., Castro, C. L., Mullen, S. L., Comrie, A. C., & Pytlak, E. (2009). The Relationship of Transient Upper-Level Troughs to Variability of the North American Monsoon System. *Journal of Climate*, *22*(15), 4213–4227. https://doi.org/10.1175/2009JCLI2487.1

Brazel, A. J., & Nickling, W. G. (1986). The relationship of weather types to dust storm generation in Arizona (1965-1980). *Journal of Climatology*, *6*(3), 255–275. https://doi.org/10.1002/joc.3370060303

Brekke, L. D., Maurer, E. P., Anderson, J. D., Dettinger, M. D., Townsley, E. S., Harrison, A., & Pruitt, T. (2009). Assessing reservoir operations risk under climate change. *Water Resources Research*, *45*(4), 1–16. https://doi.org/10.1029/2008WR006941

Brenner, I. S. (1974). A Surge of Maritime Tropical Air—Gulf of California to the Southwestern United States. *Monthly Weather Review*, *102*(5), 375–389. https://doi.org/10.1175/1520-0493(1974)102<0375:ASOMTA>2.0.CO;2

Brown, C., Ghile, Y., Laverty, M., & Li, K. (2012). Decision scaling: Linking bottom-up vulnerability analysis with climate projections in the water sector. *Water Resources Research*, *48*(9), 1–12. https://doi.org/10.1029/2011WR011212

Broxton, P., X. Zeng, and N. Dawson. 2019. Daily 4 km Gridded SWE and Snow Depth from Assimilated In-Situ and Modeled Data over the Conterminous US, Version 1. Boulder, Colorado USA. NASA National Snow and Ice Data Center Distributed Active Archive Center. https://doi.org/10.5067/0GGPB220EX6A. [Accessed December 2019]

Bunk, D. (2018). Colorado River Basin : System Status Update and Outlook for 2018 and 2019. *Colorado River Citizens Forum in Yuma, Arizona*, 15. U.S. Department of the Interior Bureau of Reclamation.

California Department of Water Resources Climate Change Technical Advisory Group. (2015). *Perspectives and Guidance for Climate Change Analysis*. Retrieved from http://www.water.ca.gov/climatechange/docs/2015/Perspectives_Guidance_Climate_Change_Analysis.pdf

Cannon, S. H., Boldt, E. M., Laber, J. L., Kean, J. W., & Staley, D. M. (2011). Rainfall intensity-duration thresholds for postfire debris-flow emergency-response planning. *Natural Hazards*, *59*(1), 209–236. https://doi.org/10.1007/s11069-011-9747-2

Carleton, A. M. (1986). Synoptic-dynamic character of 'bursts' and 'breaks' in the South-West U.S. summer precipitation singularity. *Journal of Climatology*, *6*(6), 605–623. https://doi.org/10.1002/joc.3370060604

Carleton, A. M. (1987). Summer Circulation Climate of the American Southwest , 1945-1984. *Annals of the Association of American Geographers*, *77*(1985). https://doi.org/10.1111/j.1467-8306.1987.tb00184.x

Cavazos, T., Turrent, C., & Lettenmaier, D. P. (2008). Extreme precipitation trends associated with tropical cyclones in the core of the North American monsoon. *Geophysical Research Letters*, *35*(21), L21703. https://doi.org/10.1029/2008GL035832

Cayan, D. R., Kammerdiener, S. A., Dettinger, M. D., Caprio, J. M., & Peterson, D. H. (2001). Changes in the Onset of Spring in the Western United States. *Bulletin of the American Meteorological Society*, *82*(3), 399–415. https://doi.org/10.1175/1520-0477(2001)082<0399:CITOOS>2.3.CO;2

Christensen, Niklas, S. ., Wood, Andrew, W. ., Nathalie, V., Lettenmaier, Dennis, P., & Palmer, Richard, N. (2004). The Effects of Climate Change on the Hydrology and Water Resources of the Colorado River Basin. *Climatic Change*, *62*(1–3), 337.

Christensen, N. S., & Lettenmaier, D. P. (2007). A multimodel ensemble approach to assessment of climate change impacts on the hydrology and water resources of the Colorado River Basin. *Hydrology and Earth System Sciences*, *11*(4), 1417–1434. https://doi.org/10.5194/hess-11-1417-2007

Christidis, N., & Stott, P. A. (2015). Changes in the geopotential height at 500 hPa under the influence of external climatic forcings. *Geophysical Research Letters*, *42*(24), 10,798-10,806. https://doi.org/10.1002/2015GL066669

Cohen, J. S., Zeff, H. B., & Herman, J. D. (2020). Adaptation of Multiobjective Reservoir

Operations to Snowpack Decline in the Western United States. *Journal of Water Resources Planning and Management*, *146*(12), 04020091. https://doi.org/10.1061/(asce)wr.1943-5452.0001300

Colorado River Basin Water Supply and Demand Study: Executive Summary. (2012). U.S. Department of the Interior Bureau of Reclamation.

Corbosiero, K. L., Dickinson, M. J., & Bosart, L. F. (2009). The Contribution of Eastern North Pacific Tropical Cyclones to the Rainfall Climatology of the Southwest United States. *Monthly Weather Review*, *137*(8), 2415–2435. https://doi.org/10.1175/2009MWR2768.1

Daly, C., Neilson, R. P., & Phillips, D. L. (1994). A Statistical-Topographic Model for Mapping Climatological Precipitation over Mountainous Terrain. *Journal of Applied Meteorology*, *33*(2), 140–158. https://doi.org/10.1175/1520-0450(1994)033<0140:ASTMFM>2.0.CO;2

Das, T., Pierce, D. W., Cayan, D. R., Vano, J. A., & Lettenmaier, D. P. (2011). The importance of warm season warming to western U.S. streamflow changes. *Geophysical Research Letters*, *38*(23), 1–5. https://doi.org/10.1029/2011GL049660

Delaney, C. J., Hartman, R. K., Mendoza, J., Dettinger, M., Delle Monache, L., Jasperse, J., … Evett, S. (2020). Forecast Informed Reservoir Operations Using Ensemble Streamflow Predictions for a Multipurpose Reservoir in Northern California. *Water Resources Research*, *56*(9). https://doi.org/10.1029/2019WR026604

Dettinger, M., & Cayan, D. (2014). Drought and the California Delta—A Matter of Extremes. *San Francisco Estuary and Watershed Science*, *12*(2). https://doi.org/10.15447/sfews.2014v12iss2art4

Dettinger, M. D., & Cayan, D. R. (2003). Interseasonal covariability of Sierra Nevada streamflow and San Francisco Bay salinity. *Journal of Hydrology*, *277*(3–4), 164–181. https://doi.org/10.1016/S0022-1694(03)00078-7

Dettinger, M. D., Ralph, F. M., Das, T., Neiman, P. J., & Cayan, D. R. (2011). Atmospheric Rivers, Floods and the Water Resources of California. *Water*, *3*(2), 445–478. https://doi.org/10.3390/w3020445

Dominguez, F., Kumar, P., & Vivoni, E. R. (2008). Precipitation Recycling Variability and Ecoclimatological Stability—A Study Using NARR Data. Part II: North American Monsoon Region. *Journal of Climate*, *21*(20), 5187–5203. https://doi.org/10.1175/2008JCLI1760.1

Douglas, M. W. (1995). The Summertime Low-Level Jet over the Gulf of California. *Monthly Weather Review*, *123*(8), 2334–2347. https://doi.org/10.1175/1520-0493(1995)123<2334:TSLLJO>2.0.CO;2

Douglas, M. W., Maddox, R. A., Howard, K., & Reyes, S. (1993). The Mexican Monsoon. *Journal of Climate*, *6*(8), 1665–1677. https://doi.org/10.1175/1520-0442(1993)006<1665:TMM>2.0.CO;2

Douglas, A. V., & Englehart, P. J. (2007). A Climatological Perspective of Transient Synoptic Features during NAME 2004. *Journal of Climate*, *20*(9), 1947–1954. https://doi.org/10.1175/JCLI4095.1

Draper, A. J., & Lund, J. R. (2004). Optimal Hedging and Carryover Storage Value. *Journal of*

Water Resources Planning and Management, *130*(1), 83–87. https://doi.org/10.1061/(asce)0733-9496(2004)130:1(83)

Favors, J. E., & Abatzoglou, J. T. (2013). Regional Surges of Monsoonal Moisture into the Southwestern United States. *Monthly Weather Review*, *141*(1), 182–191. https://doi.org/10.1175/MWR-D-12-00037.1

Finch, Z. O., & Johnson, R. H. (2010). Observational Analysis of an Upper-Level Inverted Trough during the 2004 North American Monsoon Experiment. *Monthly Weather Review*, *138*(9), 3540–3555. https://doi.org/10.1175/2010mwr3369.1

Fowler, H. J., Blenkinsop, S., & Tebaldi, C. (2007). Linking climate change modelling to impacts studies: recent advances in downscaling techniques for hydrological modelling. *International Journal of Climatology*, *27*(12), 1547–1578. https://doi.org/10.1002/joc.1556

Franz, K. J., Hartmann, H. C., Sorooshian, S., & Bales, R. (2003). Verification of National Weather Service Ensemble Streamflow Predictions for Water Supply Forecasting in the Colorado River Basin. *Journal of Hydrometeorology*, *4*(6), 1105–1118. https://doi.org/10.1175/1525-7541(2003)004<1105:vonwse>2.0.co;2

Fuller, R. D., & Stensrud, D. J. (2000). The Relationship between Tropical Easterly Waves and Surges over the Gulf of California during the North American Monsoon. *Monthly Weather Review*, *128*(8), 2983–2989. https://doi.org/10.1175/1520-0493(2000)128<2983:TRBTEW>2.0.CO;2

Garza, A. L. (1999). *1985-1998 north Pacific tropical cyclones impacting the southwestern United States and northern Mexico, an updated climatology* (N. W. S. United States Western Region, Ed.). Retrieved from https://repository.library.noaa.gov/view/noaa/14741

Gelaro, R., McCarty, W., Suárez, M. J., Todling, R., Molod, A., Takacs, L., … Zhao, B. (2017). The modern-era retrospective analysis for research and applications, version 2 (MERRA-2). *Journal of Climate*, *30*(14), 5419–5454. https://doi.org/10.1175/JCLI-D-16-0758.1

Georgakakos, A. P., Yao, H., Kistenmacher, M., Georgakakos, K. P., Graham, N. E., Cheng, F. Y., … Shamir, E. (2012). Value of adaptive water resources management in Northern California under climatic variability and change: Reservoir management. *Journal of Hydrology*, *412–413*, 34–46. https://doi.org/10.1016/j.jhydrol.2011.04.038

Gershunov, A., Shulgina, T., Clemesha, R. E. S., Guirguis, K., Pierce, D. W., Dettinger, M. D., … Ralph, F. M. (2019). Precipitation regime change in Western North America: The role of Atmospheric Rivers. *Scientific Reports*, *9*(1), 1–11. https://doi.org/10.1038/s41598-019-46169-w

Gonzalez, P. (U. S. N. P. S., Garfin, G. M. (University of A., Breshears, D. D., Brooks, K. M., Brown, H. E., Elias, E. H., … Udal, B. H. (2018). Fourth National Climate Assessment: Southwest. *Impacts, Risks, and Adaptation in the United States: Fourth National Climate Assessment*, *II*, 1101–1184. https://doi.org/10.7930/NCA4.2018.CH25

Gudmundsson, L., Bremnes, J. B., Haugen, J. E., & Engen-Skaugen, T. (2012). Technical Note: Downscaling RCM precipitation to the station scale using statistical transformations – a comparison of methods. *Hydrology and Earth System Sciences*, *16*(9), 3383–3390. https://doi.org/10.5194/hess-16-3383-2012

Hagemann, S., Chen, C., Haerter, J. O., Heinke, J., Gerten, D., & Piani, C. (2011). Impact of a statistical bias correction on the projected hydrological changes obtained from three GCMs and two hydrology models. *Journal of Hydrometeorology*, *12*(4), 556–578. https://doi.org/10.1175/2011JHM1336.1

Hales, J. E. (1974). Southwestern United States Summer Monsoon Source—Gulf of Mexico or Pacific Ocean? *Journal of Applied Meteorology*, *13*(3), 331–342. https://doi.org/10.1175/1520-0450(1974)013<0331:SUSSMS>2.0.CO;2

He, M., Anderson, M., Schwarz, A., Das, T., Lynn, E., Anderson, J., … Arnold, W. (2019). Potential changes in runoff of California's major water supply watersheds in the 21st century. *Water (Switzerland)*, *11*(8). https://doi.org/10.3390/w11081651

He, S., Guo, S., Yang, G., Chen, K., Liu, D., & Zhou, Y. (2020). Optimizing Operation Rules of Cascade Reservoirs for Adapting Climate Change. *Water Resources Management*, *34*(1), 101–120. https://doi.org/10.1007/s11269-019-02405-6

Herman, J. D., Zeff, H. B., Lamontagne, J. R., Reed, P. M., & Characklis, G. W. (2016). Synthetic Drought Scenario Generation to Support Bottom-Up Water Supply Vulnerability Assessments. *Journal of Water Resources Planning and Management*, *142*(11), 1–13. https://doi.org/10.1061/(asce)wr.1943-5452.0000701

Hewitson, B. C., Daron, J., Crane, R. G., Zermoglio, M. F., & Jack, C. (2014). Interrogating empirical-statistical downscaling. *Climatic Change*, *122*(4), 539–554. https://doi.org/10.1007/s10584-013-1021-z

Higgins, R. W., Shi, W., & Hain, C. (2004). Relationships between Gulf of California Moisture Surges and Precipitation in the Southwestern United States. *Journal of Climate*, *17*(15), 2983–2997. https://doi.org/10.1175/1520-0442(2004)017<2983:RBGOCM>2.0.CO;2

Higgins, W., & Gochis, D. (2007). Synthesis of Results from the North American Monsoon Experiment (NAME) Process Study. *Journal of Climate*, *20*(9), 1601–1607. https://doi.org/10.1175/JCLI4081.1

Hill, M. T., Platts, W. S., & Beschta, R. L. (1991). Ecological and geomorphological concepts for instream and out-of- channel flow requirements. *Rivers*, *2*(3), 198–210.

Holton, J. R. (2004). *An Introduction fo Dynamic Meteorology* (4th ed.). Elsevier Academic.

Hoskins, B. J., McIntyre, M. E., & Robertson, A. W. (1985). On the use and significance of isentropic potential vorticity maps. *Quarterly Journal of the Royal Meteorological Society*, *111*(470), 877–946. https://doi.org/10.1002/qj.49711147002

Huning, L. S., & AghaKouchak, A. (2018). Mountain snowpack response to different levels of warming. *Proceedings of the National Academy of Sciences of the United States of America*, *115*(43), 10932–10937. https://doi.org/10.1073/pnas.1805953115

Johnson, R. H., Ciesielski, P. E., McNoldy, B. D., Rogers, P. J., & Taft, R. K. (2007). Multiscales variability of the flow during the North American Monsoon experiment. *Journal of Climate*, *20*(9), 1628–1648. https://doi.org/10.1175/JCLI4087.1

Kalra, A., Piechota, T. C., Davies, R., & Tootle, G. A. (2008). Changes in U.S. Streamflow and Western U.S. Snowpack. *Journal of Hydrologic Engineering*, *13*(3), 156–163. https://doi.org/10.1061/(asce)1084-0699(2008)13:3(156)

Knapp, K. R., Kruk, M. C., Levinson, D. H., Diamond, H. J., & Neumann, C. J. (2010). The International Best Track Archive for Climate Stewardship (IBTrACS). *Bulletin of the American Meteorological Society*, *91*(3), 363–376. https://doi.org/10.1175/2009BAMS2755.1

Knowles, N., Cronkite-Ratcliff, C., Pierce, D. W., & Cayan, D. R. (2018). Responses of Unimpaired Flows, Storage, and Managed Flows to Scenarios of Climate Change in the San Francisco Bay-Delta Watershed. *Water Resources Research*, *54*(10), 7631–7650. https://doi.org/10.1029/2018WR022852

Knowles, Noah, & Cronkite-Ratcliff, C. (2018). *Modeling Managed Flows in the Sacramento/San Joaquin Watershed, California, Under Scenarios of Future Change for CASCaDE2*. 1–38. https://doi.org/https://doi.org/10.3133/ofr20181101

Knowles, Noah, Dettinger, M. D., & Cayan, D. R. (2006). Trends in snowfall versus rainfall in the western United States. *Journal of Climate*, *19*(18), 4545–4559. https://doi.org/10.1175/JCLI3850.1

Lahmers, T. M., Castro, C. L., Adams, D. K., Serra, Y. L., Brost, J. J., & Luong, T. (2016). Long-Term Changes in the Climatology of Transient Inverted Troughs over the North American Monsoon Region and Their Effects on Precipitation. *Journal of Climate*, *29*(17), 6037–6064. https://doi.org/10.1175/JCLI-D-15-0726.1

Lee, S. Y., Hamlet, A. F., Fitzgerald, C. J., Burges, S. J., & Lettenmaier, D. P. (2006). Optimized flood control in the Columbia River Basin for a global warming scenario. *Operating Reservoirs in Changing Conditions - Proceedings of the Operations Management 2006 Conference*, *2006*(6), 256–271. https://doi.org/10.1061/40875(212)26

Leung, L. R., Qian, Y., Bian, X., Washington, W. M., Han, J., & Roads, J. O. (2004). Mid-century ensemble regional climate change scenarios for the western United States. *Climatic Change*, *62*(1–3), 75–113. https://doi.org/10.1023/B:CLIM.0000013692.50640.55

Li, H., Sheffield, J., & Wood, E. F. (2010). Bias correction of monthly precipitation and temperature fields from Intergovernmental Panel on Climate Change AR4 models using equidistant quantile matching. *Journal of Geophysical Research Atmospheres*, *115*(10). https://doi.org/10.1029/2009JD012882

Liang, X., Lettenmaier, D. P., Wood, E. F., & Burges, S. J. (1994). A simple hydrologically based model of land surface water and energy fluxes for general circulation models. *Journal of Geophysical Research*. https://doi.org/10.1029/94jd00483

Liu, C., & Barnes, E. A. (2015). Extreme moisture transport into the Arctic linked to Rossby wave breaking. *Journal of Geophysical Research: Atmospheres*, *120*(9), 3774–3788. https://doi.org/10.1002/2014JD022796

Livneh, B., Rosenberg, E. A., Lin, C., Nijssen, B., Mishra, V., Andreadis, K. M., … Lettenmaier, D. P. (2013). A long-term hydrologically based dataset of land surface fluxes and states for the conterminous United States: Update and extensions. *Journal of Climate*, *26*(23), 9384–9392. https://doi.org/10.1175/JCLI-D-12-00508.1

Lorenz, E. N. (1963). Deterministic Nonperiodic Flow. *Journal of the Atmospheric Sciences*, *20*(2), 130–141. https://doi.org/10.1175/1520-0469(1963)020<0130:DNF>2.0.CO;2

Maddox, R. A., McCollum, D. M., & Howard, K. W. (1995). Large-Scale Patterns Associated with Severe Summertime Thunderstorms over Central Arizona. *Weather and Forecasting*, *10*(4), 763–778. https://doi.org/10.1175/1520-0434(1995)010<0763:LSPAWS>2.0.CO;2

Magnusson, L., & Källén, E. (2013). Factors influencing skill improvements in the ECMWF forecasting system. *Monthly Weather Review*, *141*(9), 3142–3153. https://doi.org/10.1175/MWR-D-12-00318.1

Mann, M. E., & Gleick, P. H. (2015). Climate change and California drought in the 21st century. *Proceedings of the National Academy of Sciences of the United States of America*, *112*(13), 3858–3859. https://doi.org/10.1073/pnas.1503667112

Maraun, D. (2013). Bias correction, quantile mapping, and downscaling: Revisiting the inflation issue. *Journal of Climate*, *26*(6), 2137–2143. https://doi.org/10.1175/JCLI-D-12-00821.1

Maraun, D., Shepherd, T. G., Widmann, M., Zappa, G., Walton, D., Gutiérrez, J. M., … Mearns, L. O. (2017). Towards process-informed bias correction of climate change simulations. *Nature Climate Change*, *7*(11), 764–773. https://doi.org/10.1038/nclimate3418

Martin, J. E. (2006). *Mid-Latitude Atmospheric Dynamics: A Frist Course* (Wiley, Ed.). Chichester, England.

Martius, O., & Rivière, G. (2016). Rossby wave breaking: climatology, interaction with low-frequency climate variability, and links to extreme weather events. *Dynamics and Predictability of Large-Scale, High-Impact Weather and Climate Events*, 69–78. https://doi.org/10.1017/cbo9781107775541.006

Maurer, E. P., & Pierce, D. W. (2014). Bias correction can modify climate model simulated precipitation changes without adverse effect on the ensemble mean. *Hydrology and Earth System Sciences*, *18*(3), 915–925. https://doi.org/10.5194/hess-18-915-2014

Mazon, J. J., Castro, C. L., Adams, D. K., Chang, H. I., Carrillo, C. M., & Brost, J. J. (2016). Objective climatological analysis of extreme weather events in Arizona during the North American monsoon. *Journal of Applied Meteorology and Climatology*, *55*(11), 2431–2450. https://doi.org/10.1175/JAMC-D-16-0075.1

McCabe, G. J., Clark, M. P., & Hay, L. E. (2007). Rain-on-snow events in the western United States. *Bulletin of the American Meteorological Society*, *88*(3), 319–328. https://doi.org/10.1175/BAMS-88-3-319

Michelangeli, P. A., Vrac, M., & Loukos, H. (2009). Probabilistic downscaling approaches: Application to wind cumulative distribution functions. *Geophysical Research Letters*, *36*(11), 2–7. https://doi.org/10.1029/2009GL038401

Middleton-Manning, B. R., Gali, M. S., & Houck, D. (2018). Holding the Headwaters: Northern California Indian Resistance to State and Corporate Water Development. *Decolonization-Indigeneity Education & Society*, *7*(1), 174–198.

Mioduszewski, J. R., Rennermalm, A. K., Robinson, D. A., & Wang, L. (2015). Controls on spatial and temporal variability in Northern Hemisphere terrestrial snow melt timing, 1979-2012. *Journal of Climate*, *28*(6), 2136–2153. https://doi.org/10.1175/JCLI-D-14-00558.1

Moody, P., & Brown, C. (2013). Robustness indicators for evaluation under climate change: Application to the upper Great Lakes. *Water Resources Research*, *49*(6), 3576–3588.

https://doi.org/10.1002/wrcr.20228

Mote, P. W., Hamlet, A. F., Clark, M. P., & Lettenmaier, D. P. (2005). DECLINING MOUNTAIN SNOWPACK IN WESTERN NORTH AMERICA*. *Bulletin of the American Meteorological Society*, *86*(1), 39–50. https://doi.org/10.1175/BAMS-86-1-39

Mote, P. W., Li, S., Lettenmaier, D. P., Xiao, M., & Engel, R. (2018). Dramatic declines in snowpack in the western US. *Npj Climate and Atmospheric Science*, *1*(1). https://doi.org/10.1038/s41612-018-0012-1

Musselman, K. N., Lehner, F., Ikeda, K., Clark, M. P., Prein, A. F., Liu, C., … Rasmussen, R. (2018). Projected increases and shifts in rain-on-snow flood risk over western North America. *Nature Climate Change*, *8*(9), 808–812. https://doi.org/10.1038/s41558-018-0236-4

Nayak, M. A., Herman, J. D., & Steinschneider, S. (2018). Balancing Flood Risk and Water Supply in California: Policy Search Integrating Short-Term Forecast Ensembles With Conjunctive Use. *Water Resources Research*, *54*(10), 7557–7576. https://doi.org/10.1029/2018WR023177

Ndarana, T., & Waugh, D. W. (2010). The link between cut-off lows and Rossby wave breaking in the Southern Hemisphere. *Quarterly Journal of the Royal Meteorological Society*, *136*(649), 869–885. https://doi.org/10.1002/qj.627

Nieto, R., Sprenger, M., Wernli, H., Trigo, R. M., & Gimeno, L. (2008). Identification and Climatology of Cut-off Lows near the Tropopause. *Annals of the New York Academy of Sciences*, *1146*(1), 256–290. https://doi.org/10.1196/annals.1446.016

Nieto, Raquel, Gimeno, L., de la Torre, L., Ribera, P., Gallego, D., García-Herrera, R., … Lorente, J. (2005). Climatological features of cutoff low systems in the Northern Hemisphere. *Journal of Climate*, *18*(16), 3085–3103. https://doi.org/10.1175/JCLI3386.1

Nijssen, B., O'donnell, G. M., Hamlet, A. F., & Lettenmaier, D. P. (2001). Hydrologic sensitivity of global rivers to climate change. *Climatic Change*, *50*(1–2), 143–175. https://doi.org/10.1023/A:1010616428763

Notaro, M., Liu, Z., Gallimore, R. G., Williams, J. W., Gutzler, D. S., & Collins, S. (2010). Complex seasonal cycle of ecohydrology in the Southwest United States. *Journal of Geophysical Research*, *115*(G4), G04034. https://doi.org/10.1029/2010JG001382

Oakley, N. S., & Redmond, K. T. (2014). A Climatology of 500-hPa closed lows in the northeastern pacific ocean, 1948-2011. *Journal of Applied Meteorology and Climatology*, *53*(6), 1578–1592. https://doi.org/10.1175/JAMC-D-13-0223.1

Panofsky, H. A., & Brier, G. W. (1968). Some Applications of Statistics to Meteorology. In *College of Mineral Industries, The Pennsylvania State University*.

Pascale, S., & Bordoni, S. (2016). Tropical and Extratropical Controls of Gulf of California Surges and Summertime Precipitation over the Southwestern United States. *Monthly Weather Review*, *144*(7), 2695–2718. https://doi.org/10.1175/MWR-D-15-0429.1

Pascale, S., Bordoni, S., Kapnick, S. B., Vecchi, G. A., Jia, L., Delworth, T. L., … Anderson, W. (2016). The Impact of Horizontal Resolution on North American Monsoon Gulf of California Moisture Surges in a Suite of Coupled Global Climate Models. *Journal of*

Climate, *29*(21), 7911–7936. https://doi.org/10.1175/JCLI-D-16-0199.1

Patterson, N. K., Lane, B. A., Sandoval-Solis, S., Pasternack, G. B., Yarnell, S. M., & Qiu, Y. (2020). A hydrologic feature detection algorithm to quantify seasonal components of flow regimes. *Journal of Hydrology*, *585*(August 2019), 124787. https://doi.org/10.1016/j.jhydrol.2020.124787

Payne, J. T., Wood, A. W., Hamlet, A. F., Palmer, R. N., & Lettenmaier, D. P. (2004). Mitigating the effects of climate change on the water resources of the Columbia River Basin. *Climatic Change*, *62*(1–3), 233–256. https://doi.org/10.1023/B:CLIM.0000013694.18154.d6

Pederson, G. T., Gray, S. T., Ault, T., Marsh, W., Fagre, D. B., Bunn, A. G., … Graumlich, L. J. (2011). Climatic controls on the snowmelt hydrology of the northern Rocky Mountains. *Journal of Climate*, *24*(6), 1666–1687. https://doi.org/10.1175/2010JCLI3729.1

Petts, G. E. (1996). Water Allocation to Protect River Ecosystems. *Regulated Rivers: Research & Management*, *12*(4–5), 353–365. https://doi.org/10.1002/(SICI)1099-1646(199607)12:4/5<353::AID-RRR425>3.0.CO;2-6

Pierce, D. W., Barnett, T. P., Hidalgo, H. G., Das, T., Bonfils, C., Santer, B. D., … Nozawa, T. (2008). Attribution of declining Western U.S. Snowpack to human effects. *Journal of Climate*, *21*(23), 6425–6444. https://doi.org/10.1175/2008JCLI2405.1

Pierce, D. W., & Cayan, D. R. (2013). The uneven response of different snow measures to human-induced climate warming. *Journal of Climate*, *26*(12), 4148–4167. https://doi.org/10.1175/JCLI-D-12-00534.1

Pierce, D. W., Cayan, D. R., Maurer, E. P., Abatzoglou, J. T., & Hegewisch, K. C. (2015). Improved bias correction techniques for hydrological simulations of climate change. *Journal of Hydrometeorology*, *16*(6), 2421–2442. https://doi.org/10.1175/JHM-D-14-0236.1

Pierce, D. W., Cayan, D. R., & Thrasher, B. L. (2014). Statistical downscaling using localized constructed analogs (LOCA). *Journal of Hydrometeorology*, *15*(6), 2558–2585. https://doi.org/10.1175/JHM-D-14-0082.1

Pierce, D. W., Das, T., Cayan, D. R., Maurer, E. P., Miller, N. L., Bao, Y., … Tyree, M. (2013). Probabilistic estimates of future changes in California temperature and precipitation using statistical and dynamical downscaling. *Climate Dynamics*, *40*(3–4), 839–856. https://doi.org/10.1007/s00382-012-1337-9

Poff, N. L. R., Allan, J. D., Bain, M. B., Karr, J. R., Prestegaard, K. L., Richter, B. D., … Stromberg, J. C. (1997). The natural flow regime: A paradigm for river conservation and restoration. *BioScience*, *47*(11), 769–784. https://doi.org/10.2307/1313099

Polade, S. D., Pierce, D. W., Cayan, D. R., Gershunov, A., & Dettinger, M. D. (2014). The key role of dry days in changing regional climate and precipitation regimes. *Scientific Reports*, *4*, 1–8. https://doi.org/10.1038/srep04364

Postel, G. A., & Hitchman, M. H. (1999). A Climatology of Rossby Wave Breaking along the Subtropical Tropopause. *Journal of the Atmospheric Sciences*, *56*(3), 359–373. https://doi.org/10.1175/1520-0469(1999)056<0359:ACORWB>2.0.CO;2

Pytlak, E., & Goering, M. (2005). Upper tropospheric troughs and their interaction with the North American Monsoon. *19th Conference on Hydrology*. Retrieved from http://ams.confex.com/ams/Annual2005/techprogram/paper_85393.htm

Rajagopalan, B., Nowak, K., Prairie, J., Hoerling, M., Harding, B., Barsugli, J., … Udall, B. (2009). Water supply risk on the Colorado River: Can management mitigate? *Water Resources Research*, *45*(8), 1–7. https://doi.org/10.1029/2008WR007652

Ray, A. J., Garfin, G. M., Wilder, M., Vásquez-León, M., Lenart, M., & Comrie, A. C. (2007). Applications of Monsoon Research: Opportunities to Inform Decision Making and Reduce Regional Vulnerability. *Journal of Climate*, *20*(9), 1608–1627. https://doi.org/10.1175/JCLI4098.1

Richter, B. D., Baumgartner, J. V., Powell, J., & Braun, D. P. (1996). A Method for Assessing Hydrologic Alteration within Ecosystems. *Conservation Biology*, *10*(4), 1163–1174. https://doi.org/10.1046/j.1523-1739.1996.10041163.x

Rosen, M. R., Turner, K., Goodbred, S. L., & Miller, J. M. (2012). A Synthesis of Aquatic Science for Management of Lakes Mead and Mohave. In *U.S. Geological Survey Circular 1381*.

Saarinen, T.F., Baker, V.R., Durrenburger, R., Maddock, T. (1984). The Tucson, Arizona, Flood of October 1983. *National Academy Press*, 112.

Salathé, E. P. (2003). Comparison of various precipitation downscaling methods for the simulation of streamflow in a rainshadow river basin. *International Journal of Climatology*, *23*(8), 887–901. https://doi.org/10.1002/joc.922

Schmitz, J. T., & Mullen, S. L. (1996). Water vapor transport associated with the summertime North American monsoon as depicted by ECMWF analyses. *Journal of Climate*, Vol. 9, pp. 1621–1634. https://doi.org/10.1175/1520-0442(1996)009<1621:WVTAWT>2.0.CO;2

Scott, R. K., Cammas, J.-P., Mascart, P., & Stolle, C. (2001). Stratospheric filamentation into the upper tropical troposphere. *Journal of Geophysical Research: Atmospheres*, *106*(D11), 11835–11848. https://doi.org/10.1029/2001JD900049

Seastrand, S., Serra, Y., Castro, C., & Ritchie, E. (2015). The dominant synoptic-scale modes of North American monsoon precipitation. *International Journal of Climatology*. https://doi.org/10.1002/joc.4104

Serreze, M. C., Clark, M. P., Armstrong, R. L., McGinnis, D. A., & Pulwarty, R. S. (1999). Characteristics of the western United States snowpack from snowpack telemetry (SNOTEL) data. *Water Resources Research*, *35*(7), 2145–2160. https://doi.org/10.1029/1999WR900090

Shafer, B.A., Huddleston, J. M. (1984). Analysis of Seasonal Volume Streamflow Forecast Errors in the Western United States. *Proc. A Critical Assessment of Forecasting in Water Quality Goals in Western Water Resources Management,* 117–126. Bethesda, MD: American Water Resources Association.

Small, E. E. (2001). The influence of soil moisture anomalies on variability of the North American Monsoon System. *Geophysical Research Letters*, *28*(1), 139–142. https://doi.org/10.1029/2000GL011652

Smith, B. A., Bosart, L. F., Keyser, D., & Jean, D. S. (2002). A GLOBAL 500 HPA CUTOFF CYCLONE CLIMATOLOGY : 1953 - 1999. *Proc. 19th Conf. on Weather Analysis and Forecasting*, (August).

Steinschneider, S., & Brown, C. (2012). Dynamic reservoir management with real-option risk hedging as a robust adaptation to nonstationary climate. *Water Resources Research*, *48*(5), 1–16. https://doi.org/10.1029/2011WR011540

Stensrud, D. J., Gall, R. L., & Nordquist, M. K. (1997). Surges over the Gulf of California during the Mexican Monsoon. *Monthly Weather Review*, *125*(4), 417–437. https://doi.org/10.1175/1520-0493(1997)125<0417:SOTGOC>2.0.CO;2

Sterle, K., Jose, L., Coors, S., Singletary, L., Pohll, G., & Rajagopal, S. (2020). Collaboratively Modeling Reservoir Reoperation to Adapt to Earlier Snowmelt Runoff. *Journal of Water Resources Planning and Management*, *146*(1), 1–14. https://doi.org/10.1061/(asce)wr.1943-5452.0001136

Stewart, I. T., Cayan, D. R., & Dettinger, M. D. (2005). Changes toward earlier streamflow timing across western North America. *Journal of Climate*, *18*(8), 1136–1155. https://doi.org/10.1175/JCLI3321.1

Stramler, K., Del Genio, A. D., & Rossow, W. B. (2011). Synoptically Driven Arctic Winter States. *Journal of Climate*, *24*(6), 1747–1762. https://doi.org/10.1175/2010JCLI3817.1

Swain, D. L., Langenbrunner, B., Neelin, J. D., & Hall, A. (2018). Increasing precipitation volatility in twenty-first-century California. *Nature Climate Change*, *8*(5), 427–433. https://doi.org/10.1038/s41558-018-0140-y

Tanaka, S. K., Zhu, T., Lund, J. R., Howitt, R. E., Jenkins, M. W., Pulido, M. A., … Ferreira, I. C. (2006). Climate warming and water management adaptation for California. *Climatic Change*, *76*(3–4), 361–387. https://doi.org/10.1007/s10584-006-9079-5

Tang, M., & Reiter, E. R. (2002). Plateau Monsoons of the Northern Hemisphere: A Comparison between North America and Tibet. *Monthly Weather Review*, Vol. 112, pp. 617–637. https://doi.org/10.1175/1520-0493(1984)112<0617:pmotnh>2.0.co;2

Taylor, K. E., Stouffer, R. J., & Meehl, G. A. (2012). An overview of CMIP5 and the experiment design. *Bulletin of the American Meteorological Society*, *93*(4), 485–498. https://doi.org/10.1175/BAMS-D-11-00094.1

Teutschbein, C., & Seibert, J. (2012). Bias correction of regional climate model simulations for hydrological climate-change impact studies: Review and evaluation of different methods. *Journal of Hydrology*, *456–457*, 12–29. https://doi.org/10.1016/j.jhydrol.2012.05.052

Thorncroft, C. D., Hoskins, B. J., & McIntyre, M. E. (1993). Two paradigms of baroclinic-wave life-cycle behaviour. *Quarterly Journal of the Royal Meteorological Society*, *119*(509), 17–55. https://doi.org/10.1002/qj.49711950903

Thrasher, B., Maurer, E. P., McKellar, C., & Duffy, P. B. (2012). Technical Note: Bias correcting climate model simulated daily temperature extremes with quantile mapping. *Hydrology and Earth System Sciences*, *16*(9), 3309–3314. https://doi.org/10.5194/hess-16-3309-2012

U.S. Bureau of Reclamation. (2019a). *Chapter 4 Proposed Action*.

U.S. Bureau of Reclamation. (2019b). *Facility Descriptions and Operations: Reinitiation of Consultation on the Coordinated Long-Term Operation of the Central Valley Project and State Water Project*.

Udall, B., & Overpeck, J. (2017). The twenty-first century Colorado River hot drought and implications for the future. *Water Resources Research*, *53*(3), 2404–2418. https://doi.org/10.1002/2016WR019638

United States Bureau of Reclamation. (2015). *Shasta Lake Water Resources Investigation: Feasibility Report*.

US. Army Corps of Engineers. (1977). *SHASTA DAM AND LAKE REPORT ON RESERVOIR REGULATION FOR FLOOD CONTROL - Appendix I*.

US Department of Interior, B. of R. (2011). *Hydrology , Hydraulics , and Water Management Technical Report*.

Vivoni, E. R. (2012). Diagnosing Seasonal Vegetation Impacts on Evapotranspiration and Its Partitioning at the Catchment Scale during SMEX04–NAME. *Journal of Hydrometeorology*, *13*(5), 1631–1638. https://doi.org/10.1175/JHM-D-11-0131.1

Watson, A. I., López, R. E., & Holle, R. L. (1994). Diurnal Cloud-to-Ground Lightning Patterns in Arizona during the Southwest Monsoon. *Monthly Weather Review*, *122*(8), 1716–1725. https://doi.org/10.1175/1520-0493(1994)122<1716:DCTGLP>2.0.CO;2

Watts, C. J., Scott, R. L., Garatuza-Payan, J., Rodriguez, J. C., Prueger, J. H., Kustas, W. P., & Douglas, M. (2007). Changes in Vegetation Condition and Surface Fluxes during NAME 2004. *Journal of Climate*, *20*(9), 1810–1820. https://doi.org/10.1175/JCLI4088.1

Weaver, C. P., Lempert, R. J., Brown, C., Hall, J. A., Revell, D., & Sarewitz, D. (2013). Improving the contribution of climate model information to decision making: The value and demands of robust decision frameworks. *Wiley Interdisciplinary Reviews: Climate Change*, *4*(1), 39–60. https://doi.org/10.1002/wcc.202

Wilby, R. L., & Keenan, R. (2012). Adapting to flood risk under climate change. *Progress in Physical Geography*, *36*(3), 348–378. https://doi.org/10.1177/0309133312438908

Willis, A. D., Lund, J. R., Townsley, E. S., & Faber, B. A. (2011). Climate Change and Flood Operations in the Sacramento Basin, California. *San Francisco Estuary and Watershed Science*, *9*(2). https://doi.org/10.15447/sfews.2011v9iss2art3

Wood, A. W., Maurer, E. P., Kumar, A., & Lettenmaier, D. P. (2002). Long-range experimental hydrologic forecasting for the eastern United States. *Journal of Geophysical Research: Atmospheres*, *107*(20), ACL 6-1-ACL 6-15. https://doi.org/10.1029/2001JD000659

Wood, K. M., & Ritchie, E. A. (2014). A 40-year climatology of extratropical transition in the Eastern North Pacific. *Journal of Climate*, *27*(15), 5999–6015. https://doi.org/10.1175/JCLI-D-13-00645.1

Yarnell, S. M., Petts, G. E., Schmidt, J. C., Whipple, A. A., Beller, E. E., Dahm, C. N., … Viers, J. H. (2015). Functional Flows in Modified Riverscapes: Hydrographs, Habitats and Opportunities. *BioScience*, *65*(10), 963–972. https://doi.org/10.1093/biosci/biv102